



Norwegian University of
Science and Technology

Pitting Corrosion of Super Duplex Stainless Steel - Effect of Tungsten and Isothermal Heat Treatments

Hege Kokslien Østvold

Chemical Engineering and Biotechnology

Submission date: June 2017

Supervisor: Ida Westermann, IMA

Co-supervisor: Roy Johnsen, MTP

Norwegian University of Science and Technology
Department of Materials Science and Engineering

Preface

This master thesis has been conducted at the Norwegian University of Science and Technology, at the Department of Materials Science and Engineering during the spring of 2017.

Associate Professor Ida Westermann and Professor Roy Johnsen at NTNU has supervised the thesis work. The work has been done in collaboration with Adjunct Professor Mariano Iannuzzi from GE Oil & Gas. The experimental work was performed at the metallographic laboratory at Department of Mechanical and Industrial Engineering and the SINTEF and NTNU Corrosion Laboratory. The studied materials were provided by Sandvik and Nippon Steel & Sumitomo Metal Corporation.

I hereby declare that this work has been carried out independently.

Hege Kokslien Østvold, Trondheim June 12, 2017

Acknowledgments

I would like to thank my supervisors, Associate Professor Ida Westermann and Professor Roy Johnsen for giving me feedback during the thesis work. An extra special thanks to Roy Johnsen for always being available.

The knowledge and contributions of Adjunct Professor Mariano Iannuzzi are highly appreciated, and I wish to thank him for all the feedback and interest in the results.

Huge thanks go to PhD-candidate at the Department of Mechanical and Industrial Engineering, Cristian Torres, for all the help during the experimental work, for the help with the SEM micrographs and for all the good conversations.

I wish to thank my fellow master student Mia Bernås for all her work on microstructure characterizations prior to electrochemical measurements and for discussions during the work, and Christian Lauritsen for his work with corrosion testing of low-W SDSS.



Abstract

Duplex stainless steels (DSS) and super duplex stainless steels (SDSS) can be described as austenitic-ferritic stainless steels with a chromium content of 22 and 25 %, respectively. Because of their good combination of superior corrosion resistance in chloride containing environments and high strength, together with a competitive cost, they are widely used in many industries. During production and fabrication of DSS and SDSS, they are exposed to heat treatments and welding. Since they also have a high content of alloying elements, they are prone to precipitation of deleterious intermetallic phases. When exposed to temperatures in the range of 800°C to 900°C, which is the most interesting in this work, precipitation of σ - and χ -phase, concurrently with γ_2 , are the most detrimental intermetallic phases. Due to these intermetallic phases, the duplex steels are prone to localized corrosion. This is because chromium and molybdenum are depleted from mainly ferrite, but also from the austenite phase.

To delay the precipitation of σ -phase, it has been proposed to partially replace molybdenum with tungsten (W), which promotes the precipitation of χ -phase. There are opposing opinions about the effect of tungsten addition in promoting χ phase precipitation. Some claim the χ -phase to be more detrimental than the σ -phase, while others look at the χ -phase as less deleterious, yet others have suggested that tungsten accelerated the precipitation of all deleterious phases, including χ - and σ -phase. To examine how tungsten substitution affects the corrosion resistance of SDSS during isothermal heat treatments, two SDSS grades with 0 wt% and 2.1 wt% W was investigated. The results of this work were compared with previously obtained results by another student on a SDSS grade with 0.62 wt% W. Before electrochemical measurements, the test samples were solution annealed at 1110°C and isothermally heat treated at 790°C, 846°C and 920°C at different holding times. The electrochemical measurements consisted of an open circuit potential (OCP) measurement while exposed in 6 wt% ferric chloride solution with increasing temperature, to find the critical pitting temperature (CPT), and recording of anodic cyclic potentiodynamic polarization (CPP) curves. Prior to electrochemical measurements, another student performed metallographic examinations on the three mentioned SDSS grades. The influence of the microstructure was quantified by comparing the outcome of the electrochemical results with the detailed

metallographic examination.

CPT was found to decrease with increasing isothermal heating time and, thus, increasing precipitation rate and amount of intermetallic phases. For almost all the holding times, CPT was found to increase in the order of SDSS containing 0.62 wt% W < 0 wt% W < 2.1 wt% W. A critical holding time was found to be between 2 and 4 minutes for SDSS containing 0 wt% W and between 4 and 10 minutes for SDSS containing 2.1 wt% W. The anodic CPP curves confirmed the results from the CPT measurements. The results indicated that relatively high tungsten additions promoted a better pitting corrosion resistance, whereas the opposite was observed at smaller additions. Surface characterizations after electrochemical measurements showed pitting corrosion to mainly initiate at the depleted areas around the intermetallic phases.

Sammendrag

Duplex rustfrie stål (DSS) og super duplex rustfrie stål (SDSS) kan beskrives som austenitt-ferrittiske rustfrie stål med et krominnhold på henholdsvis 22 og 25 %. Disse ståltypene er benyttet i mange industrier på grunn av deres gode kombinasjon av overlegen korrosjonsmotstand i klorholdige miljøer og høye styrke, i tillegg til en konkurransedyktig pris. Under produksjonen og fabrikkeringen av DSS og SDSS blir de utsatt for varmebehandlinger og sveising, og på grunn av deres høye legeringsinnhold er de utsatt for skadelige intermetalliske faser. Når de blir utsatt for temperaturer mellom 800°C og 900°C, som er de mest interessante i dette arbeidet, er de mest skadelige intermetalliske fasene felles ut σ - og χ -fasen, samt γ_2 . På grunn av disse intermetalliske fasene er duplex stål utsatt for lokalisert korrosjon. Dette er fordi krom og molybdenum tømmes fra hovedsakelig ferritt, men også fra austenitt.

For å utsette utfellingen av σ -fasen har det blitt foreslått å erstatte noe av mengden molybden med wolfram (W) som fremmer utfellingen av χ -fasen. Det er motstridene meninger om effekten av å tilsette wolfram til å fremme effekten av χ -fasen. Noen mener at χ -fasen er mer skadelig enn σ -fasen, mens andre mener at χ -fasen er mindre skadelig. Andre igjen har antydnet at wolfram akselererer utfellingen av alle skadelige faser, inkludert χ - og σ -fasen. For å undersøke hvordan wolframtilsetning påvirker korrosjonsmotstanden til SDSS under isoterme varmebehandlinger var to SDSS stålvaliteter med henholdsvis 0 vekt% and 2.1 vekt% W undersøkt. Resultatene fra dette arbeidet var sammenlignet med tidligere oppnådde resultater av en annen masterstudent på en SDSS stålvalitet med 0.62 vekt% W. Testprøvene ble løsningsherdet ved 1110°C and isotermt varmebehandlet ved 790°C, 846°C and 920°C ved forskjellige holdetider. De elektrokjemiske målingene bestod av en åpent kretspotensial (OCP) måling mens prøven var utsatt for en 6 vekt% jernkloridløsning med økende temperatur, for å finne den kritiske gropkorrosjonstemperaturen (CPT), og opptak av anodisk syklisk potensiodynamisk polarisasjon (CPP) kurver. En annen student utførte metallografiske undersøkelser på de tre nevnte SDSS stålvalitetene før de elektrokjemiske målingene. Mikrostrukturens påvirkning ble kvantifisert ved å sammenligne utfallet av de elektrokjemiske resultatene med den detaljerte metallografiske undersøkelsen.

Resultatene viser at CPT minker med økende isoterm varmebehandlingstid, og dermed en økende utfellingshastighet og mengde intermetalliske faser. For nesten alle holdetidene ble det funnet at CPT økte i rekkefølgen av SDSS innhold på 0.62 vekt% W, 0 vekt% W, 2.1 vekt% W. Det ble funnet en kritisk varmebehandlingstid på mellom 2 og 4 minutter for SDSS som inneholder 0 vekt% W og på mellom 4 og 10 minutter for SDSS for inneholder 2.1 vekt% W. De anodiske CPP kurvene bekreftet resultatet fra CPT målingene, noe som indikerer at relativt høye tilsetninger av wolfram fremmer en bedre groppkorrosjonsmotstand, mens det motsatte er observert for mindre tilsetninger. Overflatekarakteriseringer etter de elektrokjemiske målingene viste at groppkorrosjon hovedsakelig initierte i de intermetalliske fasene.

Contents

Preface	I
Acknowledgments	III
Abstract	V
Sammendrag	VII
1 Introduction	3
2 Theory	5
2.1 Super duplex stainless steels	5
2.1.1 Microstructure	5
2.1.2 Effect of alloying elements in SDSS	7
2.2 Effect of heat treatment of SDSS	13
2.2.1 Intermetallic precipitates and secondary phases	15
2.3 Corrosion of SDSS	19
2.3.1 Localized corrosion	20
2.3.2 Galvanic corrosion	21
2.4 Pitting corrosion	22
2.4.1 Mechanism	22
2.4.2 Kinetics and parameters	27
3 Experimental work	33
3.1 Test material	34
3.2 Heat treatment	35
3.2.1 Solution annealing	37
3.2.2 Isothermal heat treatment	37
3.3 Electrochemical measurements	42
3.3.1 Critical pitting temperature measurements	42
3.3.2 Anodic cyclic potentiodynamic polarization curves	46

3.4	Surface characterization	50
4	Results	51
4.1	CPT measurements	51
4.1.1	Surface characterization after electrochemical measurements .	60
4.2	Anodic cyclic potentiodynamic polarization curves	67
4.2.1	Surface characterization after electrochemical measurements .	76
5	Discussion	81
5.1	Electrochemical measurements	81
5.2	General trends	82
5.3	Effect of tungsten and isothermal heat treatments	84
5.3.1	Solution annealed condition	84
5.3.2	As-delivered condition	85
5.3.3	T1 - isothermal heat treatment	86
5.3.4	T2 - isothermal heat treatment	90
5.3.5	T3 isothermal heat treatment	92
5.4	Surface characterization after electrochemical measurements	94
5.4.1	After CPT measurements	94
5.4.2	After recording of anodic CPP curves	95
5.4.3	Pit initiating	96
5.5	Limitations and sources of error	98
6	Conclusion	101
7	Further work	103
	APPENDICES	i
A	Material data sheet	i
B	CPT	vii
B.1	Weight and area measurements	vii
B.2	Electrochemical measurements	ix
B.3	Previous work	xi
B.3.1	Microstructure characterization	xi
B.3.2	CPT	xviii
B.4	Surface characterization	xx
C	Anodic CPP	xxv
C.1	Electrochemical measurements	xxv
C.2	Surface characterization	xxxv

C.3 OCP xxxviii

Abbreviations and symbols

	Unit	Explanation
A	cm ²	Area
BSE	-	Backscattered electron
CCT	°C	Critical crevice temperature
CPP	-	Cyclic potentiodynamic polarization
CPT	°C	Critical pitting temperature
d	cm	Diameter
DSS	-	Duplex stainless steel
E_{corr}	V	Corrosion potential
E_{flade}	V	Flade potential
E_p	V	Pitting potential
E_{RP}	V	Repassivation potential
E_{trans}	V	Transpassive potential
??? EBSD	-	Electron backscattered diffraction
EDS	-	Energi dispersive spectroscopy
h	cm	Hight
HAZ	-	Heat affected sone
i	$\frac{A}{cm^2}$	Current density
i_p	$\frac{A}{cm^2}$	Anodic passive current density
IPM	-	Department of engineering design and materials
IHt	min	Isothermal heating time
IHT	°C	Isothermal heating temperature
LOM	-	Light optical microscope
OCP	V	Open circuit potential
OM	-	Optical microscope
PRE_N	-	Pitting resistance equivalent number
$PRE_{N,W}$	-	Pitting resistance equivalent number included tungsten
SCC	-	Stress corrosion cracking
SCE	-	Standard calomel electrode
SDSS	-	Super duplex stainless steel
SEM	-	Scanning electron microscope
SHE	-	Standard hydrogen electrode
t	min	Time
T	°C	Temperature
TTT	-	Temperature-Time-Transformation
α	-	Ferrite
γ	-	Austenite
γ_2	-	Secondary austenite
σ	-	Sigma phase
χ	-	Chi phase

Chapter 1

Introduction

Duplex stainless steels (DSS) and super duplex stainless steels (SDSS) have a chromium content of about 22 and 25 wt%, respectively. They are widely used in industry because of their excellent combination of high corrosion resistance in corrosive environments and high strength. The high corrosion resistance is mainly due to alloying with chromium, molybdenum, nitrogen, and tungsten, and because of the duplex microstructure that consists of almost equal amounts of ferrite (α) and austenite (γ). It is the relatively fine grains in duplex steels that give the high strength. Compared to austenitic stainless steels, DSS and SDSS have several advantages like superior corrosion resistance, higher mechanical strength and a lower price due to lower nickel content[1, 2, 3, 4].

During heat treatments and welding, DSS and SDSS are prone to the formation of secondary and intermetallic phases in the temperature range 400-1000°C[5]. In this work, sigma (σ), chi (χ), secondary austenite (γ_2), and chromium nitrides (Cr_2N) are the most important ones. They can precipitate during welding or due to improper heat treatment. This will affect the corrosion resistance and mechanical properties for the duplex steel, and to assure their safe use, it is important to understand how these phases affect the steel quality[5]. To delay precipitation of intermetallic phases towards longer holding times in DSS, it has been suggested by Ogawa et al. [6] and Kim and Kwon [7] to partially or completely substitute molybdenum (Mo) with tungsten (W). However, other studies have found additions of tungsten in DSS to accelerate the precipitation rate of intermetallic phases and to stabilize them towards higher temperatures[8, 9].

The main objective of this work was to quantify the effect of tungsten on phase transformation kinetics and the effect of microstructure on localized corrosion resistance. Where the focus is on the effect that σ -phase, χ -phase, and γ_2 have on the corrosion properties of SDSS. The results from these measurements are going to be com-

pared to previous measurements done by other students. One student have focused on corrosion testing of a SDSS grade with a tungsten content of 0.62 wt% and the other student focused on microstructure characterization prior to electrochemical measurements, where the effect of tungsten on the precipitation kinetics of intermetallic σ - and χ -phase after isothermal heat treatment was the main objective. Microstructure characterizations was performed using light optical microscopy (LOM), scanning electron microscope (SEM), backscattered electrons (BSE) in the SEM, and electron backscatter diffraction (EBSD).

To get a better understanding of how tungsten additions affect the corrosion resistance of SDSS after heat treatments and welding, W-free and W-rich SDSS samples were isothermally heat treated at three different temperatures in the range of 800°C to 900°C at different holding times. Through critical pitting temperature (CPT) measurements and recording of anodic cyclic potentiodynamic polarization (CPP) curves, the effect of tungsten and isothermal heat treatments on the pitting corrosion resistance of SDSS could be better understood. The results of the different works are combined to get a deeper understanding on how the precipitation of secondary and intermetallic phases affects the corrosion properties of SDSS.

Chapter 2

Theory

2.1 Super duplex stainless steels

Stainless steels are divided into four main groups based on their microstructure: ferritic, austenitic, martensitic and ferritic/austenitic. There are also precipitation hardening stainless steels that can be either martensitic or austenitic[10]. Duplex stainless steels (DSS) are defined as ferritic/austenitic stainless steels that contain minimum 22 wt% chromium, which is the same amount as for austenitic stainless steels. They also have similar corrosion resistance. Super duplex stainless steels (SDSS) are high alloyed versions of DSS, with a chromium content of minimum 25 wt% and a pitting resistance equivalent number (PRE_N) above 40[1]. PRE_N is an estimate of the effect of chromium, molybdenum, and nitrogen. It developed to reflect and predict the pitting resistance of a stainless steel, based upon the proportions of mentioned alloys[11]. PRE_N will be further described in Section 2.4.2. The chemical composition and microstructure found in duplex steels result in particularly high strength, very good resistance to stress corrosion cracking and localized corrosion, good abrasion, and wear. Thus, it is not surprising that different grades of DSS are commonly used in a large field of applications in marine and petrochemical industries[2, 3]. SDSS also has a reduced content of high-cost nickel compared to austenitic stainless steels, without sacrificing the high strength and corrosion resistance. They are therefore a more economical and advantageous choice[4].

2.1.1 Microstructure

DSS and SDSS obtain their optimum combination of corrosion resistance and mechanical properties by having approximately the same amount of ferrite (α) and austenite

(γ), and due their alloying elements and their relatively small grain sizes. α and γ are present in relatively large separate volumes and in approximately equal volume fractions. The α content can vary between 35 and 55 wt%, but manufacturers balance the steels close to an ideal 50/50 wt%. The main alloying elements in duplex steels are chromium (Cr), molybdenum (Mo), nickel (Ni), and nitrogen (N). They are not evenly distributed in the two phases. Chromium and molybdenum are concentrated in ferrite, whereas nickel and nitrogen are enriched in austenite. Thus, chromium and molybdenum are austenite stabilizers and expand the γ -field and encourages the formation of austenite over wider compositional limits, whereas nickel and nitrogen are ferrite stabilizer and contract the α -field and thereby encourages the formation of ferrite[12]. The partitioning of these elements affects the corrosion resistance of both the single phases and the entire alloy[3, 13, 14, 15]. The α/γ microstructure of a UNS S32750 SDSS are shown in Figure 2.1.1, where the dark phase is α and the brighter phase is γ .

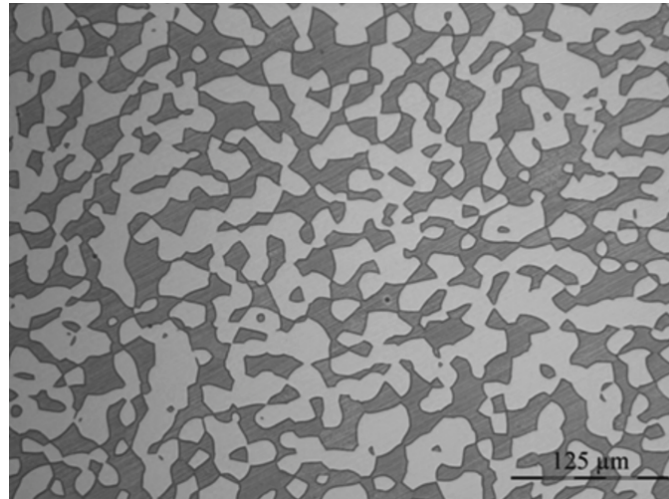


Figure 2.1.1: Optical image of the typical microstructure of SDSS, here UNS S32750, showing the dark α -phase and the brighter γ -phase[13].

The α/γ microstructure is designed to help overcome the low toughness of ferritic stainless steels and the stress corrosion cracking (SCC) susceptibility of austenitic stainless steels[4]. The high pitting corrosion resistance is due to the high amounts of chromium, molybdenum, nitrogen, and tungsten in W-containing SDSS. For optimum corrosion resistance these alloying elements should be dissolved in the ferrite and austenite phases and not precipitate as secondary and intermetallic phases[1, 5, 16, 17]. However, with increased levels of alloying also comes an increased sensitivity for formation of intermetallic phases, which can precipitate during heat treatments like fabrication and hot forming processes or quenching[17]. The corrosion properties of both ferrite and austenite are in SDSS strongly dependent on their chemical compo-

sition. The secondary and intermetallic phases are caused by the alloying elements, and their formation reduces the corrosion resistance and makes the alloy more susceptible to localized corrosion attacks. These types of precipitations can also affect the mechanical properties, such as toughness. Sigma (σ) phase, chi (χ) phase, secondary austenite (γ_2), and chromium nitride (Cr_2N), are some examples of secondary and intermetallic phases. The most important factors in the precipitation behavior of SDSS are chemical composition and heat treatment temperature. They both determine the phase volume fraction of ferrite and austenite, and the partitioning of the main alloying elements[4, 15, 17, 18, 19]. The σ -phase is a brittle intermetallic compound that is rich in chromium and molybdenum, and it has a larger volume fraction than any other intermetallic phase in the alloys. Precipitation of σ also depletes surrounding phases of chromium and molybdenum, while nickel simultaneously diffuses into α . Thus, enriching α with γ -stabilizers and depleting the phase for α -stabilizers, leading to an unstable ferrite, transforming into secondary or tertiary austenite[20]. This causes a reduction in corrosion resistance of duplex steels. Since the χ -phase often coexist, it is difficult to separate inherent effects of χ -phase from those of σ -phase on corrosion and mechanical properties[7]. χ -phase is commonly found in SDSS in the temperature range 750°C to 850°C . It contains even more molybdenum than σ and nucleates in the first stages of aging, prior to σ [21, 22, 23]. The secondary and intermetallic phases will be further described in Section 2.2.1.

2.1.2 Effect of alloying elements in SDSS

Some of the alloying elements in SDSS are austenite stabilizers and expand the γ -field and encourages the formation of austenite over wider compositional limits, while ferrite stabilizer contracts the γ -field and thereby encourages the formation of ferrite[12]. In this section, the most important alloying elements and how they effect SDSS will be described.

Chromium

Chromium is a ferrite stabilizer, but as can be seen from the relatively small γ -field in Figure 2.1.2, it is relatively weak and has a small temperature range from about 850°C to 1400°C . However, the main function of chromium is to improve the corrosion resistance of SDSS by forming a protective passive oxide film, especially improving the localized corrosion resistance properties. If the content is too high, intermetallic phases start to precipitate, hence the amount of chromium should be limited. Especially since chromium promotes σ -phase precipitation, as can be seen from the phase diagram in

Figure 2.1.2. Thus, the amount is usually kept in the range of 22-26 wt% for duplex steels[24].

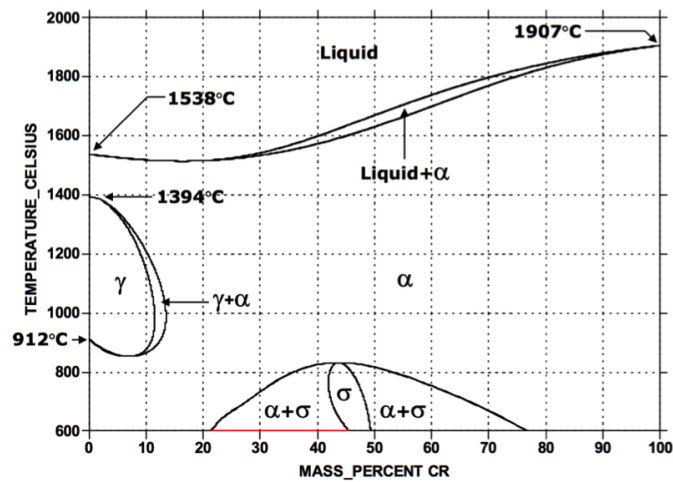


Figure 2.1.2: The Fe-Cr phase diagram[25].

Molybdenum

It is well known that a molybdenum addition of 0.5-4.0 wt% raises the pitting potential and crevice corrosion resistance of stainless steels in chloride solutions[26]. A picture of the importance of molybdenum is given by PRE_N , which claims that molybdenum is 3.3 more effective than chromium when pitting is considered. But addition above 4.0 wt% is not desirable since molybdenum may lead to formation of σ - and χ -phase at high working temperatures, due to its high diffusion rate in austenite[24, 26]. The effect of molybdenum is not well understood, but molybdenum seem to provide resistance against localized corrosion in chloride solutions stabilizing the stable passive film. When molybdenum is included as an alloying element in a stainless steel, it is incorporated into the passive film, providing resistance against localized corrosion in chloride solutions[27]. Molybdenum shows a complex oxide chemistry with different states of oxidation. Hexavalent molybdenum is found to be enriched at the surface, whereas tetravalent states show a more homogeneous distribution through the film[27]. Others have proposed that the effect of molybdenum should not be found in enrichments in the oxide film, but rather to increase the pitting resistance of stainless steels by blocking active sites during active dissolution by dissolving inside pits or crevices favoring repassivation[28, 29]. The thickness of the passive film is found to increase almost linearly with increasing molybdenum content[26]. It has also been found that presence of a certain amount of chromium is necessary for molybdenum to improve the pitting resistance in SDSS[26].

Tungsten

At the time of this writing, there is much debate in the oil and gas community in Norway and in ISO standardization committees as to whether tungsten, a ferrite stabilizer, has a beneficial effect on localized corrosion resistance of SDSS[30]. In the work of Kim and Kwong[7] it was found that by adding tungsten in the alloys, precipitation of χ -phase along grain boundaries was promoted. This indicates that tungsten is a strong χ -stabilizer. Thus, the authors claim that nucleation and growth of σ -phase was inhibited by depleting tungsten and molybdenum around the χ -precipitates. Both Kim and Kwong [7] and Ogawa et al. [4] propose that substitution of molybdenum by tungsten delay the formation of intermetallic phases towards longer holding times, and Anh et al. [31] found tungsten and molybdenum to increase the pitting potential (E_p) in almost the same amount. However, several studies have also reported that tungsten additions in duplex steels accelerates the precipitation rate of intermetallic phases, and stabilizes them towards higher temperatures[8, 9].

The improved corrosion resistance by tungsten addition may also be result of the difference in diffusion rate between tungsten and molybdenum. It has been reported that the diffusion rate of tungsten at 850°C is 10 to 100 times slower than that of molybdenum in iron or ferrous alloys[32]. Jeon et al.[33] suggested that tungsten substitution only retards the precipitation of the intermetallic phases effectively in the early stage of aging, but that the effectiveness of tungsten substitution decreases as aging time increases. The authors reported that tungsten improves the overall pitting corrosion resistance, by tungsten strongly favoring the precipitation of χ -phase. Precipitation of χ -phase during the early stages of aging depletes molybdenum and tungsten along grain boundaries, reducing the driving force for σ -phase formation. Due to relatively long temperatur holding time of more than 600 seconds, the main criticism to Jeon, et al.[33], is that the experiments are not representative of the temperature profiles experienced during welding.

Although the effect of tungsten on localized corrosion resistance on duplex steels has not been studied to the same extent as other alloying elements, such as chromium, molybdenum, and nickel, researchers seems to agree that an optimal tungsten concentration does exists. When the tungsten concentration is outside of this range, tungsten is either ineffective or detrimental[7, 4]. Ogawa et al.[4] reported that addition of tungsten had a positive effect up to 2 wt%, where there is an improvement of pitting corrosion resistance without heavy loss of impact toughness in the heat affected zone (HAZ). However, a tungsten addition greater than 3 wt% decreased both the pitting corrosion resistance and the mechanical properties in HAZ by accelerating the precipitation of intermetallic compounds during the heat treatment[4]. These precipitates occur to a greater extent with increasing tungsten content. In the base metal, the

pitting corrosion resistance improves linearly when tungsten is added. At a tungsten content of less than 2 wt%, fewer precipitates are found[4]. Kim and Kwon[7] found the retracting of σ -phase precipitation to be most dominant when an alloy contained 1.5 wt% tungsten and 3 wt% molybdenum, compared to alloys without tungsten and 3 wt% molybdenum or with 2 wt% of each.

Haugan et al.[13] investigated and compared the localized corrosion properties of UNS S32750 without tungsten and UNS S39274 with a tungsten content of 2 wt%. By anodic cyclic potentiodynamic polarization (CPP) it was found that tungsten increases critical pitting temperature (CPT), as illustrated in Figure 2.1.3. CPT was calculated as the mean temperature between the temperature of the last transpassive potential (E_{trans}) and the first repassivation potential (E_{RP}). Tungsten was in this study found to improve the CPT of SDSS, with the strongest effects on crevice corrosion resistance. The electrochemical measurements performed in this work gave a CPT of 85°C for UNS S39274 against 70°C for UNS S32750[13].

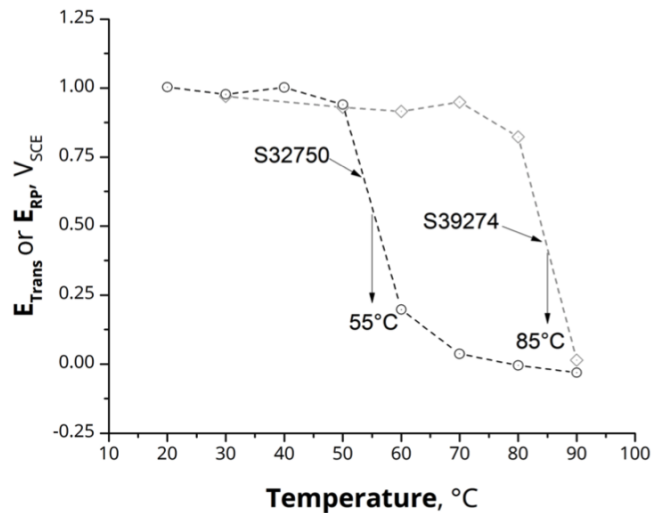


Figure 2.1.3: CPT calculated as the mean temperature between the temperature of the last E_{trans} and the first E_{RP} potential of UNS S32750 and UNS S39274[13].

Nilsson et al.[9] suggested that partial substitution of molybdenum by tungsten caused a more rapid growth of intermetallic phases, and the authors concluded that high-W (i.e. 2.16 wt% W) in SDSS had a faster σ -phase precipitation kinetics than W-free and low-W SDSS. Which indicates the opposite of the findings by Kim and Kwong [7] and Ogawa et al. [4]. However, both opponents and advocates of tungsten addition reports tungsten to be a strong χ -stabilizer.

It is still unclear whether tungsten is enriched in the passive film as tungsten oxide (WO_3) or if tungstate (WO_4^{2-}) inhibit the electrolyte inside pits and crevices[30]. Tung-

sten is present in the passive film in a hexavalent state, and while hexavalent molybdenum oxides in the passive film dissolves at potentials well below oxygen evolution, the stability of hexavalent tungsten oxide extends to anodic potentials of several tens of volts[10]. One of the proposed mechanisms is the direct reaction of W with water to form WO_3 which interacts with other metallic oxides to increase the stability of the passive oxide layer[34]. It is assumed that tungsten increases the ion density in the passive film, due to ions considered to be WO_4^{2-} , on the basis of their time constant and surface analysis data. Irzho et al.[34] propose tungsten to improve the passivity of stainless steels by interaction with the positive ions and because of its inhibitive effect. Whereas Chen and Wu[35] found that the passive films of low tungsten steels do not offer a good resistance to Cl^- ions. If the tungsten content is increased, the oxidized tungsten ion will remain on the metal surface when the insoluble oxide WO_3 is formed, which can enhance the stability of the oxide layer and improve passivation[35].

Nitrogen

Nitrogen is an austenite stabilizer and is mainly partitioned to austenite, but the content of nitrogen in ferrite increases with increasing temperature. As a consequence of this, nitrides are bound to form during rapid cooling from high temperatures as ferrite is supersaturated with nitrogen. This is because only diffusion of the interstitial elements is fast enough to allow transport over distances similar to the austenite spacing during rapid cooling. Thus, equilibrium conditions are not reached[19]. These nitrides are often referred to as quenched-in nitrides since they are limited in the ferrite grains when the temperature is rapidly decreased[19]. Nitrides can also form during isothermal heat treatments in their thermodynamic stability range. Isothermal precipitation of nitrides occurs at grain boundaries, but can be avoided by adjusting the heat treatment temperature. The quenched-in nitrides are more difficult to avoid since they form during quenching after heat treatments or welding[19].

Since nitrogen is strongly enriched in the austenite it improves the corrosion resistance in SDSS. By reducing the activity of chromium and molybdenum in ferrite, nitrogen has also been proven to reduce the tendency for σ -phase precipitations. Indicating that a high nitrogen content would allow further increase of the chromium and molybdenum content in the steel, and thus corrosion resistance[3, 14]. With respect to corrosion resistance, a higher nitrogen level is not beneficial by itself, but needs to be paralleled by increasing molybdenum and decreasing chromium contents[14]. Since nitrogen leads to a higher volume fraction of austenite, the content of the other austenite forming element, nickel, also has to be considered to obtain an equal volume fractions of ferrite and austenite in SDSS[3, 14].

Nitrogen can also improve the localized corrosion resistance and inhibit pit growth

by forming ammonium ions that could be combined with active oxidants, and thereby buffering the local pH in the pit[36]. It is proposed that nitrogen inhibits the anodic dissolution by covering kinks and steps in the surface, as a result of the slow reaction of nitrogen with protons during anodic dissolution[37, 38]. Jargelius-Pettersson[11] showed that alloyed nitrogen have a marked beneficial effect on pitting resistance as expressed by CPT. In the presence of a higher level of molybdenum, a more distinct effect of nitrogen was observed, demonstrating the synergistic effect of these alloying elements. There was also observed a reduced beneficial effect of nitrogen at higher nitrogen levels[11]. Nitrogen as an alloying element results in good weldability, since it acts as an effective austenite stabilizer during welding, attaining the preferred ratio of phases after high-temperature ferritization[19].

Nickel

As can be seen from the Fe-Ni phase diagram in Figure 2.1.4, nickel is an austenite stabilizer and its main function is to balance the high content of ferrite stabilizers and to control element partitioning. The phase diagram shows a wide and open γ -field, that even expand to room temperature at high amount of nickel. Another advantage with nickel additions is increased resistance to particularly pitting and crevice corrosion. Since a high nickel content accelerates formation of austenite in ferrite, the material gets more brittle with additions of nickel[1, 24]. Nickel, as well as nitrogen, is known to lower the temperature for σ -phase precipitation, but while nitrogen is found to reduce the partitioning of chromium and molybdenum, nickel enhances the partitioning ratio of these two alloying elements[14].

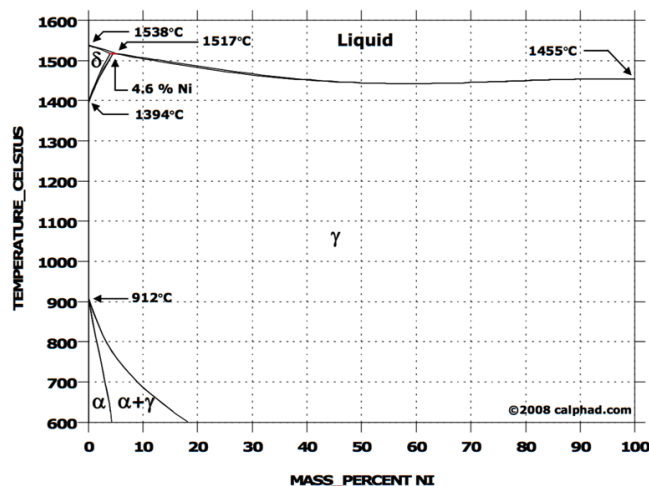


Figure 2.1.4: The Fe-Ni phase diagram[39].

Manganese

Manganese stabilizes the austenite, but it is not as effective as nickel in stabilizing this phase. Thus, nitrogen is simultaneously added with manganese in duplex steels to balance a decrease in the nickel content[23]. Manganese is generally regarded as detrimental, and for two evaluations of PRE expressions, it has been given a negative coefficient. However, some works have found the effect to lack statistical significance, but when Jargelius-Petterson[11] compared results, it was apparent that increasing manganese content had a detrimental effect on pitting corrosion. This despite, addition of manganese to stainless steel has been used to increase the solubility of nitrogen and molybdenum, both of which have a strong beneficial influence on the pitting resistance[27].

2.2 Effect of heat treatment of SDSS

Duplex stainless steels are exposed to high temperatures during heat treatments and welding. As previously mentioned, heat treatments and holding time at higher temperatures greatly affects the precipitation rate and amount of intermetallic phases in duplex stainless steels. The temperature range of 400°C to 1000°C causes the most concern, since that is when precipitation mainly occurs.

The heat treatment of duplex steels above 1000°C is often referred to as solution annealing, and is primarily conducted to dissolve phases, to relieve internal stress, and to soften the material. Solution annealing is performed by heating the material at a required temperature for a holding time that allows the necessary changes in microstructure. Thus, diffusion of the alloying elements is promoted, giving similar properties for the two phases. The annealing temperature affects the microstructure in both phases and thus the corrosion resistance, since the microstructure affects the precipitation nature of intermetallic phases. It is during solution annealing above 1000°C that SDSS obtain their optimal microstructure with equal amount of α and γ , since this is when ferrite transforms into austenite. The higher the annealing temperature, the higher the amount of ferrite[40]. To avoid precipitation during cooling, research has been done to determine the optimal solution annealing for SDSS. For duplex stainless steels, this can be achieved by solution annealing at temperatures in the range of 1050°C to 1150°C, followed by a rapid quenching[41]. The cooling to room temperature should be rapid, such as water quenching, to avoid exposure in the temperature range 600°C to 950°C, which can lead to precipitation of intermetallic phases. During solution annealing interstitial elements diffuse rapidly, while the distribution of alloys like chromium, molybdenum, nitrogen, and nickel remains nearly unchanged. Since the phase vol-

ume fraction of ferrite decreases with decreasing temperature, there are a higher concentration of chromium and molybdenum in this phase. Whereas a larger austenite volume fraction leads to lower concentration of nitrogen and nickel in austenite, making ferrite and austenite the only phases thermodynamically stable in SDSS at high temperatures[1, 3, 21]. Thus, the steels form a microstructure with alternating ferrite and austenite lamellas during solution annealing[40].

As mentioned, SDSS are prone to formation of secondary and intermetallic phases during heat treatments and welding[5]. A summation of the different secondary and intermetallic phases precipitating and at which temperatures and holding times, can be made into a temperature-time-transformation (TTT) diagram. The TTT-diagram for UNS S32750 can be found in Figure 2.2.1[21].

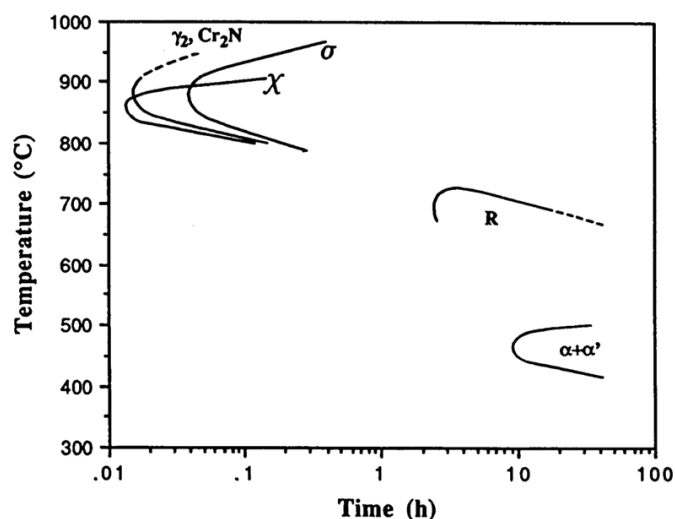


Figure 2.2.1: The TTT-diagram of UNS S32750[21]. The R and $\alpha + \alpha'$ phase are not further described in this work.

As can be seen from TTT diagram in Figure 2.2.1, secondary and intermetallic phases may form in the temperature range of 400°C to 1000°C. The residence time should especially be held short between 800°C and 1000°C to avoid precipitation of the most undesirable secondary and intermetallic phases like σ -phase, χ -phase, γ_2 , and Cr_2N . σ precipitation is most critical and can both drastically decrease the toughness of the material and weaken the corrosion resistance properties. At lower temperatures and shorter holding times other phases such as χ will precipitate. It may form after cooling from high temperatures or after holding times at temperatures between 650 and 950°C, depending on the alloy[5].

2.2.1 Intermetallic precipitates and secondary phases

Intermetallic and secondary phases can be expected to have unfavorable effect on the local corrosion resistance of duplex steels, particularly in highly oxidizing environments. This can either be an effect of low corrosion resistance of the intermetallic phase, or by depleting the parent phase and thereby introducing a weakness in the passive film. The most researched intermetallic phase in stainless steels is σ , which is a complex intermetallic phase that occur primarily in ferrite, but also in austenite. χ -phase are related to the σ -phase, a phase that only can occur in alloys that contain molybdenum. Both of these intermetallic phases are hard and brittle, and do generally reduce the toughness and the ductility in room temperature[42]. Figure 2.2.2 show formation of χ -phase and γ_2 , and growth of σ -phase in a cast duplex steel grade.

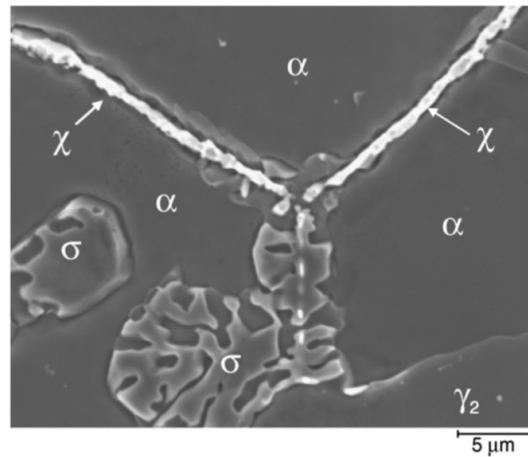


Figure 2.2.2: Formation of χ -phase and γ_2 , and growth of σ -phase in a cast duplex steel grade[22].

σ phase

The phase that causes most concern is σ , since it has a relatively large volume fraction and reduces both mechanical properties, like ductility and toughness, and corrosion resistance significantly. Since σ -phase forms by a diffusion assisted transformation, chromium and molybdenum accumulate in the σ -phase. The precipitation of this phase depletes the surrounding regions of chromium and molybdenum, leading to a decrease in corrosion resistance. The growing σ -phases will not only consume chromium and molybdenum from the ferrite, but also from the primary austenite. It tends to precipitate at the ferrite/austenite interface or at twin boundaries within the austenite phase[2, 15, 18].

The partitioning of chromium and molybdenum are crucial since the σ -phase has a high content of these elements. It is because of ferrite having a higher amount and mobility of these elements than austenite, that the sigma precipitation occurs in this phase. As the precipitation continues, chromium and molybdenum diffuse from the ferrite to the σ -phase, causing ferrite to simultaneously transform into austenite. The chromium content in ferrite is only decreasing slightly, while the molybdenum content decreases rapidly. This forces molybdenum to diffuse from inner parts of the ferrite matrix, indicating molybdenum to mainly control the σ -phase precipitation. At 900°C, the molybdenum diffusion is about twice as fast as the chromium diffusion. Nucleation of σ mainly occurs on the ferrite–ferrite and ferrite–austenite grain boundaries. Afterwards, the nuclei grows into the adjacent ferrite grains or on triple junctions where two austenite grains meet one ferrite region. The σ -phase tends to grow into the ferrite phase, where former ferrite is transformed into σ -phase and γ_2 [5, 18, 21]. This often gives a lamellar morphology, but at higher temperatures, it may assume other morphologies[17]. The regions depleted with chromium and molybdenum may influence the location of pitting sites[43].

The formation of σ can in many cases be suppressed by appropriate heat treatment. By solution annealing SDSS at high temperatures, the ferrite content will increase, thus diluting ferrite from its stabilizing alloys. A rapid quenching from high annealing temperatures will prevent the formation of σ -phase, but favor the formation of chromium nitrides[18]. Since σ is hard and brittle, its presence in stainless steels will reduce the toughness and ductility, but can increase their strength. At high temperature applications it has even been considered a strengthening agent. The problem, as with other hard phases, is to achieve fine dispersion and avoid continuous networks.[42]

χ phase

The χ -phase is usually present in a much smaller scale than the σ -phase and in contrast to the σ -phase, the precipitation of χ -phase is thermodynamically unstable in duplex steels. χ -phase is commonly formed in SDSS in the temperature range 750-850°C. It contains even more molybdenum than σ and nucleates in the first stages of aging, prior to σ . The χ -phase starts to transform to σ when the σ -phase start to precipitate. Residues from partial soluted χ -phase can often be found in the σ -phase located at the former grain boundaries. This is shown in Figure 2.2.2 where the beginning σ -phase forms, as the χ -phase transforms in favor of the σ -phase. The growth of χ - and σ -phase further depletes chromium and molybdenum in the ferrite. Hence, ferrite phase with high nickel content becomes unstable and eventually transforms into secondary austenite. Some studies claims that the χ -phase has unfavorable effects on corrosion and toughness properties, but that it can be difficult to separate from that of σ -phase

since they often coexist. It has been claimed that the pitting temperature becomes lower when χ -phase precipitates since it consumes chromium and molybdenum, and since γ_2 forms simultaneously, it becomes poor in these elements.[21, 22, 23] However, the effect of χ versus σ is not well explained in the literature and authors do not agree on this issue.

As described in Section 2.1.2, tungsten is a χ -stabilizer, so the precipitation of χ -phase will increase with increasing tungsten concentration. There may be a retardation of the growth of the σ - and χ -phases when tungsten is added to the alloy. This is because of the inherent difference in diffusion rate between tungsten and molybdenum as mentioned in Section 2.1.2[32]. The reason why precipitation of χ -phase is preferred relative to σ -precipitation seems to be closely associated with the retardation of the precipitation of σ -phase. Since there are required high concentrations of molybdenum and tungsten to form σ -phase, precipitation of χ -phase in the alloy during the initial period of aging is preferred. This is because the χ -phase can inhibit nucleation and growth of σ -phase by depleting tungsten and molybdenum adjacent to the χ -precipitates[33].

Secondary austenite, γ_2

Nilsson and Wilson[44] found pitting attack to initiate preferentially in secondary austenite, and suggested it to be a result of lower concentrations of chromium and nitrogen in this phase. The combination of poor chromium and nitrogen content together with the observation of pitting corrosion in association with γ_2 , supported the conclusion that γ_2 can be as detrimental to pitting corrosion as σ -phase. A γ_2 phase can be formed independently by diffusion at high temperatures. The rejection of chromium and molybdenum and the absorbance of nitrogen makes this phase a poorer corrosion resistor than the previously formed γ . γ_2 can grow from austenite towards the ferritic phase or be formed by heterogeneous nucleation in intergranular chromium nitride particles, as can be seen in Figure 2.2.3[17]. The γ_2 formed at α/γ phase boundaries has been found to be poor in chromium, particularly when chromium nitrides precipitates simultaneously. This explains why pitting attacks can occur in these areas, as well as why pitting can be a problem even if the amount of σ -phase is considered to be negligible[21].

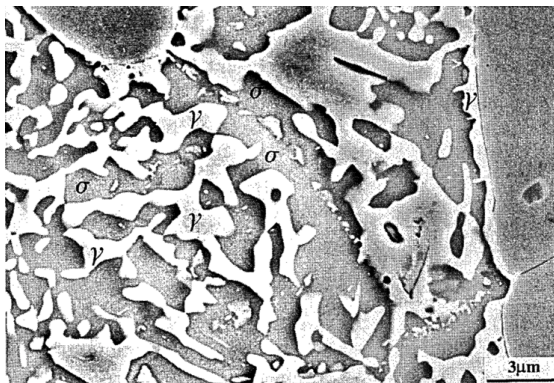


Figure 2.2.3: SEM of UNS S32750 aged for 72 hours at 700°C, showing decomposition of ferrite into σ -phase and γ_2 [21].

Chromium nitrides, Cr_2N

The duplex grades have high levels of nitrogen and chromium, and are thus particularly susceptible to precipitation of chromium nitrides[21]. Most studies of nitrides have only found precipitation of Cr_2N in duplex stainless steels, while precipitation of CrN are less common. This may be due to the higher thermodynamic driving force for formation of Cr_2N compared to CrN [19]. Whereas σ -phase is avoided by cooling from a high solution temperature, the conditions for chromium nitride precipitation will become more favorable and likely occur when rapid cooling takes place from a high temperature. This is a consequence of nitrogen mainly being partitioned to austenite. With increasing temperature the nitrogen content in ferrite increases as an effect of the low solubility of nitrogen in the ferrite[3, 19, 21]. Cr_2N is found to precipitate with a high density within ferrite grains when rapidly cooled from temperatures in the range 1100°C to 1250°C. Higher cooling rate results in larger nitride sizes. That can be detected in a higher fraction of the ferrite grains, but Pettersson et al.[19] found the effect to be further enhanced with increased austenite spacing. They also found chromium nitrides to primarily precipitate intergranularly or at sub-grain boundaries and defects in ferrite, while there was not found any nitrides close to adjacent austenite grains[19]. Slower cooling of DSS is suggested in order to avoid large nitrides, which is expected to give a smaller detrimental effect on pitting resistance. The slow cooling will, however, result in formation of other intermetallic phases such as σ -phase[19]. Figure 2.2.4 shows a backscattered SEM of a typical appearance of nitride precipitation in duplex stainless steels, here UNS S32750, solution annealed for 10 minutes at 1250°C, before it was water quenched.

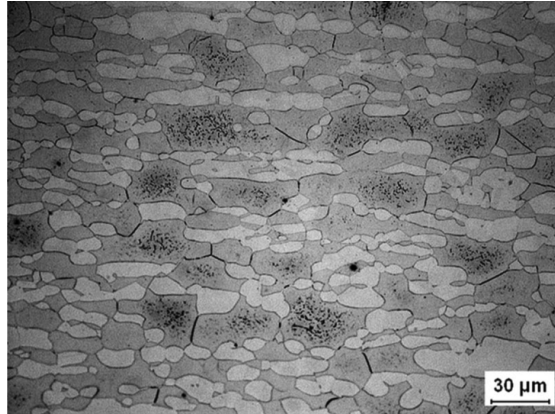


Figure 2.2.4: Typical appearance of nitride precipitation in duplex stainless steels after rapid cooling from 1250°C. Etching has revealed nitrides as mottled dark areas visible within some of the ferrite grains and along some of the grain boundaries.[19]

Chromium nitrides can also form during isothermal heat treatments in their thermodynamic stability range between 700°C and 900°C. Isothermal precipitation of nitrides occurs either on the α/α or the γ/α grain boundaries, which may affect the pitting corrosion[17, 18, 21, 19]. However, this can be avoided by adjusting the heat treatment temperature. The nitrides that develop during rapid cooling are more difficult to avoid since they form during quenching after e.g. heat treatments or welding[19].

2.3 Corrosion of SDSS

SDSS are mainly attractive because of their corrosion properties, and they are superior to some austenitic steels in many corrosive environments, although they have comparable additions of chromium and molybdenum[21]. The corrosion resistance in SDSS is mainly due to the formation of a relatively thin oxide film that forms naturally on the metal surface if dissolved oxygen is present[45]. The film is in order of 1 to 3 nm, is adherent, and have low ionic permeability[45]. It forms at high rates and protects against corrosion. The properties of the protective film depends on the chromium, molybdenum, and nitrogen content of the steel[45]. Olsson and Landolt[10] suggested that it is reasonable to assume that at least the outer part of the passive film can spread homogeneously and repair over short distances where precipitates have caused a local variation in composition. The passive films can constantly adapt to changes in potential or anion concentration in the electrolyte and consequently alters in thickness and composition with the environment[10]. Some other factors that influence the passive film are temperature, presence of halides in the electrolyte, and pH. The dy-

dynamic properties of the passive film are the reason for the high corrosion resistance of stainless steels. Passive films are formed during an exposure of the bare metal surface to oxidizing air and once a film is formed, the reaction rate between the metal and the environment will be several orders of magnitude lower. While the thickness of the passive film changes within a couple of seconds in response to a potential change, structural ordering follows considerably slower kinetics. Both of these are important factors in the growth and break down of passive films[10].

Secondary phases formed in duplex steels deplete areas of chromium and molybdenum. The depleted zones close to grain boundaries have a lower pitting potential than the surrounding grains. Thus, the film locally is less protective and the depleted zone experiences active dissolution. They will act as the anode and corrode upon exposure to corrosive environment, while the surrounding grains remain in the passive state and act as the cathode[23].

2.3.1 Localized corrosion

Localized corrosion occurs due to a local breakdown of the passive film, which can be promoted by either environmental conditions or by inclusions, selective corrosion due to high potential differences between components in the steel, and sensitized grain boundaries[45]. Localized corrosion is almost insensitive to α/γ ratio and is mainly dependent on both the bulk composition and the partitioning of alloying elements in the steel[21]. If an attack on the passive layer initiates on an open surface it is called pitting corrosion, and if it initiates on an occluded site it is called crevice corrosion[29]. There exist a critical pitting temperature (CPT) and a critical crevice temperature (CCT), below which stable corrosion do not occur at any potential up to the onset of transpassivity[46].

Pitting corrosion

Pitting corrosion is a type of localized corrosion, and the first stage of pitting corrosion is a local breakdown of the protective passive film. The breakdown of the passive film results in accelerated dissolution of the stainless steel. In an anodic CPP curve, the pitting potential can be defined as the potential above which pitting corrosion starts to grow on the metal[29, 47, 48]. Pitting corrosion is one of the most harmful forms of corrosion, since corrosion pits often provide initiation sites for fatigue cracks and stress corrosion cracks[21]. The pits are preferentially nucleated in the α/γ boundaries or inside the ferrite domains. Pitting corrosion can occur on either phase depending on the partitioning of alloying elements. Garfias et al. [49] showed that the solution

annealing temperature had a very strong influence on localized corrosion initiation. Pitting corrosion is further described in Section 2.4.

Crevice corrosion

Crevice corrosion have many similarities with pitting, such as the likelihood increases with increasing potential or chloride concentration, and that there are an existence of CCT analogous to the CPT. The alloying elements interesting in crevice corrosion resistance are almost the same as for pitting corrosion, thus alloying elements such as molybdenum have the same affect on both types of corrosion. Given the similarities between these two forms of localized corrosion, some authors have considered pitting to be a special case of crevice corrosion, and others looks at corroding crevices as large pits[50].

Crevice corrosion is a direct result of stagnant solution accumulated within crevices or holes on the metal surface. A crevice corrosion attack involves mechanistic steps such as hydrolysis, production of metal ions in the stagnant solution, and formation of critical crevice solution. An important parameter for determining the crevice corrosion tendencies of a material in a particular environment is the critical solution[51]. There are at least four different models for the initiation of crevice corrosion on stainless steels. One model is passive dissolution leading to gradual acidification and general breakdown. Others are inclusion dissolution causing thiosulphate accumulation and assisting breakdown, IR drop within the crevice forcing the metal into the active state, and stabilization of metastable pitting by the occluded crevice geometry[50]. By using two coupled electrodes to measure crevice corrosion initiation potentials and induction times for 316L stainless steel under open circuit conditions in 1 M NaCl with sodium hypochlorite added as an oxidant, Laycock et al.[50] claims that the metastable pitting model is the most suitable model for these conditions. If there are equally amounts of metastable pitting occurring both inside and outside the crevice area, and any pit within the crevice has a probability of initiating crevice corrosion, then the induction time is the time lapse before random initiation of a pit at a favorable site within the crevice. They suggested that over longer tests, crevice corrosion would occur at all temperatures where the metastable pitting rate does not reach zero with time[50].

2.3.2 Galvanic corrosion

Galvanic corrosion can occur when two dissimilar metals are in metallic contact in presence of a corrosive environment. The net current flow from the more active to the more noble metal in a closed circuit. As a consequence of this, the more active metal is

expected to corrode at a higher rate than the more noble metal in the metallic contact under open circuit conditions. Contact between dissimilar metals is often difficult to avoid, especially in metallic structures[52].

A galvanic series is an arrangement of open circuit potential (OCP) in a given electrolyte of different metals and alloys. The galvanic corrosion rate gets higher when two dissimilar metals are in electrical contact in an electrolyte, and thereby higher OCP differences. Other factors that affect the corrosion rate are area, geometry, environmental factors, potential difference, temperature, dissolved oxygen content, and chlorination[53].

2.4 Pitting corrosion

2.4.1 Mechanism

Pitting corrosion happens in various stages, first is the breakdown of the passive film, then metastable pitting and in the end, pit growth. Any of these stages may be considered the most rate-limiting, like once the passive film breaks down and a pit initiates, there is a change that there will be a stable pit grow. In hope to predict and understand pit initiation, the structure and composition have been studied widely[29].

Passive film breakdown

The breakdown of the passive film and the early initiation of the pitting process is the least understood part of the pitting process. This may partly be because it happens extremely rapidly and at a very small scale. The thickness, composition, structure, and protectiveness of the passive film is dependent of the alloy composition, potential, environment, and exposure history. [29]. The breakdown of the passive film and initiation of pitting results in accelerated dissolution of the stainless steel, and is often categorized in three main mechanisms, passive film penetration, film breakage, and adsorption. However, pits in stainless steels are most often associated with inclusions or secondary phases[29]. Film penetration involves transport of aggressive anions through the passive film where aggressive dissolution is promoted[54]. The penetration mechanism is supported by the induction time for pitting and the following introduction of chloride into the electrolyte.

Metastable pitting

Metastable pits are pits that initiate and grow for a limited time before repassivating, often with a lifetime in the order of seconds or less. An illustration of metastable pitting before E_p in a potentiodynamic polarization curve is shown in Figure 2.4.1. Metastable pits are able to form under conditions where stable pits do not form, and they often act as precursors to stable pits under conditions where stable pits will form. The pits that are considered metastable are typically those of micron size. Larger pits can also stop growing for different reasons, but they are not considered metastable. For a period, metastable pits can initiate at potentials far below E_p , where the stable pits initiate, and at potentials above E_p during the induction time before the onset of stable pitting. This provides evidence against the definition of E_p being the potential above which pits initiate. Small stable pits behave identically to metastable pits, and are in fact metastable. Stable pits will survive the metastable phase and continue to grow, whereas metastable pits repassivate and stop growing[49]. Rupture of the cover during metastable growth leads to repassivation of the pit. Pit growth is stabilized if a salt film precipitates on the pit surface before the cover ruptures[55].

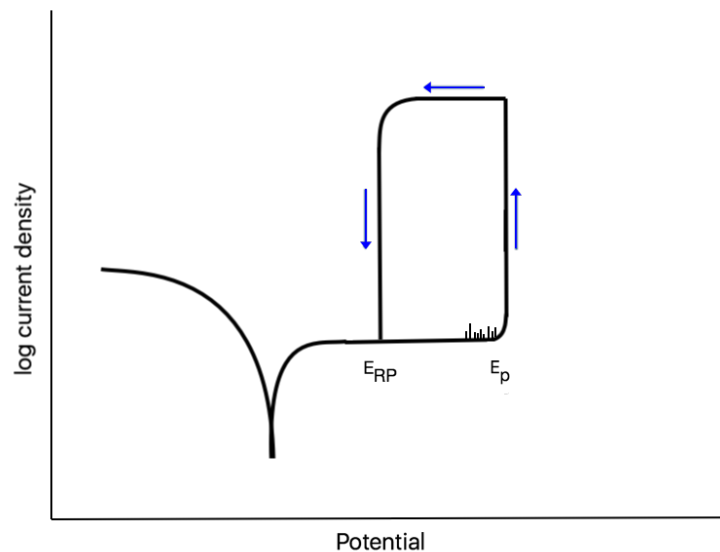


Figure 2.4.1: Illustration of a metastable pitting before E_p in a potentiodynamic polarization curve.

It has been suggested, after many investigations of metastability, that metastable pits in stainless steels are covered by a layer over the pit mouth during growth. The layer is suggested to be the remnant of the undermined passive film[29, 49]. Larger pits can be covered with a metal layer detached from the rest of the metal. It is often of

a considerable thickness and do still remain reflecting, making optical detection of the pits extremely difficult. The whole pit can be revealed by removing the cover by a short exposure to ultrasonic agitation[29]. Metastable pits grow on stainless steels with covers by undercutting the passive film. To allow flow of electrolyte into the pit and metal ions out of the pit, these covers must be sufficiently porous. There are not possible to see the pores in the cover by SEM, and therefore the diameters must be less than $\sim 50 \mu\text{m}$. Large resistances and thus ohmic potential drops may develop as a result of the constriction of current flow by the pores[55]. This cover provides an extra diffusion barrier that helps to maintain a concentrated aggressive environment inside the pit[49].

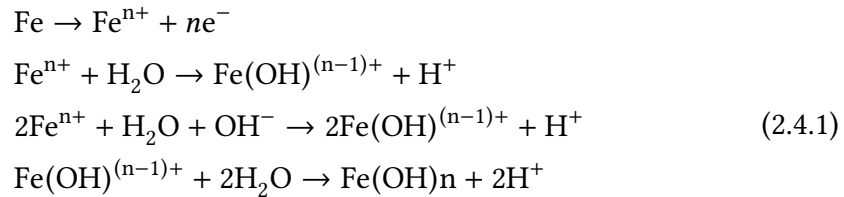
Laycock and Newman[56] have shown that it is not always necessary with salt precipitation to stabilize metastable pitting. In other words pits can be stabilized both with or without a salt film if the pit environment is concentrated enough to avoid repassivation. For metastable pits that grow without a salt film, the covers are very thin since they are remnants of the pre-existing passive film. Due to large dissolution current inside the pit during metastability, there will be partial ruptures of the cover, leading to stepwise current increases. If there is complete rupture of the cover during metastable growth, the pit will repassivate as the pit and bulk electrolytes mix, making a diluted solution environment[49, 55]. To form a salt film on the metal surface that prevents growth of passive film, a critical concentration of metal chlorides is required[49]. If the cover ruptures after a salt film has precipitated on the pit surface, the lost potential drop is compensated by an increase in the salt film thickness. Giving an increase in the potential drop across the salt film. As a result, the pit cover is no longer critical to pit stability[55]. The pit can achieve stability if the pit depth by itself is a sufficient diffusion barrier. Thus making it possible to maintain an environment that is sufficiently aggressive to prevent repassivation at the metal surface inside the pit. If the concentration on the bottom of the pit is sufficiently high to precipitate a salt film, this salt film will thicken until the anode current matches the diffusion flux out of the pit[49]. If the conditions allow a salt film to form, the pit has a greater chance to survive a rupture in the cover and become a stable pit. The reason for this is the buffering action of the salt, which can replenish the pit environment by dissolving[29].

Pit growth

The pitting initiates when the pitting potential reaches a critical value, the pitting potential (E_p). This value depends on the chemical composition of the steel, temperature, chloride concentration, and pH. E_p is the minimum potential at which localized acidity can be maintained inside a pit. This can even be obtained at early stages of pitting[57]. Pit growth may be controlled by the same factors that control any other electrochemi-

cal reaction, charge-transfer process, mass-transport, ohmic effects, or a combination of these factors[29]. For stainless steels chloride concentration is more important than pH in terms of stabilizing pith growth and to prevent repassivation. This is because pitting corrosion can only occur if there is any aggressive anodic species present[29]. Usually it is chloride ions, but not always. Chloride is an anion of a strong acid and it is relatively small with a high diffusivity, which interfere with passivation. The onset of pitting corrosion is observed as an irreversible increase in the current density (i). A higher value of E_p indicates that the steel are more resistant to pitting corrosion in the considered environment[29, 47, 57].

The reactions in Equation 2.4.1 show that the likelihood of pitting corrosion is enhanced with an increase in potential associated with oxidizing agents. During pitting, the anodic and cathodic electrochemical reactions that happens during corrosion separate spatially. All of the cathodic reactants, like oxygen, are depleted in the pit, which is exchanged with an exposed surface where there are more reactants. The pit is now enriched in iron cations and an anodic species such as chloride. To maintain a charge neutrality, the anodic species migrates into the pit and thereby balancing the cathionic charge. The acidic chloride environment generated in the pit is aggressive and propagate the pit growth in most metals[29].



Where n most usually are 2 or 3 for Fe. The first reaction is a dissolution reaction and it is followed by the second reaction, which is a simplified description of the processes taking place inside a pit, where equilibrium is very quickly reached. If it is assumed that the bulk solution could have any pH value, the second reaction has to be rewritten to account for the contribution of the OH^{-} ions at pH values higher than 7, which is shown as the third reaction. The fourth equation shows the reaction of the corrosion products[57, 29]. An illustration of these reactions is shown in Figure 2.4.2.

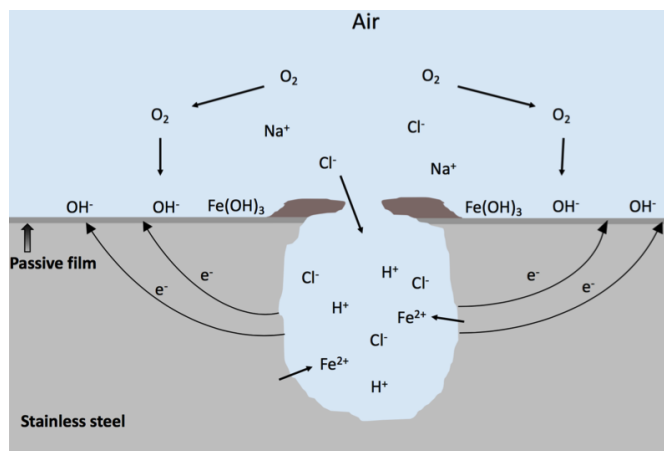


Figure 2.4.2: Illustration of the electrochemical reactions behind pitting corrosion.

The critical step

It is considered that the passive state is required for pitting to occur, but that the composition and the structure of the passive film play a minor role in the pit propagation stage. Often the metastable pitting phase is considered the most important since only the pits that survive this phase become stable growing pits[29]. However, a debate about the critical step in localized corrosion has been going on for decades. Whereas some researchers focus on the composition and structure of the passive film associated with the initial breakdown of the film, others consider the susceptibility to pitting to be controlled by the pit growth kinetics and the stabilization of pit growth[58].

Many researchers, primarily those who focus on surface analysis of passive films, consider the protectiveness of the passive film and its initial breakdown to be the critical aspects of localized corrosion. Localized corrosion can after all, only occur if a protective passive film is present and undergoes a breakdown event. They have focused their studies on linking film breakdown events to the composition and structure of the passive film[58]. The other side of the debate focuses on the stabilization of pit growth and do not look at the passive film breakdown as the critical step. They think that a high rate of passive film breakdown, for example by high rates of metastable pitting, might not be a problem. The damage resulting from frequent film breakdown and repair might be insignificant if the repair is rapid. Although it has been proposed that the frequency of stable pitting is related to the frequency of metastable pitting, this has never been proved. They think it is unlikely that metastable pitting observed many hundreds of mV below the pitting potential, could ever stabilize in the absence of a crevice. Localized corrosion is only regarded as an issue for structural reliability

when the breakdown of the passive film leads to a stable growing pit. Active pits can perforate a structure or act as initiation sites for cracks. In some cases, differences in pitting potential have been explained by differences in the kinetics of pit growth, suggesting that differences in passive film properties are not important[58]. Newman[59] found the difference in pitting potential between two alloys to be explained by differences in the pit growth kinetics, thus there is no need to consider any differences in the passive films.

To unify the two perspectives, Frankel et al. [58] suggests that both passive film breakdown and pit stabilization must occur for pitting to be a concern, and that either can be controlling. The authors suggest that under exposure to an aggressive environment and/or a material with a susceptible microstructure, pit stability considerations would determine whether or not pitting occurs. This is because the passive film breakdown will be easy and frequent. In contrast, passive film breakdown would be difficult and rare in less extreme environments and/or for less susceptible alloys and microstructures. Thus, the properties of the passive film properties and its protectiveness become the critical factors[58].

2.4.2 Kinetics and parameters

The effect of chromium, molybdenum, tungsten, and nitrogen can be estimated by a pitting resistance equivalent, PRE. It is an empirical formula developed to reflect and predict the pitting resistance of a stainless steel, based upon the proportions of mentioned alloys. Analysis in terms of PRE has often been applied to results from electrochemical and immersion testing to determine the CPT in NaCl or ferric chloride (FeCl_3) and to pitting potentials[11]. However, extreme care should be used in applying PRE expressions since it only gives a qualitative estimate of the localized corrosion resistance of an alloy. Most equations lack general validity and thus cannot be applied indiscriminately to the entire range of stainless steels available, especially if the different types are treated in the same manner. While NORSOK M-001[60] defines PRE based on chromium, molybdenum, and nitrogen, ISO 21457[61] includes tungsten in the PRE expression, as shown below.

$$\text{PRE}_N = \text{Cr} + 3.3x\text{Mo} + kxN \quad (2.4.2)$$

$$\text{PRE}_{N,W} = \text{Cr} + 3.3(x\text{Mo} + 0.5xW) + kxN \quad (2.4.3)$$

Where k is a value between 10 and 30, often 16, in Equation 2.4.2 and 2.4.3. The sub-index "N" in Equation 2.4.2 indicates a modification of the original PRE formula to

include nitrogen[21]. While the sub-index "W" in Equation 2.4.3 indicates that the PRE expression also includes tungsten[51]. All of the values in Equation 2.4.2 and 2.4.3 are given in wt%.

The corrosion resistance of a SDSS is determined by the corrosion resistance of the weaker phase, indicating that the PRE_N of both austenite and ferrite should be calculated. To obtain the best corrosion resistance, both of the phases should have the same PRE_N value. This problem can be avoided by choosing an annealing temperature which gives equal values of PRE_N , thus equal pitting resistance in the two phases. The volume fraction of austenite and ferrite as well as the partitioning behavior of chromium and molybdenum, has a strong influence on the chemical composition of the two phases and their PRE_N values [2, 3, 14, 16, 47, 62]. The ferrite volume fraction increases with increasing temperature, which makes the chromium and molybdenum more diluted in this phase. This leads to a decreasing PRE_N in the ferrite phase. A higher concentration of nitrogen and nickel is obtained in the γ phase since the austenite volume fraction gets smaller, leading to a increasing PRE_N for the austenite phase. As the annealing temperature increases, ferrite has a decreasing PRE_N , while austenite has an increasing PRE_N , as shown in Figure 2.4.3 for UNS S32750. The optimal annealing temperature can be reached when the two PRE_N -temperature curves cross each other, and it is in this condition that the PRE_N reaches the maximum value for both the austenite and ferrite phases, and the sample reaches the best corrosion resistance. Figure 2.4.3 shows a optimum annealing temperature of about 1070°C for this case. k was set to 20[47].

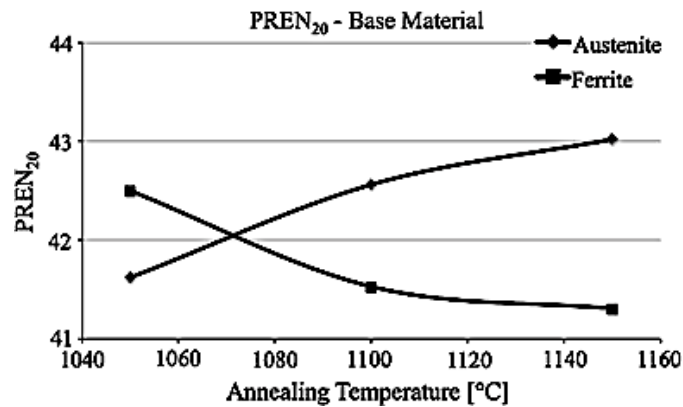


Figure 2.4.3: $PRE_{N,20}$ of ferrite and austenite phase in a UNS S32750 sample as a function of temperature, showing the optimum annealing temperature. [47]

According to NORSOK M-001[60] and ISO 21457[61], steels with PRE_N above 40 can be used in seawater up to 20°C, which is the case for all SDSS. However, the value of PRE_N is not enough to decide whether or not SDSS can be used in seawater. Together with microstructural features like ferrite/austenite proportion and the presence of intermetallic phases, parameters such as the pitting potential (E_p), the repassivating

potential (E_{RP}), the corrosion potential (E_{corr}), and the flade potential (E_{flade}), affect the pitting corrosion resistance of SDSS. According to Pourbaix [63], the pits that initiate at E_p will keep growing even if the potential is below the pitting potential. They will only stop growing if the potential is lower than E_{RP} . The repassivating potential varies with the depth of the pit, and deeper pits have a lower E_{RP} .

The different parameters can be obtained from anodic cyclic potentiodynamic polarization (CPP) curves, by reversing the sweep at a potential noble to E_p [64]. The active-passive behavior of metals in aqueous solutions can be determined from a plot of applied potential versus current density using a potentiostat. The polarization curve are made using a potentiostat which gives a continuously varying potential to the specimen and as the applied potential is varied, the current is continually recorded[23]. Figure 2.4.4 give an example of an anodic CPP curve, showing different parameters related to pitting corrosion. This can be done according to the ASTM G61 standard[65]. Pit initiation occurs once the potential for the test sample has exceeded E_p . The current density increases rapidly from a passive to a reversal current density level of the scan direction. When the sweep is reversed, the propagation process decreases in rate until it stops, and the pit repassivates at E_{RP} when the current density drops back. It is a potential dependent operation. To stabilize the pit growth and prevent repassivation, the local chloride concentration is more important than pH for stainless steel. Once a pit starts to grow in nature, further pitting is promoted[29, 48, 64].

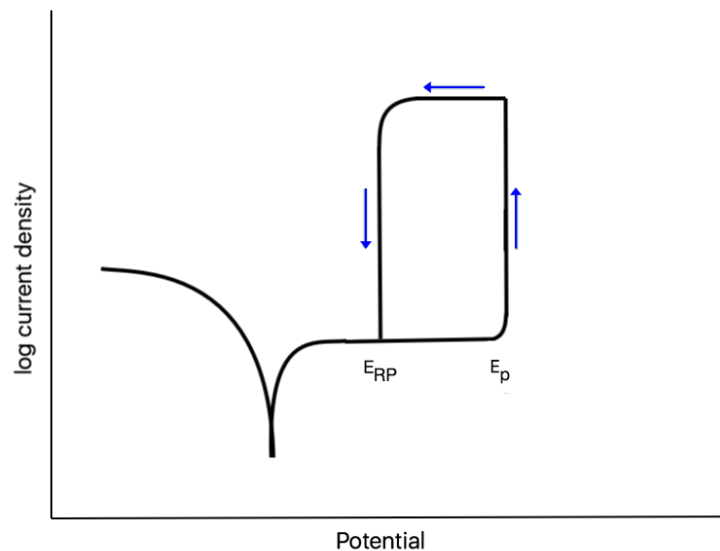


Figure 2.4.4: Illustration of a potentiodynamic polarization curve.

For the anodic CPP curves, E_p can be measured at the inflection point and E_{RP} is defined

to be where the current density is below $2\mu\text{A}/\text{cm}^2$. E_{RP} is in this thesis defined as the potential where a stable oxide film is formed. The passive current density (i_p) is defined as the average or mid point of the current density where the oxide film is formed. i_p is a measure of the protectiveness of the passive film. Qualitatively, a SDSS is considered pitting resistant in seawater if the value of $E_{RP} - E_{corr}$ is greater than 200 mV. However, it all depends on the oxidizing power of the solution, not only E_{RP} and E_p [66].

The shape of the anodic CPP curves depends both on the microstructure of the test sample and on the temperature of the electrolyte. All electrochemical response of anodic CPP curves can be grouped into three distinctive cases. The curves can show no hysteresis, high E_p and a little hysteresis, or large positive hysteresis loops with a value of $E_p - E_{RP}$ of several hundred mV[64, 67]. No hysteresis or high E_p and a little hysteresis indicates anodic dissolution and oxygen evolution caused by water oxidation. The presence of small pits together with oxygen evolution translates into small hysteresis loops. A large positive hysteresis is the case for pitting corrosion, because of elevated temperatures and/or presence of secondary and intermetallic phases[68, 69].

For many steels, pitting corrosion will not initiate at temperatures below a certain value, making temperature one of the critical factors in pitting corrosion. Extremely high breakdown potentials are observed at low temperatures, which corresponds to transpassive dissolution, not localized corrosion. When the temperature is just above a critical pitting temperature (CPT), pitting corrosion occurs at a potential far below the transpassive breakdown potential. CPT is defined as the minimum temperature for pits to form on the metal surface, and the lowest potential independent of the temperature, below which pitting does not occur[46]. The value of CPT is a measure of the resistance to stable pit propagation, and it is independent of environmental parameters. The pitting potential decreases with increasing temperature and chloride concentration at higher temperatures. For many stainless steels the CPT is in the range of 10°C to 100°C . The temperature effect of the pitting corrosion can be seen either by varying the temperature at a range of fixed applied potentials or varying the potential for a range of constant temperature experiments. Like when CPT is found by determine the inflection point of E_p as a function of temperature or according to the ASTM G48 standard[70]. CPT can also be found by exposing a test sample to a 6 wt% FeCl_3 solution, where CPT is defined as the temperature where OCP falls from approximately 700 mV_{SCE} to below 500 mV_{SCE} . The value of 500 mV_{SCE} can be explained on the basis of polarization curves, where detrimental phases or increased temperature can decrease the pitting corrosion area or increase the active area in the polarization curve. The corrosion rate depends on the intersection between the cathodic tafel slope for dissolution of trivalent iron into divalent iron with the anodic polarization curve. This intersection gives a low corrosion rate if a stable oxide film is present. If detrimental phases are present or the temperature is raised and there is damage in the oxide film,

the intersection can be found in the pitting area or in the active area of the anodic polarization curve, which gives a high corrosion rate. This will also suppress the OCP from the corrosion potential of iron to lower values, and the critical value for activation and corrosion has been found to be about 500 mV_{SCE} [71]. The test is a modified version of the ASTM G48 standard, that combines both high chloride content and high oxidizing power[71]. Like pitting potential, CPT can be used to rank the susceptibility to pitting corrosion. The higher CPT, the higher resistance the alloy has against pitting[29].

Chapter 3

Experimental work

In this experimental work, the objective was to investigate the effect of tungsten and isothermal heat treatments on the pitting corrosion properties of the two SDSS grades W-free UNS S32750 and W-rich UNS S39274. In this chapter, the procedure of isothermal heat treatments are presented first. They were performed at 790°C, 846°C and 920°C at a various selection of times. After this, the setup and procedure for the two electrochemical measurements are presented. The UNS S32750 samples isothermal heat treated at 846°C were studied in previous work, while the samples isothermal heat treated at 790°C and 920°C were studied in this work. Only the UNS S39274 samples isothermal heat treated at 846°C were studied in this work. The two electrochemical procedures were a open circuit potential (OCP) measurement while exposed in 6 wt% ferric chloride solution and recording anodic cyclic potentiodynamic polarization (CPP) curves according to the ASTM G61 standard. Results from these electrochemical measurements are going to be compared with results from corrosion testing on low-W UNS S32760 performed by another student. Microstructure characterizations was performed by another student prior to electrochemical measurements, to investigate precipitation of intermetallic and secondary phases. After electrochemical measurements, surface characterizations by optical microscope (OM) and scanning electron microscope (SEM) was performed to find the pitting corrosion morphology.

3.1 Test material

The test materials used in this work were two different SDSS grades, W-free UNS S32750 and W-rich UNS S39274. The samples were delivered by Sandvik and Sumitomo, respectively, and the chemical composition of the two SDSS grades are given in Table 3.1.1 together with the chemical composition of low-W UNS S32760. The chemical composition and other specifications can be found in the material sheets given in Appendix A.

Table 3.1.1: The chemical composition (wt%) and corresponding PRE_N and $PRE_{N,W}$ of UNS S32750, UNS S32760, and UNS S39274 used in the experimental work and in previous work. Only the major alloying elements are included, the rest can be found in Appendix A.

Standard	Cr	Ni	Mo	N	W	C	PRE_N	$PRE_{N,W}$
UNS S32750	25.6	6.42	3.83	0.293		0.014	42.9	
UNS S32760	25.2	7.1	3.6	0.2	0.62	0.02	40.3	41.3
UNS S39274	24.9	6.3	3.1	0.29	2.10	0.018	39.8	43.2

All of the samples were machined at the workshop at the Department of Engineering Design and Materials, IPM. The samples were machined from pipes with an outer diameter of approximately 210 mm (8" pipe) and wall thickness of 30 mm. Quadratic segments with dimensions 30x30 mm were machined to circular rods with diameter varying from 22 mm to 30 mm. Samples with thicknesses of 2 mm to 3 mm were cut from the circular rod. The geometry of the samples are given in Figure 3.1.1 To connect the samples to the circuit in the electrochemical measurements, the specimens had a hole with a diameter of 2.2 mm. A platinum wire was used to complete the circuit. The area of the samples was calculated from Equation 3.1.1.

$$A_{sample} = \frac{\pi \cdot d_1^2}{2} + \pi \cdot d_1 \cdot h - \frac{\pi \cdot d_2^2}{2} \quad (3.1.1)$$

Where d_1 is the diameter of the sample, d_2 is the diameter of the hole, and h is the width of the sample. The geometry of the samples are shown in Figure 3.1.1.

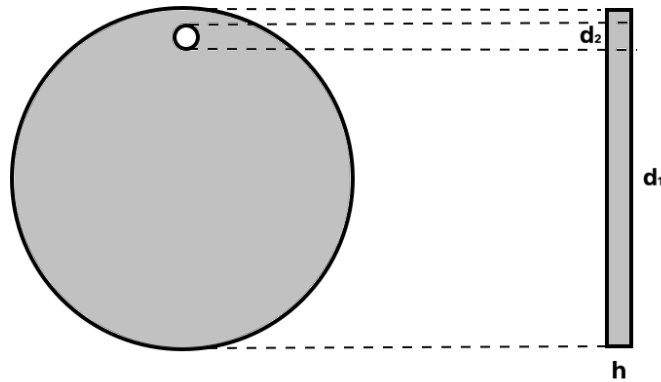


Figure 3.1.1: The geometry of the samples used in the experimental work.

3.2 Heat treatment

To obtain similar grain sizes and to remove prior heat treatment history, the samples were solution annealed prior to isothermal heat treatment. The solution annealing and the T2 and T3 isothermally heat treatments were done in a Nabertherm N17/HR chamber furnace, while the T1 heat treatments were done in a Nabertherm N15/HR chamber furnace. When solution annealed and isothermal heat treated, the samples were placed on a tray made of stainless steel foil with approximately 30 rooms for the samples, as shown in Figure 3.2.1. The heat treatment procedure can be seen in Figure 3.2.2.



Figure 3.2.1: The tray made of stainless steel, with samples placed in their rooms, used when heat treating the samples.

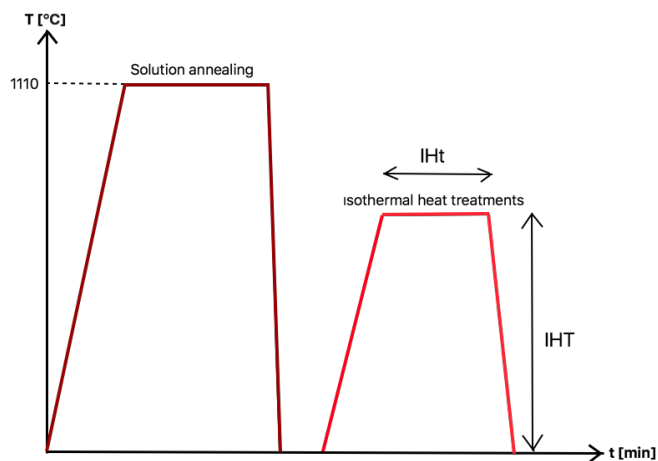


Figure 3.2.2: Illustration of the heat treatment procedure for the samples, consisting of solution annealing, followed by a water quenching and an isothermal heat treatment, followed by another water quenching.

3.2.1 Solution annealing

To dissolve inclusions and to ensure equal volume fractions of α and γ in the samples, they were solution annealed before the isothermal heat treatments. In the intention of having the same conditions for each sample from the same SDSS grade, they were solution annealed at the same time. The samples were solution annealed for 15 minutes at 1110°C, as recommended by the manufacturers, followed by water quenching at ambient temperature. To make sure the samples had the wanted temperature in the wanted time period, the time for the samples to reach 1110°C were added to the 15 minutes, making it 16 minutes. This time was found by logging the temperature in the middle of a sample at different places in the oven using a thermocouple. The heating rate was found to be 25°C/second, and the real temperatures were found to be 1083°C in the front of the oven and 1118°C in the back of the oven, as shown in Figure 3.2.3. This may affect the final result.

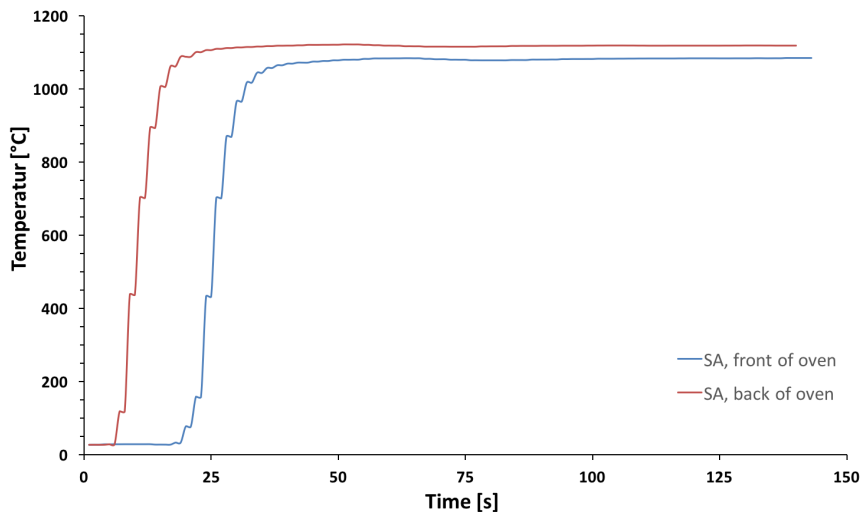


Figure 3.2.3: The temperature logging of two SDSS samples where one were placed in the front of the oven and the other were placed in the back of the oven. Giving a real temperature of 1083°C and 1118°C respectively.

3.2.2 Isothermal heat treatment

A selection of samples made of UNS S32750 and UNS S39274 were isothermal heat treated after the solution annealing. This was to provoke the formation of intermetallic and secondary phases. The isothermal heat treatments were performed at three different isothermal heating temperatures (IHT) at different isothermal heating times

(IHt). Table 3.2.1 shows the different combinations of IHT and IHt. To find which combinations of IHT and IHt that were interesting, a TTT diagram of UNS S32750 were used. The TTT diagram is shown in Figure 2.2.1 and the selected times and temperatures used in the isothermal heat treatments are shown in Figure 3.2.4 and given in Table 3.2.1 and 3.2.2. The different heat treatment conditions were selected to obtain different secondary and intermetallic phases, like σ , χ , and Cr_2N . As can be seen from Figure 3.2.4, the value of T1 was chosen close to the temperature where σ -phase and Cr_2N are expected to have the fastest precipitation kinetics. To separate the effect of the precipitation of χ -phase from that of σ -phase and Cr_2N , T2 was chosen close to the temperature where χ -phase is expected to have the fastest precipitation kinetics. T3 was chosen above the expected stability range of χ -phase to separate the affect of Cr_2N from that of σ -phase.

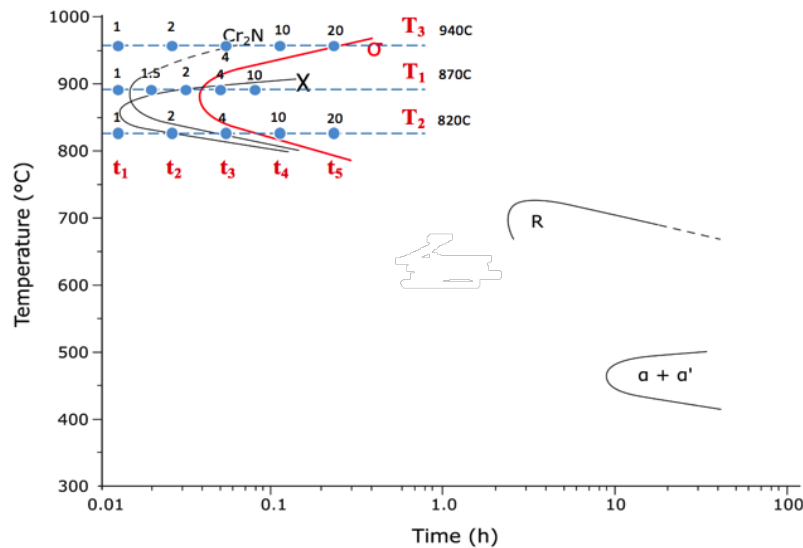


Figure 3.2.4: The TTT diagram of UNS S32750, showing the temperature and time conditions of the isothermal heat treatment of the samples. The numbers by the blue dots are the isothermal heating time given in minutes.

The selected combinations of IHT and IHt, and the number of samples for each heat treatments can be found in Table 3.2.1 and 3.2.2, together with the observed intermetallic precipitations and secondary phases for that heat treatment. The detection of intermetallic precipitations and secondary phases was performed by another student[72].

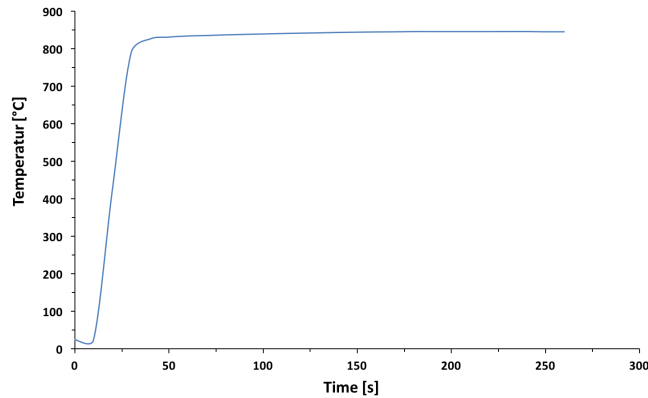
Table 3.2.1: The number of samples and temperature, time conditions of isothermal heat treatment, and observed intermetallic precipitations and secondary phases for UNS S32750.

Number of samples	Heat treatment	Temperature [°C]	Time [min]	Secondary phases
8	As-delivered			-
8	Solution annealed	1110	15	-
8	T1t1	846	1	-
8	T1t2	846	1.5	-
8	T1t3	846	2	σ, χ
2	T1t4	846	4	σ, χ
0	T1t5	846	10	σ, χ
2	T2t1	790	1	-
2	T2t2	790	2	-
8	T2t3	790	4	σ, χ
0	T2t4	790	10	σ, χ
2	T2t5	790	20	σ, χ
2	T3t1	920	1	-
2	T3t2	920	2	$\sigma, \text{Cr}_2\text{N}, \chi$
8	T3t3	920	4	$\sigma, \text{Cr}_2\text{N}, \chi$
0	T3t4	920	10	$\sigma, \text{Cr}_2\text{N}, \chi$
2	T3t5	920	20	$\sigma, \text{Cr}_2\text{N}, \chi, \gamma_2$

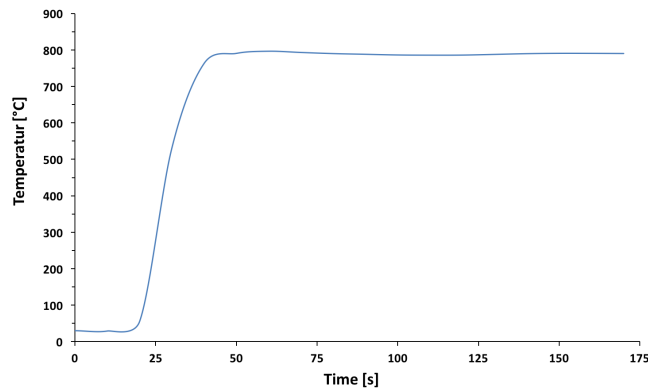
Table 3.2.2: The number of samples and temperature and time conditions of isothermal heat treatment of UNS S39274.

Number of samples	Heat treatment	Temperature [°C]	Time [min]	Secondary phases
8	As-delivered			-
8	Solution annealed	1110	15	-
8	T1t1	846	1	-
2	T1t2	846	1.5	-
2	T1t3	846	2	-
8	T1t4	846	4	σ, χ
8	T1t5	846	10	σ, χ

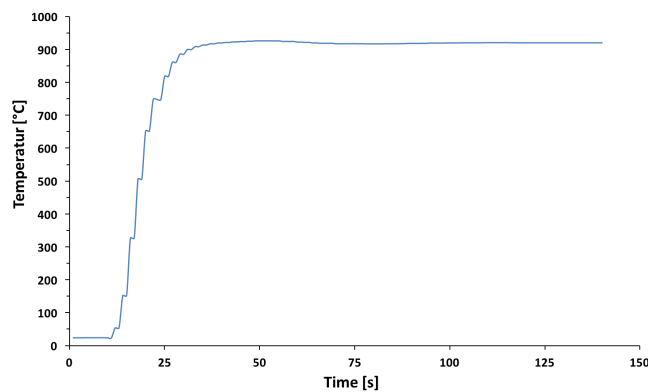
To investigate whether the temperature in the oven was the same as the set temperature, a K-type thermocouple logged the temperature in the middle of a sample during isothermal heat treatments at the different IHT. Since all of the samples were isothermal heat treated in the front of the oven, the temperatures were logged there. The result of the temperature logging, given in Figure 3.2.5, showed lower temperatures than the set temperatures, giving T1 of 846°C, T2 of 790°C, and T3 of 920°C. These are the temperatures used in this work.



(a) The temperature logging of a SDSS sample isothermal heat treated at 870°C in the front of the oven, giving a real temperature of 846°C.



(b) The temperature logging of a SDSS sample isothermal heat treated at 820°C in the front of the oven, giving a real temperature of 790°C.



(c) The temperature logging of a SDSS sample isothermal heat treated at 940°C in the front of the oven, giving a real temperature of 920°C.

Figure 3.2.5: Temperature logging of SDSS samples at the three different IHT, showing lower temperatures than the set temperatures.

3.3 Electrochemical measurements

To investigate the effect of isothermal heat treatment two electrochemical measurements were performed. CPT measurements by OCP exposure in a 6% ferric chloride solution and anodic CPP measurements according to the ASTM G61 standard. Before the electrochemical measurements the samples were ground with 320, 500, 1000, 2000, and 4000 SiC paper, using water as lubricant. This was followed by polishing with 3 μm and 1 μm diamond spray. After grinding and polishing, and between the two diamond spray sizes, the samples were rinsed in an ultrasonic bath with ethanol for 3 minutes. After that they were rinsed with ethanol and distilled water, air dried and stored in a desiccator for at least 24 hours for passivation.

3.3.1 Critical pitting temperature measurements

CPT of the test samples was obtained OCP exposure in a 6% ferric chloride solution, a solution taken from the ASTM G48 method[71]. The temperature at which pitting corrosion could be observed was termed CPT[71]. The electrolyte for this test was made by dissolving 100 g $\text{FeCl}_3 \cdot 6\text{H}_2\text{O}$ in 900 mL distilled water, which gave about 6 wt% FeCl_3 . A magnet stirrer at ambient temperature was used to dissolve the salt. The electrolyte was preheated in a 1000 mL beaker on a heating plate before the test samples were immersed. OCP was recorded and logged while the samples were immersed in the electrolyte. The samples were held at the same temperature for 24 hours, and if the OCP was above 500 mV_{SCE} , the temperature was increased by 5°C and held at that temperature for another 24 hours. This continued till OCP was below 500 mV_{SCE} , which indicates that the SDSS was in the active area and pitting had occurred. After the test, the samples were removed and rinsed with distilled water. The starting temperature was set to be 40°C, and two samples from chosen heat treatments were tested at the same time.

The test setup is illustrated in Figure 3.3.1 and an overview of the test setup is shown in Figure 3.3.2. The different components are numbered and specified in Table 3.3.1. Specifications of the samples tested with this method are given in Table 3.3.2. Surface characterization prior to electrochemical measurements showed a later precipitation of secondary phases for the T1 isothermal heat treatment for UNS S39274 than for UNS S32750. Therefore it was decided to add an extra isothermal heat treatment time in the test matrix for UNS S39274 called T1t5, isothermal heat treated for 10 minutes. The OCP measurements on solution annealed and T1 conditions for UNS S32750 was performed during the project work[73].

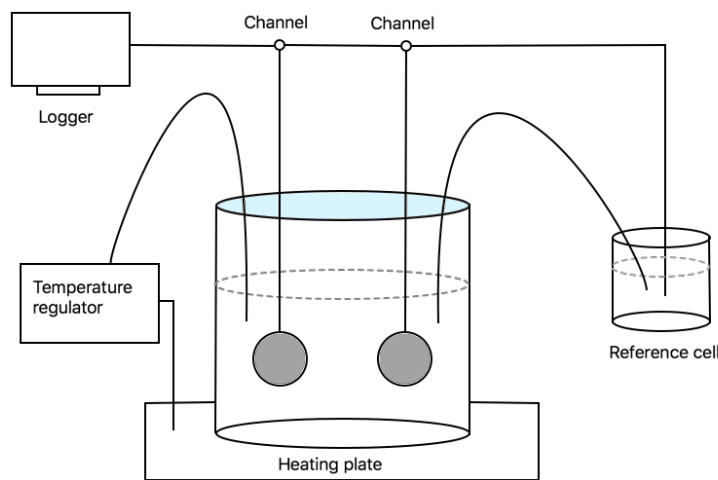


Figure 3.3.1: Illustration of the test setup for the CPT measurements.

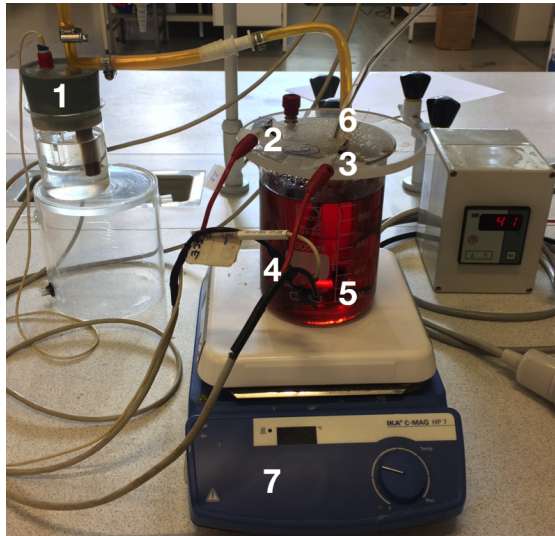


Figure 3.3.2: An overview of the test setup for the CPT measurements.

Table 3.3.1: Specifications of the numbered components in the test setup in Figure 3.3.2.

Number	Specification
1	Reference cell with reference electrode
2	Logging channels
3	Test samples
4	Temperature regulator
5	Heating plate

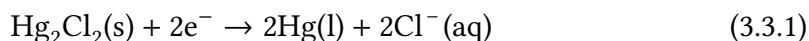
Table 3.3.2: Specifications of the samples used to obtain CPT.

Sample name	Heat treatment temperature [°C]	Isothermal heating time [min]
AD-1, AD-2	-	-
SA-1, SA-2,	1110	15
T1t1-1, T1t1-2	846	1
T1t2-1, T1t2-2	846	1.5
T1t3-1, T1t3-2	846	2
T1t4-1, T1t4-2	846	4
T2t1-1, T2t1-2	790	1
T2t2-1, T2t2-2	790	2
T2t3-1, T2t3-2	790	4
T2t4-1, T2t4-2	790	10
T2t5-1, T2t5-2	790	20
T3t1-1, T3t1-2	920	1
T3t2-1, T3t2-2	920	2
T3t3-1, T3t3-2	920	4
T3t4-1, T3t4-2	920	10
T3t5-1, T3t5-2	920	20
W-AD-1, W-AD-2	-	-
W-SA-1, W-SA-2	-	-
W-T1t1-1, W-T1t1-2	846	1
W-T1t2-1, W-T1t2-2	846	1.5
W-T1t3-1, W-T1t3-2	846	2
W-T1t4-1, W-T1t4-2	846	4
W-T1t5-1, W-T1t5-2	846	10

Reference electrode

The reference cell used for the CPT measurements consisted of a standard calomel electrode (SCE) immersed in a saturated potassium chloride (KCl) solution. To get an electrochemical connection between the reference electrode and the electrolyte, a hose filled with electrolyte and secured with a cotton string, was placed between the two beakers.

Equation 3.3.1 gives the half reaction in the SCE [74]:



The standard potential of the SCE is approximately 241 mV_{SHE} at 25°C and all the potentials for the modified ASTM G48 test are given with respect to that value.[74]

3.3.2 Anodic cyclic potentiodynamic polarization curves

To obtain the parameters OCP, E_p , E_{RP} , and i_p , the anodic CPP curves were recorded according to the ASTM G61 standard[65]. The electrolyte used for this experiment was 34 g sodium chloride (NaCl) dissolved in 920 mL distilled water with a magnet stirrer at ambient temperature. This gave about 3.56 wt% NaCl. Anodic CPP curves were obtained using a conventional three-electrode array - the reference electrode, a test samples as working electrode, and a platinum mesh as counter electrode. The reference electrode was electrochemically connected to the electrolyte by a luggin probe with a ceramic wick, filled with electrolyte. To obtain the anodic CPP curves there were used a Gamry Interface 1000 potentiostat. Making sure of minimal dissolved oxygen (O_2) in the electrolyte, all openings where covered and the electrolyte was bubbled with nitrogen (N_2) gas for one hour before immersing the sample in the solution. While the electrolyte was bubbled, it was heated in a water bath to the selected temperature of 40°C, 60°C, or 80°C, as given in Table 3.3.4. Nitrogen purging was maintained for the duration of the anodic polarization. OCP was measured for one hour before recording of the anodic CPP curve. The polarization started at E_{corr} , and scanned in the more noble direction at a scan rate of 0.6 V/h, before it turned at a sat current value of 0.6 A[65].

The test setup is illustrated in Figure 3.3.3 and shown in Figure 3.3.4 where the different components are numbered and specified in Table 3.3.3. Specifications of the samples tested with this method and the conditions used to obtain anodic CPP curves are given in Table 3.3.4. Surface characterization prior to electrochemical measurements showed a later precipitation of secondary phases for the T1 isothermal heat treatment for UNS S39274 than for UNS S32750. Since no intermetallic phases was observed for UNS S39274 before after 4 minutes of aging, there was decided to record anodic CPP curves for samples aged at 1, 4, and 10 minutes instead of the previously planned 1, 1.5, and 2 minutes as for UNS S32750. The anodic CPP curves for the T1 conditions of UNS S32750 were recorded during the project work[73].

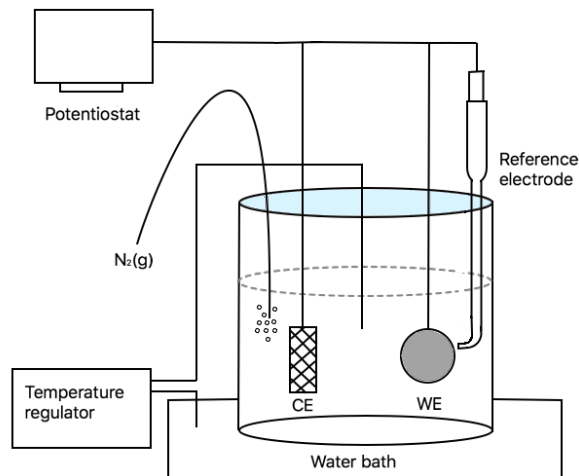
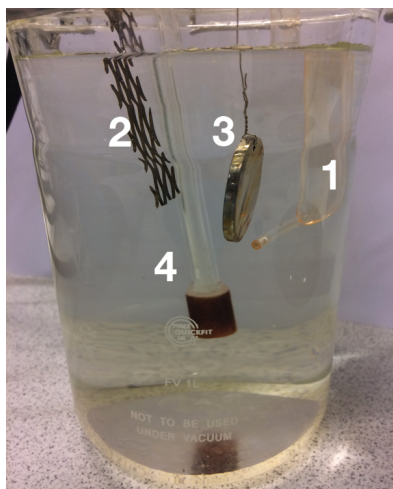
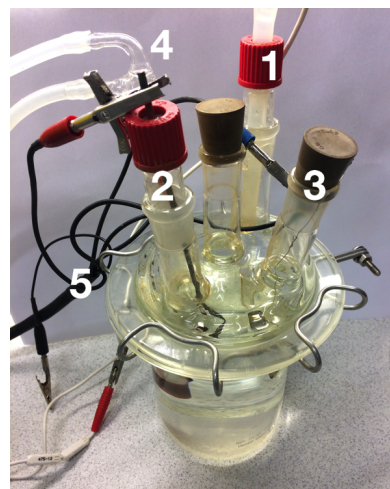


Figure 3.3.3: Illustration of the test setup for the ASTM G61 measurements used to obtain the anodic CPP curves, where CE is the counter electrode and WE is the working electrode.



(a) Closeup on the test setup, showing the different electrodes and the distances between them.



(b) An overview of the test setup without the water bath, showing the connections to the potentiostat.

Figure 3.3.4: An overview of the test setup, with numbered components, used to obtain the anodic CPP curves .

Table 3.3.3: Specifications of the numbered components in the test setup in Figure 3.3.4.

Number	Specification
1	Reference electrode
2	Counter electrode - platina mesh
3	Working electrode - test sample
4	Hose supplying N_2 (g)
5	Connection to the potentiostat

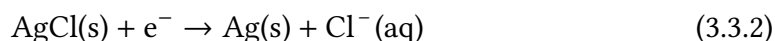
Table 3.3.4: Specifications of the samples and conditions used to obtain anodic CPP curves.

Sample name	Heat treatment temperature [°C]	Isothermal heating time [min]	Electrolyte temperature [°C]
AD-40-1, AD-40-2	-	-	40
AD-60-1, AD-60-2	-	-	60
AD-80-1, AD-80-2	-	-	80
SA-40-1, SA-40-2	-	-	40
SA-60-1, SA-60-2	-	-	60
SA-80-1, SA-80-2	-	-	80
T1t1-40-1, T1t1-40-2	846	1	40
T1t1-60-1, T1t1-60-2	846	1	60
T1t1-80-1, T1t1-80-2	846	1	80
T1t2-40-1, T1t2-40-2	846	1.5	40
T1t2-60-1, T1t2-60-2	846	1.5	60
T1t2-80-1, T1t2-80-2	846	1.5	80
T1t3-40-1, T1t3-40-2	846	2	40
T1t3-60-1, T1t3-60-2	846	2	60
T1t3-80-1, T1t3-80-2	846	2	80
T2t3-40-1, T2t3-40-2	790	4	40
T2t3-60-1, T2t3-60-2	790	4	60
T2t3-80-1, T2t3-80-2	790	4	80
T3t3-40-1, T3t3-40-2	920	4	40
T3t3-60-1, T3t3-60-2	920	4	60
T3t3-80-1, T3t3-80-2	920	4	80
W-AD-40-1, W-AD-40-2	-	-	40
W-AD-60-1, W-AD-60-2	-	-	60
W-AD-80-1, W-AD-80-2	-	-	80
W-SA-40-1, W-SA-40-2	-	-	40
W-SA-60-1, W-SA-60-2	-	-	60
W-SA-80-1, W-SA-80-2	-	-	80
W-T1t1-40-1, W-T1t1-40-2	846	1	40
W-T1t1-60-1, W-T1t1-60-2	846	1	60
W-T1t1-80-1, W-T1t1-80-2	846	1	80
W-T1t4-40-1, W-T1t4-40-2	846	4	40
W-T1t4-60-1, W-T1t4-60-2	846	4	60
W-T1t4-80-1, W-T1t4-80-2	846	4	80
W-T1t5-40-1, W-T1t5-40-2	846	10	40
W-T1t5-60-1, W-T1t5-60-2	846	10	60
W-T1t5-80-1, W-T1t5-80-2	846	10	80

Reference electrode

The reference electrode used for this method was a saturated Ag/AgCl electrode. It was electrochemically connected to the electrolyte by a luggin probe with a ceramic wick, filled with electrolyte, as illustrated in Figure 3.3.3.

Equation 3.3.2 gives the half reaction in the Ag/AgCl reference electrode[74]:



The standard potential for this reference electrode is approximately 199 mV_{SHE} at 25°C, and all the potentials for the ASTM G61 test are given with respect to that value.

3.4 Surface characterization

Microstructure characterization prior to electrochemical measurements was performed by another student in SEM using light optical microscopy (LOM), scanning electron microscope (SEM), backscattered electrons (BSE) in the SEM, and electron backscatter diffraction (EBSD). The surfaces of selected samples after electrochemical measurements were characterized by optical microscope (OM). All of the surface characterizations by OM were performed with a Alicona InfiniteFocus 3D optical microscope. A few selected sample were also characterized by SEM-BSE to see where the pitting initiated. The surface characterization in SEM were performed using a FEI Quanta FEG 650 Environmental SEM. The samples were rinsed with distilled water prior to surface characterization by OM, and rinsed in an ultrasonic bath with ethanol for 5 minutes prior to SEM.

Chapter 4

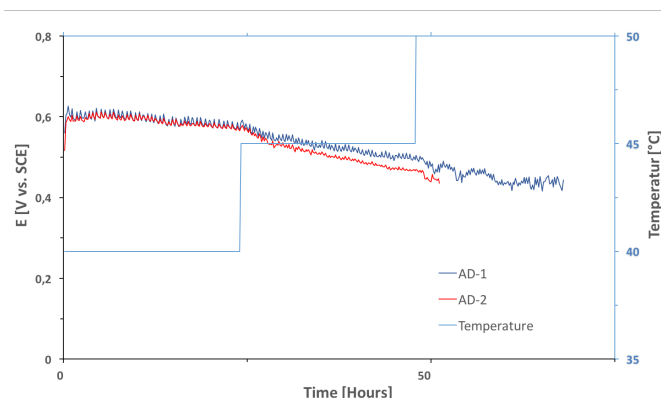
Results

This chapter presents the results from the experimental work on the SDSS grades UNS S32750 and UNS S39274. This was done according to the test matrixes given in Table 3.3.2 and 3.3.4. The electrochemical measurements are given in OCP curves and anodic CPP curves, where the OCP measurements were used to obtain CPT as a function of IHT and the anodic CPP curves were used to obtain E_p , E_{RP} , and i_p . Together with surface characterization by OM and SEM-BSE these results are used to describe the pitting corrosion properties of W-free UNS S32750 and W-rich UNS S39274 as a function of tungsten and isothermal heat treatments. To better understand the effect of tungsten and isothermal heat treatments, the results from this work are going to be compared with previously obtained results from two other students. One student performed the same electrochemical measurements as were performed in this work on low-W UNS S32760 containing 0.62 wt% W. Whereas the other student focused on microstructure characterizations on the three mentioned SDSS grades, W-free UNS S32750, low-W UNS S32760, and W-rich UNS S39274. The previously obtained work that are found most relevant are presented in Appendix B.3.

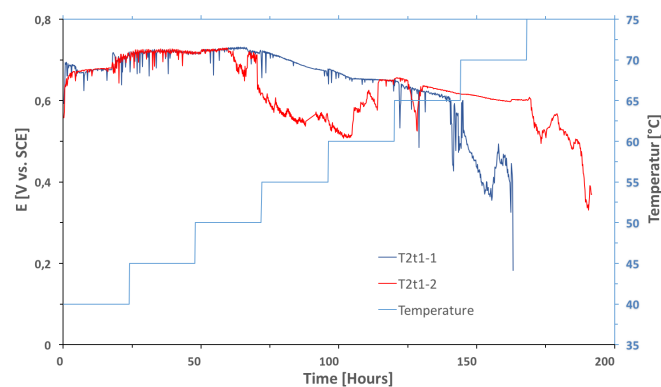
4.1 CPT measurements

To get a better understanding of the pitting corrosion resistance of the two grades, the conditions described in the test matrix in Table 3.3.2 was exposed in a 6% ferric chloride solution with increasing temperatures while OCP was measured, as described in Section 3.3.1. This gave CPT for the different conditions, which can be used to find a critical IHT, and to get an indication on the effect of alloying with tungsten. The results from this work are going to be compared with the results from UNS S32760 with 0.62 wt% tungsten, obtained by another student[75] and the T1 condition of UNS S32750,

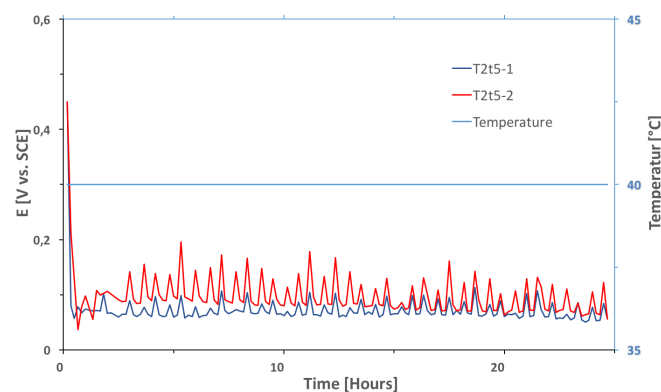
obtained in the project work[73], as can be found in Table B.3.4. To get a greater understanding of the results, they are going to be compared with surface characterizations prior to electrochemical measurements performed by another student[72]. This makes it possible to correlate the pitting corrosion resistance with the precipitation of intermetallic and secondary phases. Some of the results of the surface characterization prior to electrochemical measurements are included in Table 4.1.1 and can be found in Appendix B.3. Figure 4.1.1, 4.1.2, and 4.1.3 show some of the results of the CPT measurements, while the rest of the results are presented in Appendix B.2, and a summary of the results are given in Table 4.1.1 and 4.1.2. It was expected a steady decreasing CPT as a function of IHt.



(a) The CPT measurements of sample AD-1 and AD-2, UNS S32750 as-delivered samples that have not been solution annealed. Giving CPT of 45 and 40°C respectively.

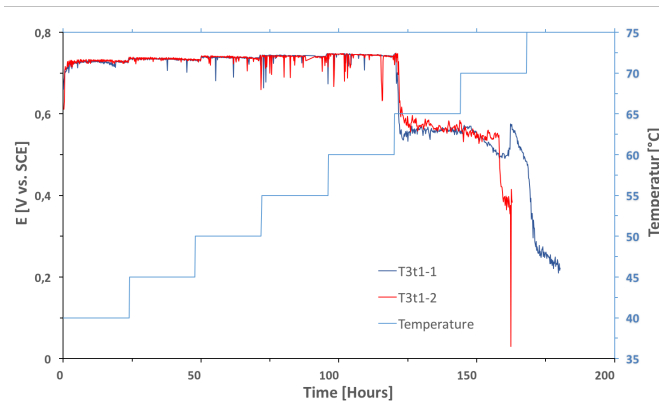


(b) The CPT measurements of sample T2t1-1 and T2t1-2, UNS S32750 samples isothermally heat treated for 1 minute at 790°C. Giving CPT of 70 and 75°C respectively.

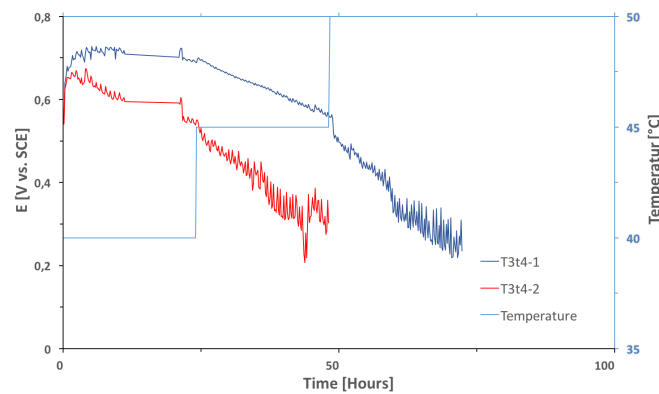


(c) The CPT measurements of sample T2t5-1 and T2t5-2, UNS S32750 samples isothermally heat treated for 20 minutes at 790°C. Giving CPT below 40°C.

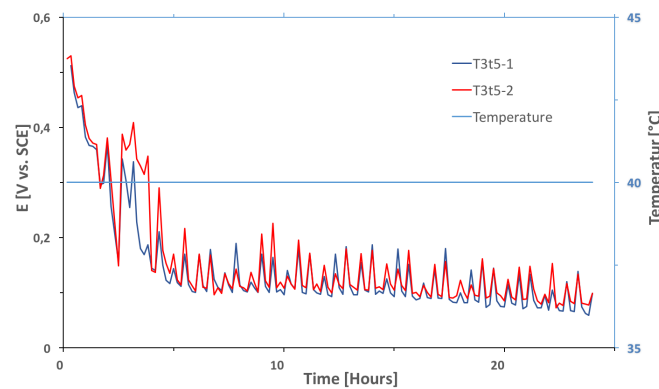
Figure 4.1.1: CPT measurements on UNS S32750 samples according to the modified version of G48.



(a) The CPT measurements of sample T3t1-1 and T3t1-2, UNS S32750 samples isothermally heat treated for 1 minute at 920°C. Giving CPT of 75 and 70°C respectively.

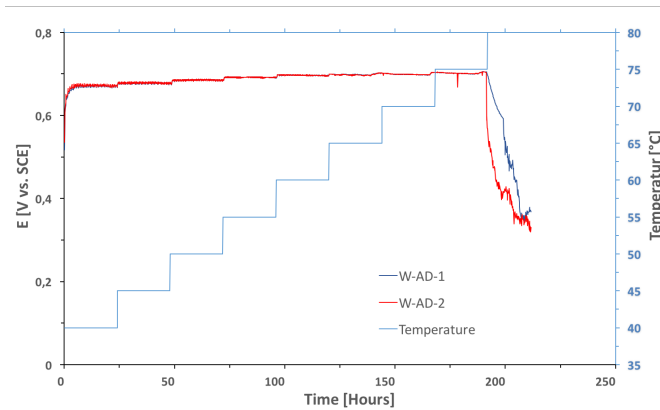


(b) The CPT measurements of sample T3t4-1 and T3t4-2, UNS S32750 samples isothermally heat treated for 10 minutes at 920°C. Giving CPT of 50 and 45°C respectively.

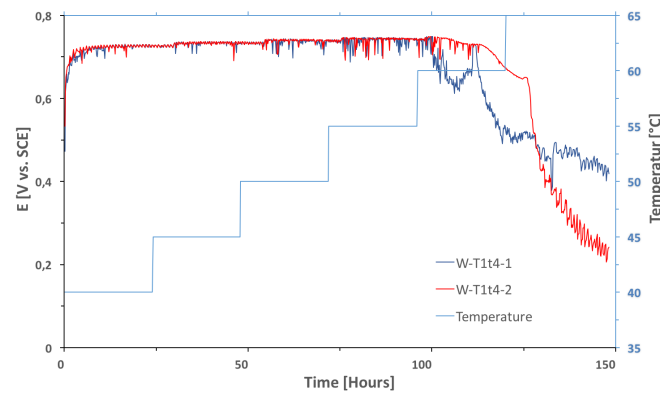


(c) The CPT measurements of sample T3t5-1 and T3t5-2, UNS S32750 samples isothermally heat treated for 20 minutes at 920°C. Giving CPT below 40°C.

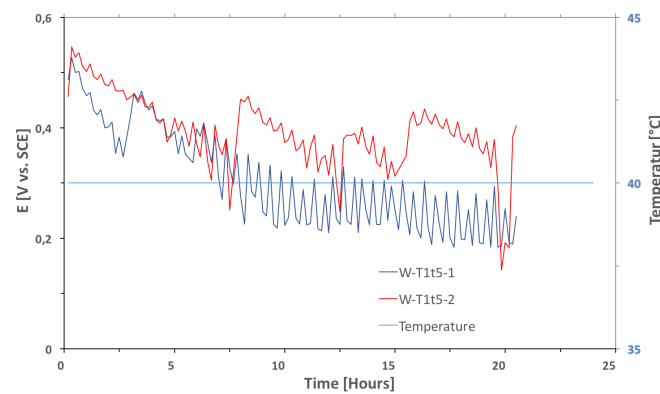
Figure 4.1.2: CPT measurements on UNS S32750 samples according to the modified version of G48.



(a) The CPT measurements of sample W-AD-1 and W-AD-2, UNS S39274 as-delivered samples that have not been solution annealed. Giving CPT of 80°C.



(b) The CPT measurements of sample W-T1t4-1 and W-T1t4-2, UNS S39274 samples isothermally heat treated for 4 minutes at 846°C. Giving CPT of 65°C.



(c) The CPT measurements of sample W-T1t5-1 and W-T1t5-2, UNS S39274 samples isothermally heat treated for 10 minutes at 846°C. Giving CPT below 40°C.

Figure 4.1.3: CPT measurements on UNS S32750 samples according to the modified version of G48.

As described in Section 3.3.1, when OCP is below 500 mV_{SCE}, SDSS is in the active area, which indicates that pitting has occurred. The as-delivered condition for UNS S32750 in Figure 4.1.1a show a slowly decreasing OCP from about 600 mV_{SCE}, where AD-1 reaches 500 mV_{SCE}, and thus CPT, at 45°C and AD-2 at 40°C. For the samples aged for 1 minute at 790°C shown in Figure 4.1.1b, T2t1-1 show a rapid decrease in OCP from about 700 mV_{SCE} to below 500 mV_{SCE} at 70°C, while T2t1-2 show a decreasing OCP almost down to 500 mV_{SCE} at 60°C, before it increases again. When the temperature had reached 75°C, a rapid decrease to below 500 mV_{SCE} could be observed. As can be observed in Figure 4.1.1c, both of the samples aged for 20 minutes at 790°C, show an immediate decrease in OCP to about 100 mV_{SCE}, giving CPT below 40°C.

Aging at 920°C for 1 minute gave a CPT between 70 and 75°C, as can be seen in Figure 4.1.2a. The two OCP curves show a stable value of about 700 mV_{SCE}, before they decreases rapidly to just above 500 mV_{SCE} at 65°C and keeps that potential until T3t1-1 decreases rapidly at 75°C and T3t1-2 at 70°C. With a holding time of 10 minutes, both curves show a steady decrease from just below 700 mV_{SCE}, as can be seen in Figure 4.1.2b. T3t4-2 reaches 500 mV_{SCE} first, giving a CPT of 45°C, while T3t4-1 gives a CPT of 50°C. After 20 minutes of aging, both of the samples give a CPT below 40°C, as can be seen from the immediate decrease in OCP in Figure 4.1.2c.

For the W-rich UNS S39274, the as-delivered condition in Figure 4.1.3a show a stable, slowly increasing OCP of approximately 700 mV_{SCE}, before both of the samples show a rapid decrease to below 500 mV_{SCE} at 80°C. When UNS S39274 is aged at 846°C for 4 minutes, both of the samples in Figure 4.1.3b show a stable and slowly increasing OCP of about 700 mV_{SCE}, before W-T1t4-1 start to decrease at 60°C and reaches 500 mV_{SCE} at 65°C. W-T1t4-2 decreases rapidly at 65°C. Figure 4.1.3c show that after 10 minutes of aging, both of the samples have a slowly decreasing OCP from just above 500 mV_{SCE}, giving CPT below 40°C.

As can be seen in Figure 4.1.1b, 4.1.2a, 4.1.3a, and 4.1.3b samples with high CPT had OCP measurements that showed a stable, slowly increasing potential at approximately 700 mV_{SCE} before a rapid potential decrease close to CPT. For samples with CPT just above 40°C, the potential was slowly decreasing from the beginning of the measurements. This can be observed in Figure 4.1.1a and 4.1.2b. For the measurements that gave CPT below 40°C, like in Figure 4.1.1c and 4.1.2c, they never reached 700 mV_{SCE} and showed a rapid potential decrease to about 100 mV_{SCE}.

CPT obtained from OCP measurements on UNS S32750 are given in Table 4.1.1. The results from the T1 conditions of UNS S32750 was obtained in the project work, but are included to show the whole picture[73]. To get a greater understanding of the affect of microstructure on corrosion resistance, the intermetallic phases detected during microstructure characterizations prior to corrosion testing are included in the table.

Table 4.1.1: CPT as a function of heat treatment. Where AD stands for as-delivered samples that have not been solution annealed and SA is the solution annealed condition where the samples only have been solution annealed and not isothermally heat treated.

Sample	IHT [°C]	IHt [min]	CPT [°C]	Secondary phases
AD-1	-	-	50	-
AD-2	-	-	45	-
SA-1	1110	15	80	-
SA-2	1110	15	80	-
T1t1-1	846	1	65	-
T1t1-2	846	1	65	-
T1t2-1	846	1.5	70	-
T1t2-2	846	1.5	75	-
T1t3-1	846	2	70	σ, χ
T1t3-2	846	2	70	σ, χ
T1t4-1	846	4	50	σ, χ
T1t4-2	846	4	50	σ, χ
T2t1-1	790	1	70	-
T2t1-2	790	1	75	-
T2t2-1	790	2	65	-
T2t2-2	790	2	75	-
T2t3-1	790	4	70	σ, χ
T2t3-2	790	4	70	σ, χ
T2t4-1	790	10	Below 40	σ, χ
T2t4-2	790	10	Below 40	σ, χ
T2t5-1	790	20	Below 40	σ, χ
T2t5-2	790	20	Below 40	σ, χ
T3t1-1	920	1	75	-
T3t1-2	920	1	70	-
T3t2-1	920	2	75	$\sigma, \text{Cr}_2\text{N}, \chi$
T3t2-2	920	2	70	$\sigma, \text{Cr}_2\text{N}, \chi$
T3t3-1	920	4	75	$\sigma, \text{Cr}_2\text{N}, \chi$
T3t3-2	920	4	70	$\sigma, \text{Cr}_2\text{N}, \chi$
T3t4-1	920	10	50	$\sigma, \text{Cr}_2\text{N}, \chi$
T3t4-2	920	10	45	$\sigma, \text{Cr}_2\text{N}, \chi$
T3t5-1	920	20	Below 40	$\sigma, \text{Cr}_2\text{N}, \chi, \gamma_2$
T3t5-2	920	20	Below 40	$\sigma, \text{Cr}_2\text{N}, \chi, \gamma_2$

CPT obtained from the electrochemical measurements on the SDSS grade UNS S39274 are listed in Table 4.1.2. The intermetallic precipitations and secondary phases detected during microstructure characterizations prior to corrosion testing are included in the table to get a greater understanding of the affect the microstructure has on the corrosion resistance.

Table 4.1.2: CPT as a function of heat treatment for UNS S39274. Where AD stands for as delivered samples that have not been solution annealed and SA is the solution annealed condition where the samples only have been solution annealed and not isothermal heat treated..

Sample	IHT [°C]	IHt [min]	CPT [°C]	Secondary phases
W-AD-1	-	-	80	-
W-AD-2	-	-	80	-
W-SA-1	1110	15	80	-
W-SA-2	1110	15	80	-
W-T1t1-1	846	1	80	-
W-T1t1-2	846	1	80	-
W-T1t2-1	846	1.5	80	-
W-T1t2-2	846	1.5	80	-
W-T1t3-1	846	2	75	-
W-T1t3-2	846	2	75	-
W-T1t4-1	846	4	65	σ, χ
W-T1t4-2	846	4	65	σ, χ
W-T1t5-1	846	10	Below 40	σ, χ
W-T1t5-2	846	10	Below 40	σ, χ

For the W-free UNS S32750 the results showed an increasing CPT as a function of IHT for T3 (920°C) and T2 (790°C) compared to T1 (846°C) performed in previous work. For the samples isothermally heat treated at T2 and T3, CPT as a function of IHt showed a similar trend, but with a slightly higher average CPT for T3. This is summarized in Figure 4.1.4.

The results of the CPT measurements showed a differens in CPT as a function of IHt between the two SDSS grades. The previously tested UNS S32750 samples from the T1 isothermal heat treatment, showed a more rapid decrease in CPT as a function of IHt than the W-rich UNS S39274. This is illustrated in Figure 4.1.5.

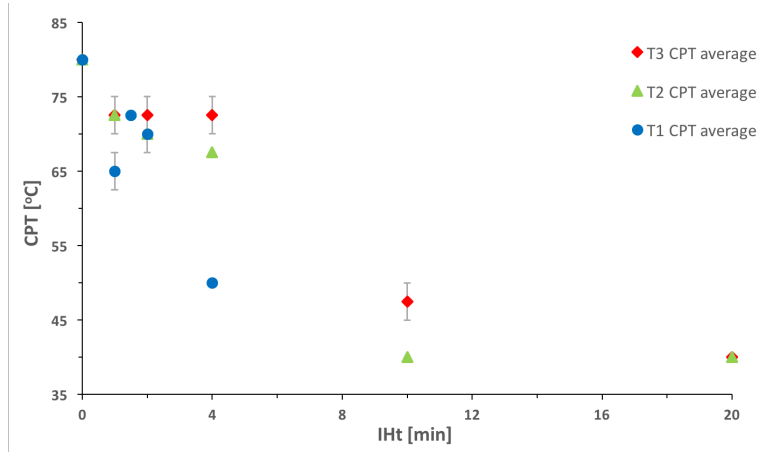


Figure 4.1.4: CPT as a function of IHT for all the UNS S32750 from the test matrix in Table 3.3.4.

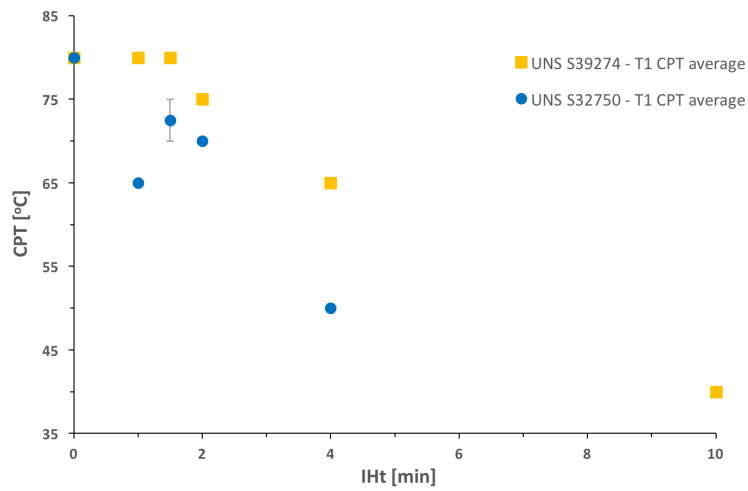


Figure 4.1.5: A comparison of the results from the CPT measurements of the T1 isothermal heat treatment on UNS S32750 and UNS S39274.

4.1.1 Surface characterization after electrochemical measurements

To get an overview of where pitting initiated and how severe the pitting was after the CPT measurements, the surfaces of the samples were characterized by OM, and the weight loss due to corrosion during the CPT measurements can be found in Appendix in Table B.1.1. Surface characterization by OM do not show which phase the pitting initiated or if it initiated along grain boundaries. Thus, some samples were characterized by SEM-BSE, to get a greater understanding to where the pits initiated.

Optical Microscopy

Several of the samples showed major weight loss after CPT measurements, as shown in Table B.1.1. The weight loss increased with increasing IHT and with increasing holding time after pit initiating. To be able to see how the CPT measurements affected the whole sample, a magnification of 2.5X was used. The results of the surface characterization by OM of W-free UNS S32750 can for selected samples be found in Figure 4.1.6 and 4.1.7, and for the W-rich UNS S39274 in Figure 4.1.8. The rest of the samples can be found in Appendix in Figure B.4.1 to B.4.3. To make it easier to compare the results, CPT is included. The dots and squares that can be observed in the figures after surface characterization by OM is due to a defect in the microscope, and do not need to be considered.

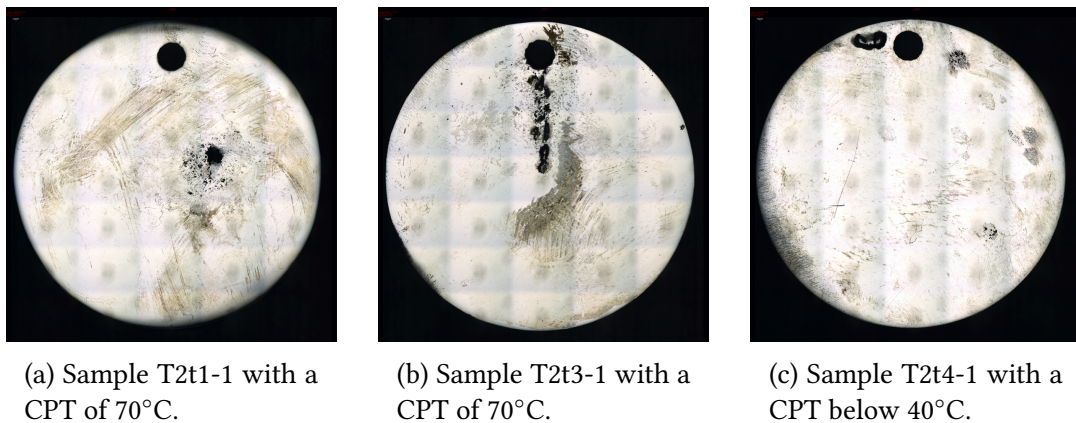
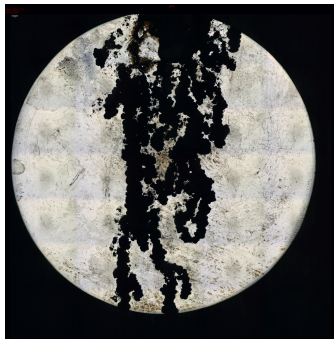
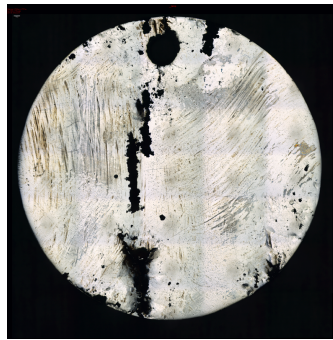


Figure 4.1.6: Surface characterization by OM with a magnification of 2.5X of selected W-free UNS S32750 samples heat treated at 790°C after the modified version of ASTM G48.

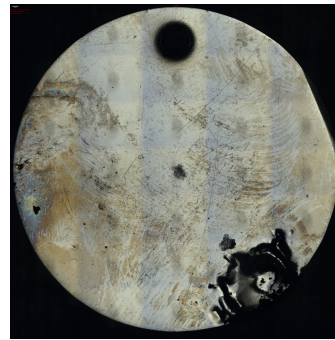
The W-free UNS S32750 show significant variations in amount of pitting after the CPT measurements. For the samples heat treated at 790°C, Figure 4.1.6a shows one relatively big pit in the middle of the sample after aging for 1 minute, while Figure 4.1.6b shows many pits between the hole and the middle of the samples. Both of the samples have CPT of 70°C. After aging for 10 minutes the CPT was measured to be below 40°C, and Figure 4.1.6c shows that one relatively big pit had occurred after the CPT measurements.



(a) Sample T3t1-1 with a CPT of 75°C.



(b) Sample T3t3-2 with a CPT of 70°C.



(c) Sample T3t4-1 with a CPT of 50°C.

Figure 4.1.7: Surface characterization by OM with a magnification of 2.5X of selected W-free UNS S32750 samples heat treated at 920°C after the modified version of ASTM G48.

After aging UNS S32750 at 920°C for 1 minute, Figure 4.1.7a shows that severe pitting had occurred across the sample from the hole and down, after CPT measurements. CPT was measured to be 75°C for that sample. Figure 4.1.7b show big pits both in the middle of the sample and on the edges. That samples had been aged for 4 minutes at 920°C and the CPT was measured to be 70°C. After aging for 10 minutes and CPT measurements, which gave a CPT of 50°C, the sample showed one big pit close to the edge.

The surface characterization by OM with a magnification of 2.5X of selected W-free UNS S32750 samples after CPT measurements can be found in Figure 4.1.8. The CPT is included making it easier to compare the results.

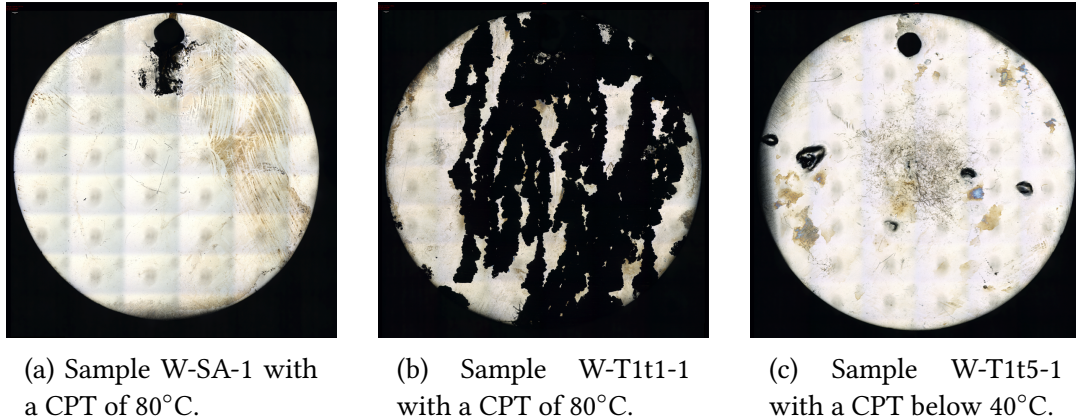


Figure 4.1.8: Surface characterization by OM with a magnification of 2.5X of selected W-rich UNS S39274 samples after the modified version of ASTM G48.

For the W-rich UNS S39274, the solution annealed condition in Figure 4.1.8a with a CPT of 80°C, show pitting around the hole after CPT measurements. After 1 minute of aging at 846°C, and still with a CPT of 80°C, Figure 4.1.8b shows that severe corrosion over the whole sample after CPT measurements. When the sample was aged for 10 minutes, CPT had dropped to below 40°C. Figure 4.1.8c shows that some relatively big pits had occurred at different places on the sample after CPT measurements.

Surface characterization by OM of W-free UNS S32750 and W-rich UNS S39274 show significant differences when the amount of pitting is evaluated and the samples with lower CPT shows generally less severe pitting than the ones with higher CPT. Individually differences can be seen from samples from the same condition and with the same CPT. The surface characterization by OM can mainly be used to show that pitting had initiated and not to establish the effect of tungsten and isothermal heat treatments.

To easier see the shape of the pits and the damage that was caused to the surrounding areas, some of the pits were more closely observed by OM with 2.5X magnification after the CPT measurements. It can be seen in Figure 4.1.7 that pitting had occurred at different places on the samples and that the pits had different shapes. Cracks can also be observed in Figure 4.1.9a and 4.1.9e. As can be seen from Figure 4.1.9a, 4.1.9b, 4.1.9c, and 4.1.9f, the size of the pits and the damage that was caused to the surrounding area differs significantly between the samples. Figure 4.1.9a shows a pit with surrounding cracks, Figure 4.1.9b show many connected pits, and Figure 4.1.9c shows one big pit

with surrounding smaller pits, while Figure 4.1.9f shows one smaller pit with remnants of a metal layer detached from the rest of the metal. While most of the samples showed corrosion in the middle of the sample, some of the samples had corroded on the edges and around the hole, as can be observed in Figure 4.1.9d and 4.1.9e.

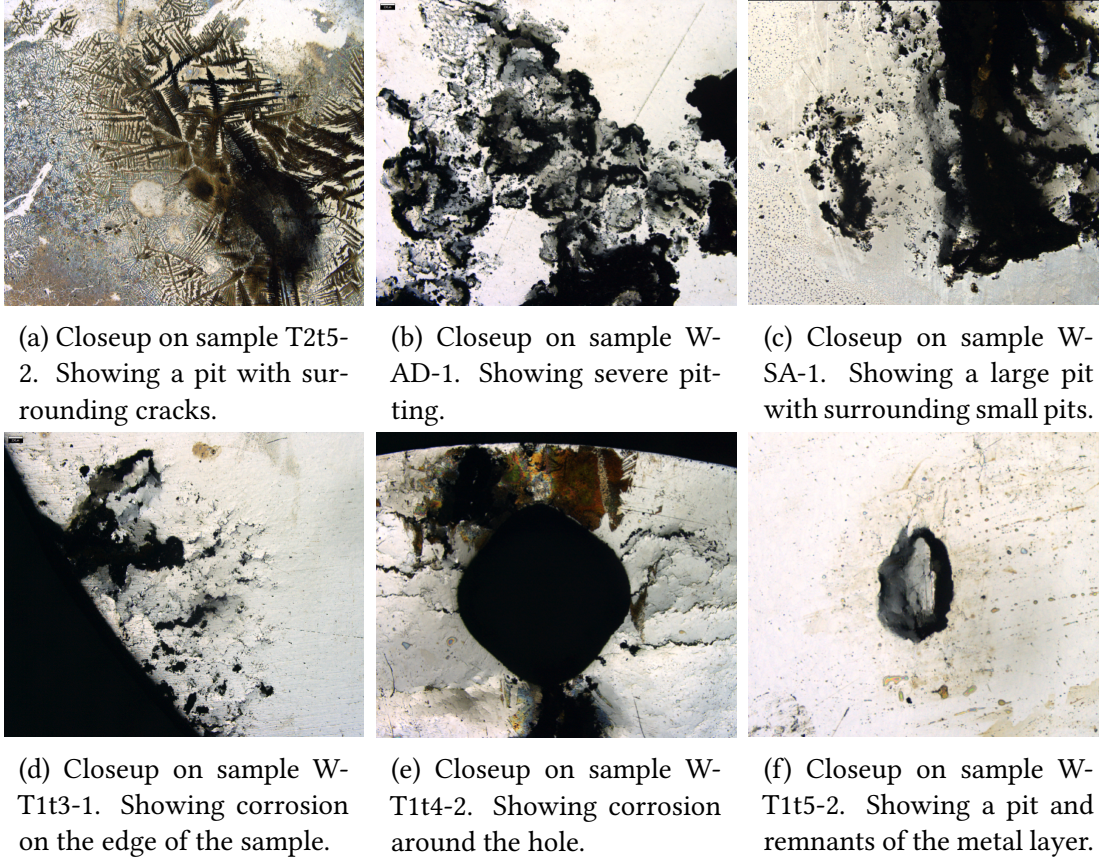
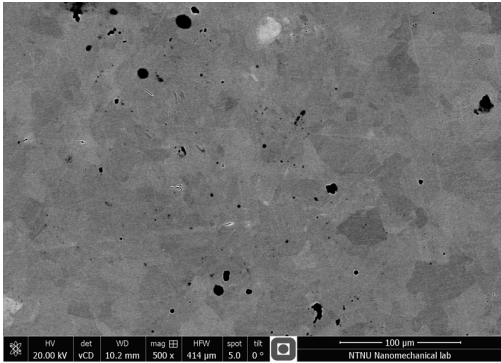


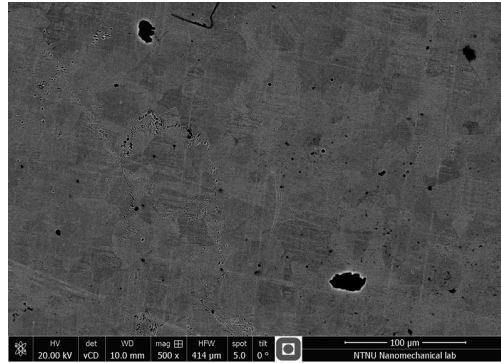
Figure 4.1.9: Closeup on the surface characterization by OM with a magnification of 2.5X of selected samples after the modified version of ASTM G48.

Scanning Electron Microscope

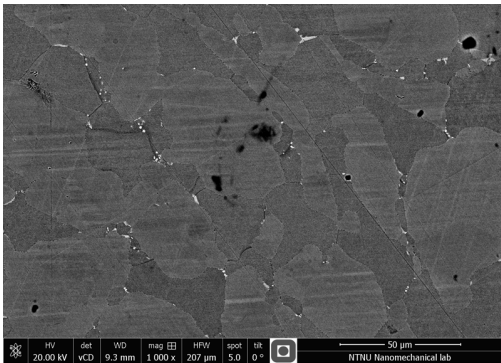
Selected samples from UNS S32750 and UNS S39274 with different heat treatments were also examined using the backscattered electron signal of SEM (SEM-BSE) as it is more sensitive than an optical microscope in detecting intermetallic phases. The SEM-BSE micrographs can be found in Figure 4.1.10 and 4.1.11. The objective with this was to establish if the pitting had occurred in the intermetallic phases, austenite, ferrite, or along the grain boundaries, and in what direction the pits grew. It was not possible to separate the secondary phases at the magnifications selected for these micrographs, but the phases that was present prior the electrochemical measurements was characterized by another student[72]. Some of the results from those measurements can be found in Appendix B.3 and are included in Table 4.1.1. They are also included when discussing the results from the electrochemical measurement, to help understand the effect of tungsten and the isothermal heat treatments. Intermetallic phases can be seen as bright inclusions due to the high content of molybdenum, which have a significantly larger atomic scattering factor than the other elements. The γ -phase appears slightly brighter than the α -phase.



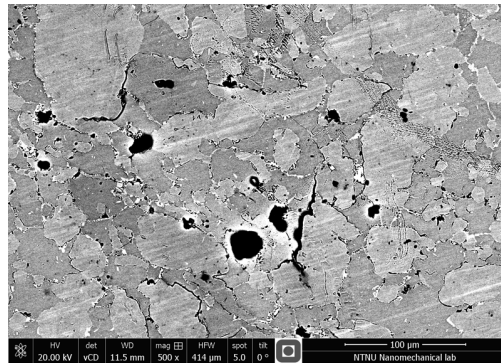
(a) Sample T1t1-1 with a magnification of 500X.



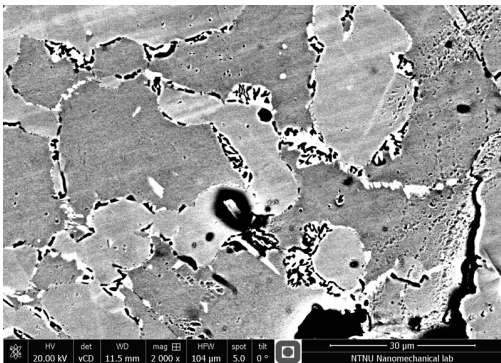
(b) Sample T1t3-1 with a magnification of 500X.



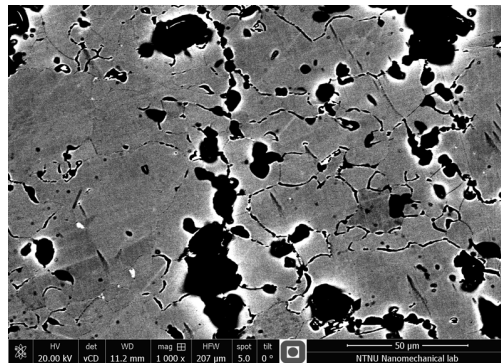
(c) Sample T1t4-1 with a magnification of 1000X.



(d) Sample T2t5-2 with a magnification of 500X.

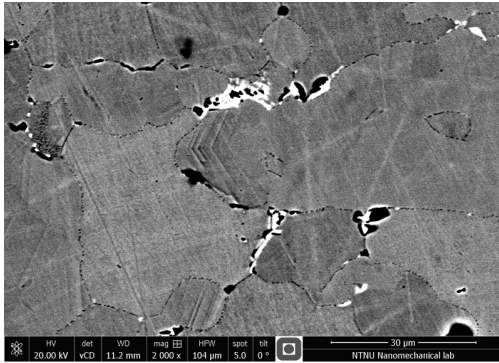


(e) Sample T2t5-2 with a magnification of 2000X.

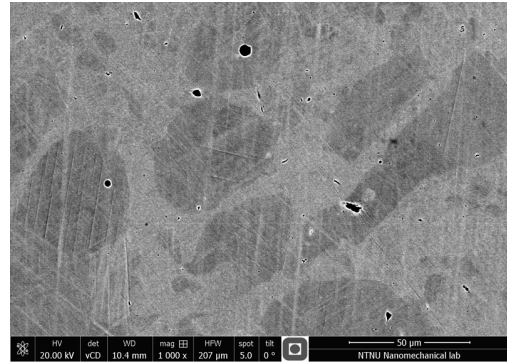


(f) Sample T3t3-2 with a magnification of 1000X.

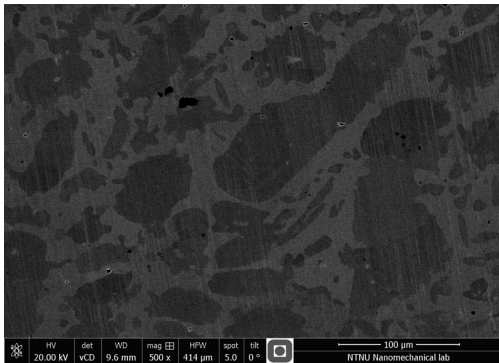
Figure 4.1.10: Surface characterization by back scattered SEM with different magnification of selected samples after the modified version of ASTM G48.



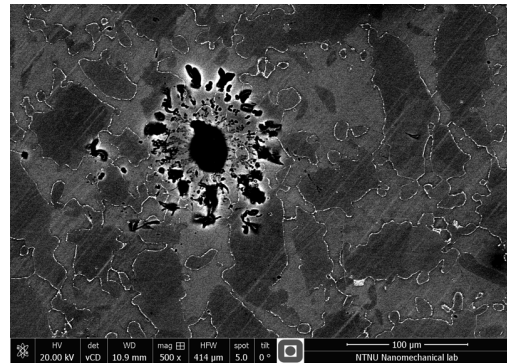
(a) Sample T3t3-2 with a magnification of 2000X.



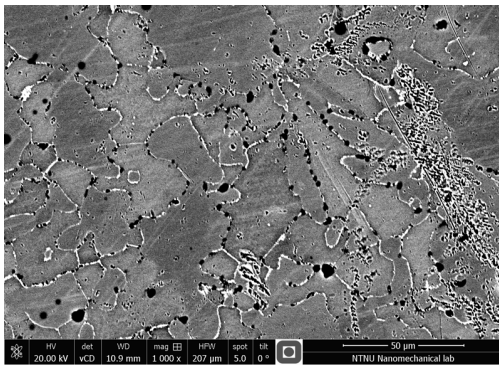
(b) Sample W-SA-1 with a magnification of 1000X.



(c) Sample W-T1t3-1 with a magnification of 500X.



(d) Sample W-T1t5-1 with a magnification of 500X.



(e) Sample W-T1t5-1 with a magnification of 1000X.

Figure 4.1.11: Surface characterization by back scattered SEM-BSE with different magnification of selected samples after the modified version of ASTM G48.

Trying to get a greater understanding of how addition of tungsten affects where pitting initiates, SEM-BSE micrographs of three different holding times at 846°C were taken for both W-free UNS S32750 and W-rich UNS S39274. For UNS S32750, holding times of 1, 2, and 4 minutes was chosen, given in Figure 4.1.10a, 4.1.10b, and 4.1.10c, respectively. A holding time of 1 and 2 minutes showed pitting mainly inside of γ -grains, but also in α -grains. After 3 minutes of aging, intermetallic phases had started to precipitate along the grain boundaries, and pitting was found to mainly initiate in the depleted areas around those inclusions. The solution annealed condition, together with aging for 2 and 10 minutes was chosen for UNS S39274. Their micrographs are found in Figure 4.1.11b and 4.1.11c, respectively. No secondary phases could be seen at the solution annealed condition or after 2 minutes of aging, and pitting was mainly observed inside the α -grains. As can be seen from Figure 4.1.11d and 4.1.11e, intermetallic phases along the grain boundaries could be observed after a holding time of 10 minutes. They show pitting to mainly initiate the depleted areas around the intermetallic phases, and some pits inside the α -grains.

To easier establish where the pitting initiates, a sample from a heating condition that measured a CPT below 40°C was investigated by SEM-BSE. This was because a low CPT indicates that intermetallic phases most likely have started to precipitate at larger quantities, as could be seen from surface characterizations prior to electrochemical measurements. Pitting corrosion have been found to mainly initiate at intermetallic phases, which also can be observed in Figure 4.1.10d and 4.1.10e. They show precipitation of intermetallic phases along the grain boundaries, and pitting mainly initiating in the depleted areas around those phases. Pitting can also be observed inside the grains, mainly γ . A condition where intermetallic phases were present at smaller quantities, as can be found in Table B.3.3, was also chosen to get an overview of where the pits mainly initiate at that condition. By observing Figure 4.1.10f and 4.1.11a, pitting are found to mainly initiate in the secondary phases along the grain boundaries.

4.2 Anodic cyclic potentiodynamic polarization curves

In this section, the anodic CPP curves obtained according to the ASTM G61 standard for samples given in the test matrix in Table 3.3.4 are presented. Values of the parameters OCP, E_p , E_{RP} , and i_p obtained from the anodic CPP curves are also given in this section. The anodic CPP measurements were performed to learn more about the pitting corrosion resistance to the different conditions as these test give a more detailed description of the pits than the CPT measurements. To see if the two measurements give the same results and to get a greater understanding of the results, the two electrochemical measurements are going to be compared. The anodic CPP measurements

forces pitting to initiate and the curves give an indication of the pit size. As described in Section 2.4.2, E_p is the potential where pitting initiates, giving an indication about the pitting corrosion resistance. E_{RP} is the repassivation potential of the pit, telling something about the depth of the pit, and the passive current density, i_p , is a measurement of the protectiveness of the passive film[66]. The hysteresis of the curve indicates if pitting corrosion is present or not[68, 69]. The OCP measurements prior to the recording of the anodic CPP curves performed in this thesis can be found in Appendix C.3.

Figure 4.2.1, 4.2.2, and 4.2.3 show some of the anodic CPP curves obtained with an electrolyte temperature of 40°C, while Figure 4.2.4, 4.2.5, and 4.2.6 show some of the anodic CPP curves obtained with an electrolyte temperature of 60°C, and Figure 4.2.7, 4.2.8, and 4.2.9 show some of the anodic CPP curves obtained with an electrolyte temperature of 80°C. The rest of the results are found in Appendix C.1.

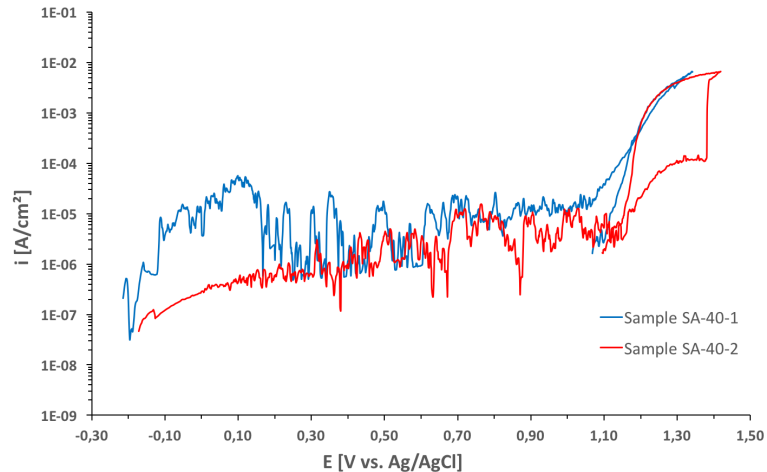


Figure 4.2.1: The anodic CPP curves for sample SA-40-1 and SA-40-2, UNS S32750 samples that only have been solution annealed and not isothermal heat treated. The curves were recorded with an electrolyte temperature of 40°C.

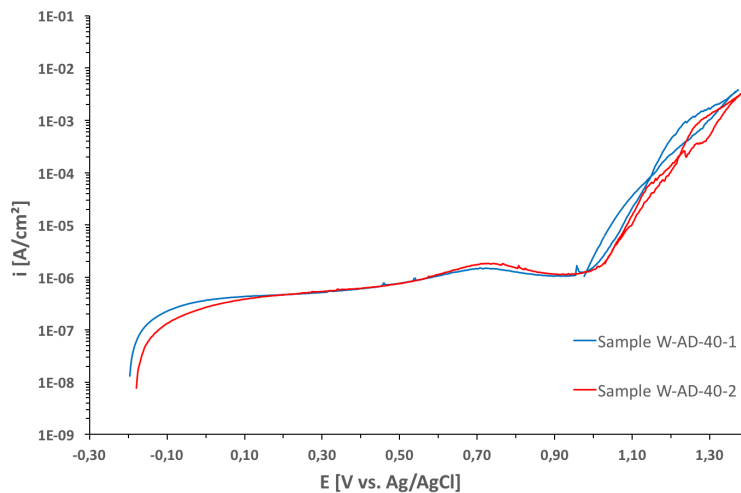


Figure 4.2.2: The anodic CPP curves for sample W-AD-40-1 and W-AD-40-2, UNS S39274 as delivered samples that have not been heat treated. The curves were recorded with an electrolyte temperature of 40°C.

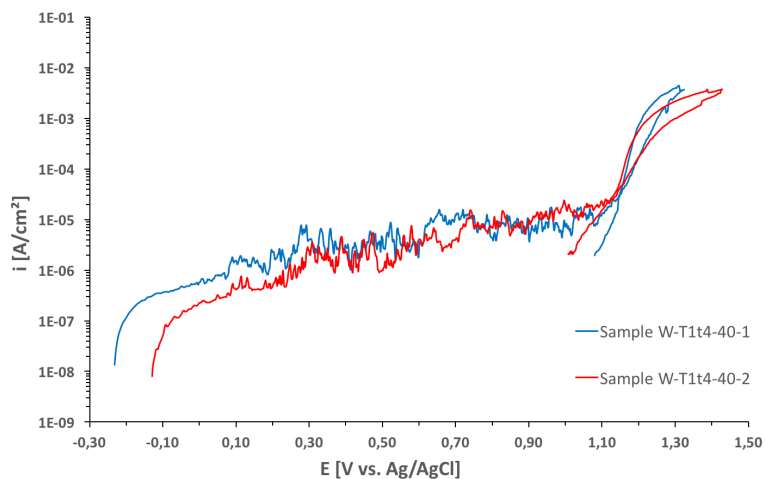


Figure 4.2.3: The anodic CPP curves for sample W-T1t4-40-1 and W-T1t4-40-2, UNS S39274 samples isothermal heat treated for 4 minute at 870°C. The curves were recorded with an electrolyte temperature of 40°C.

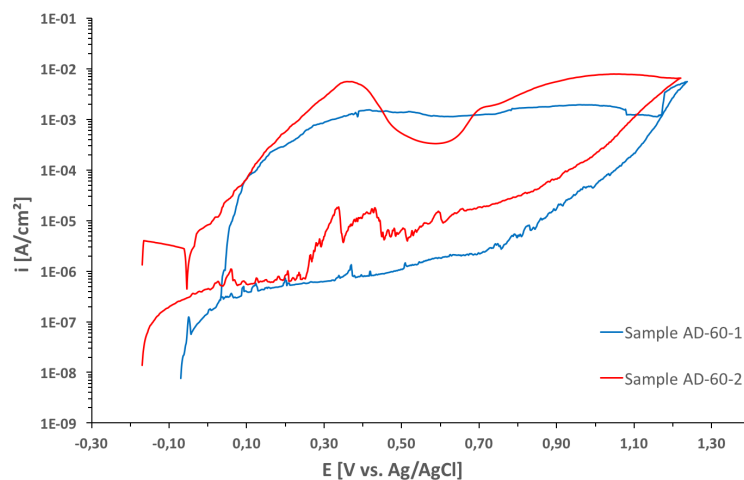


Figure 4.2.4: The anodic CPP curves for sample AD-60-1 and AD-60-2, UNS S32750 as delivered samples that have not been heat treated. The curves were recorded with an electrolyte temperature of 60°C.

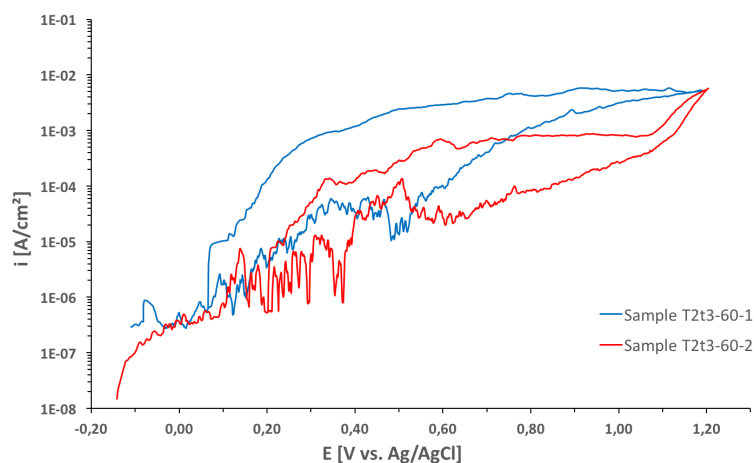


Figure 4.2.5: The anodic CPP curves for sample T2t3-60-1 and T2t3-60-2, UNS S32750 samples isothermal heat treated for 4 minutes at 810°C. The curves were recorded with an electrolyte temperature of 60°C.

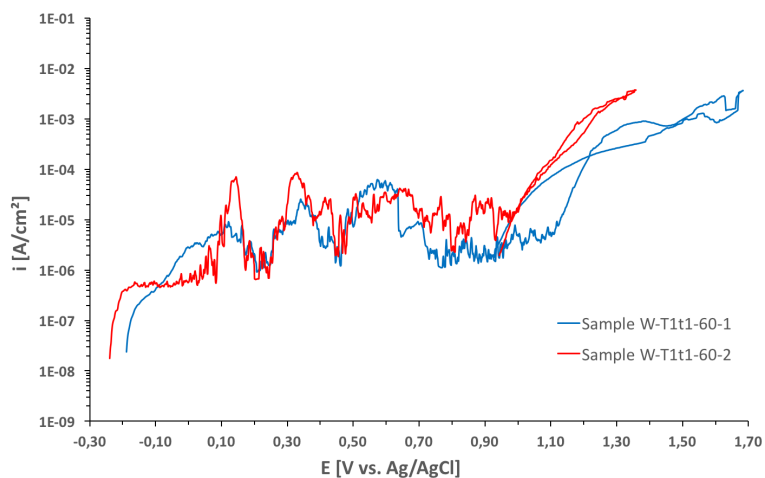


Figure 4.2.6: The anodic CPP curves for sample W-T1t1-60-1 and W-T1t1-60-2, UNS S39274 samples isothermal heat treated for 1 minute at 870°C. The curves were recorded with an electrolyte temperature of 60°C.

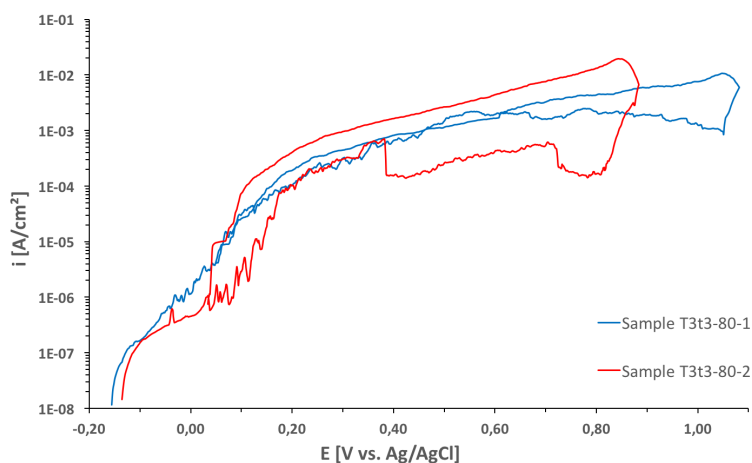


Figure 4.2.7: The anodic CPP curves for sample T3t3-80-1 and T3t3-80-2, UNS S32750 samples isothermal heat treated for 4 minutes at 920°C. The curves were recorded with an electrolyte temperature of 80°C.

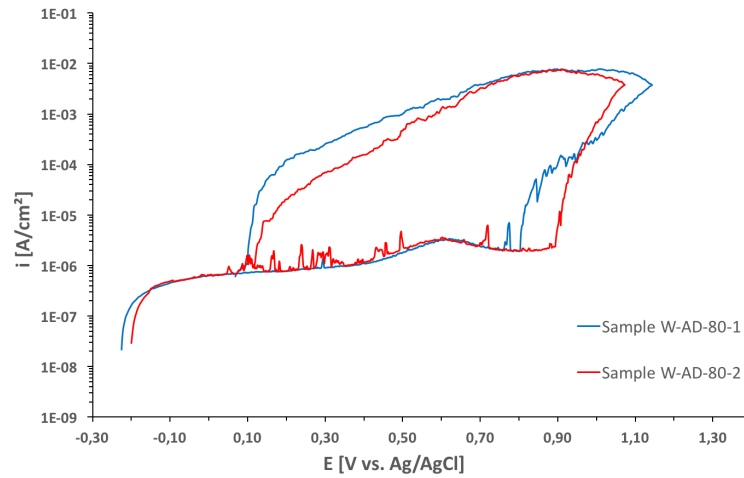


Figure 4.2.8: The anodic CPP curves for sample W-AD-80-1 and W-AD-80-2, UNS S39274 as delivered samples that have not been heat treated. The curves were recorded with an electrolyte temperature of 80°C.

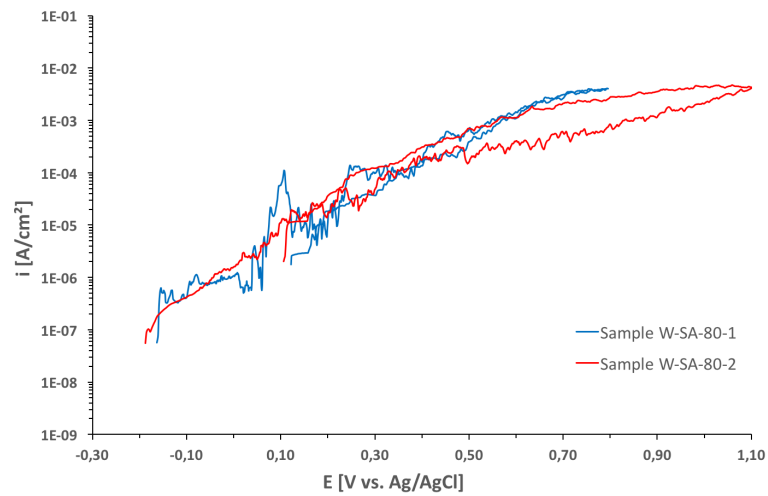


Figure 4.2.9: The anodic CPP curves for sample W-SA-80-1 and W-SA-80-2, UNS S39274 samples that only have been solution annealed and not isothermal heat treated. The curves were recorded with an electrolyte temperature of 80°C.

The polarization curves shows no hysteresis at 40°C, as can be seen in Figure 4.2.1, 4.2.2, and 4.2.3. At 60°C, Figure 4.2.4 show polarization curves with hysteresis, while the polarization curves in Figure 4.2.5 shows a smaller hysteresis, and the polarization curve in Figure 4.2.6 shows no hysteresis. Hysteresis loops could be observed for all of the polarization curves recorded at 80°C. Figure 4.2.7 shows a smaller hysteresis than Figure 4.2.8, but not as narrow as Figure 4.2.9.

The most interesting parameters obtained from the anodic CPP curves obtained at 40°C, 60°C, and 80°C for the test matrix in Table 3.3.4 are given in Table 4.2.1, 4.2.2, and 4.2.3 respectively. The results from the T1 isothermal heat treatments on UNS S32750 was obtain in the project work, but are included to get a greater understanding of the results[73].

Table 4.2.1: Parameters obtained by anodic CPP curves of samples according to Table 3.3.4 recorded with an electrolyte temperature of 40°C.

Sample	OCP [V _{Ag/AgCl}]	E _p [V _{Ag/AgCl}]	E _{RP} [V _{Ag/AgCl}]	i _p [μA/cm ²]
AD-40-1	-0.160	1.01		1.152
AD-40-2	-0.123	1.01		1.173
SA-40-1	-0.214	1.08	1.07	9.765
SA-40-2	-0.171	1.15	1.10	3.026
T1t1-40-1	-0.0568	1.03	0.990	0.6292
T1t1-40-2	-0.160	1.06	1.05	0.4496
T1t2-40-1	-0.202	0.997	0.977	0.083 71
T1t2-40-2	-0.144	0.995	0.969	1.266
T1t3-40-1	-0.0712	1.08	0.986	0.9595
T1t3-40-1	-0.191	1.07	1.03	3.894
T2t3-40-1	-0.237	1.08	1.02	6.272
T2t3-40-2	-0.103	0.987	0.995	1.015
T3t3-40-1	-0.309	1.14	1.04	10.34
T3t3-40-2	-0.0463	1.01	1.00	1.275
W-AD-40-1	-0.196	1.01	9.99	1.182
W-AD-40-2	-0.179	1.03	1.03	1.152
W-SA-40-1	-0.212	1.08	1.02	8.314
W-SA-40-2	-0.197	1.13	1.06	9.960
W-T1t1-40-1	-0.0982	0.998	1.12	1.272
W-T1t1-40-2	-0.194	1.06	1.08	1.751
W-T1t4-40-1	-0.231	1.10	1.09	8.333
W-T1t4-40-2	-0.129	1.12	1.01	10.41
W-T1t5-40-1	-0.208	0.993	0.902	7.639
W-T1t5-40-2	-0.132	1.14	1.04	5.936

Table 4.2.2: Parameters obtained by anodic CPP curves of samples according to Table 3.3.4 recorded with an electrolyte temperature of 60°C.

Sample	OCP [V_{Ag/AgCl}]	E_p [V_{Ag/AgCl}]	E_{RP} [V_{Ag/AgCl}]	i_p [μA/cm²]
AD-60-1	-0.0695	0.735	0.621	0.6537
AD-60-2	-0.170	0.253	0.266	0.6445
SA-60-1	-0.094	1.09		1.783
SA-60-2	-0.177	1.10		1.837
T1t1-60-1	-0.188	0.243	0.0790	2.268
T1t1-60-2	-0.192	0.363	0.0790	0.5654
T1t2-60-1	-0.168	1.03	0.681	0.7230
T1t2-60-2	-0.194	1.02	0.599	0.8250
T1t3-60-1	-0.238	1.00	0.597	9.220
T1t3-60-2	-0.157	1.01	0.867	0.8268
T2t3-60-1	-0.110	0.154	0.0656	1.340
T2t3-60-2	-0.141	0.377	0.202	1.276
T3t3-60-1	-0.442	0.0754	0.0704	1.263
T3t3-60-2	-0.178	0.0824	0.125	0.4970
W-AD-60-1	-0.155	1.03	1.07	1.538
W-AD-60-2	-0.197	1.03	0.985	1.396
W-SA-60-1	-0.185	0.991	0.904	9.007
W-SA-60-2	-0.472	1.09	1.04	9.765
W-T1t1-60-1	-0.188	1.11	0.930	2.707
W-T1t1-60-2	-0.240	0.980	0.943	3.612
W-T1t4-60-1	-0.175	0.414	0.308	7.966
W-T1t4-60-2	-0.203	0.249	0.0872	7.739
W-T1t5-60-1	-0.224	0.0594	0.00164	10.91
W-T1t5-60-2	-0.158	0.206	0.163	10.11

Table 4.2.3: Parameters obtained by anodic CPP curves of samples according to Table 3.3.4 recorded with an electrolyte temperature of 80°C.

Sample	OCP [$V_{Ag/AgCl}$]	E_p [$V_{Ag/AgCl}$]	E_{RP} [$V_{Ag/AgCl}$]	i_p [$\mu A/cm^2$]
AD-80-1	-0.188	0.280	-0.024	0.5240
AD-80-2	-0.0507	0.234	-0.012	0.5678
SA-80-1	-0.178	0.233	0.0718	1.242
SA-80-2	-0.106	0.155	0.0517	1.040
T1t1-80-1	-0.172	0.303	0.107	0.7448
T1t1-80-2	-0.148	0.360	0.0153	0.6574
T1t2-80-1	-0.186	0.413	0.0704	0.6264
T1t2-80-2	-0.180	0.257	0.0784	0.7556
T1t3-80-1	-0.223	0.514	0.0319	0.8997
T1t3-80-2	-0.148	0.185	0.0536	0.9324
T2t3-80-1	-0.138	0.0213	0.0038	1.731
T2t3-80-2	-0.225	0.118	0.0974	1.015
T3t3-80-1	-0.155	0.0997	0.0160	1.225
T3t3-80-2	-0.136	0.0758	0.0878	1.011
W-AD-80-1	-0.226	0.803	0.101	1.843
W-AD-80-2	-0.201	0.892	0.121	1.846
W-SA-80-1	-0.163	0.177	0.122	2.482
W-SA-80-2	-0.188	0.198	0.106	3.807
W-T1t1-80-1	-0.143	0.264		0.7164
W-T1t1-80-2	-0.172	0.185		1.085
W-T1t4-80-1	-0.118	0.111	0.000 440	3.448
W-T1t4-80-2	-0.240	0.230	0.005 91	24.31
W-T1t5-80-1	-0.176	0.0178	-0.0182	0.8314
W-T1t5-80-2	-0.272	-0.0158	-0.0288	5.833

Table 4.2.1 show that all of the anodic CPP curves obtained at 40°C have E_p around 1 $V_{Ag/AgCl}$ and a slightly lower value of E_{RP} . The pitting potential for samples tested with an electrolyte temperature of 60°C was found to have big variations in E_p between 0 and 1 $V_{Ag/AgCl}$, and the repassivation potential was found to be close to the pitting potential. This can be observed in Table 4.2.2. At 80°C the pitting was found to initiate at about 0.2 $V_{Ag/AgCl}$ for all of the samples except from W-AD-80-1, and to repassivate close to 0 $V_{Ag/AgCl}$. This can be found in Table 4.2.3. The same range of OCP was recorded at all of the electrolyte temperatures. For most of the samples it was found in the range of -0.150 to -0.250 $V_{Ag/AgCl}$. i_p was found to vary between 1 $\mu A/cm^2$ and 10 $\mu A/cm^2$ for all of the samples except from W-T1t4-80-2.

4.2.1 Surface characterization after electrochemical measurements

The surfaces of the samples after the anodic CPP measurements was characterized by OM to see how the measurements affected the samples. To be able to see how the CPT measurements affected the whole sample, a magnification of 2.5X was used. The surface characterization gives a correlation between the pitting measured to have initiated in the polarization curves and the pits that actually have appeared on the surface. The surface characterizations by OM after anodic CPP measurements with an electrolyte temperature of 40°C can be found in Figure 4.2.10, while Figure 4.2.11 and 4.2.12 show the samples after anodic CPP measurements with electrolyte temperatures of 60°C and 80°C, respectively. The rest rest of the surface characterizations can be found in Appendix in Figure C.2.1, C.2.2, and C.2.3.

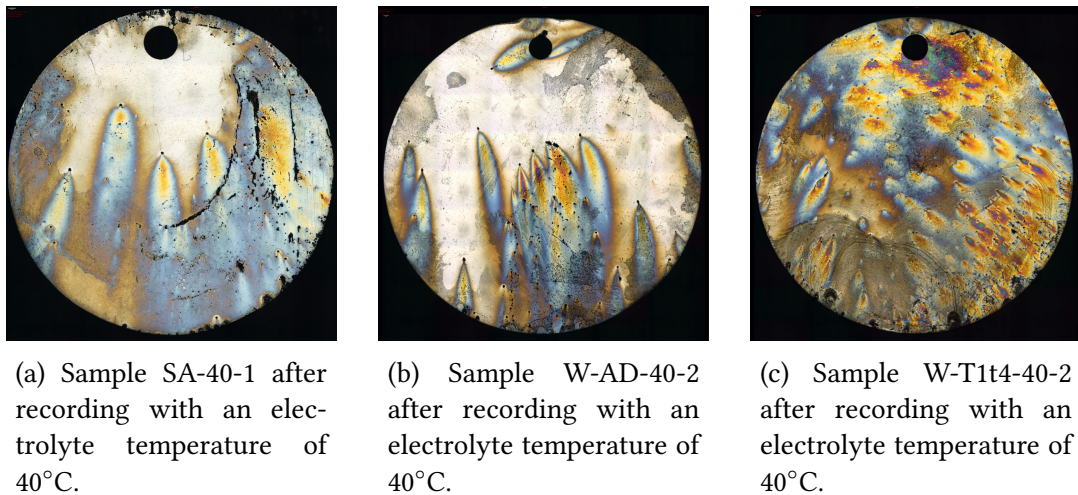
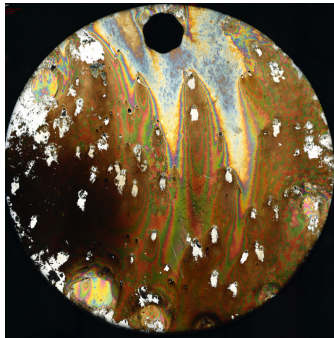
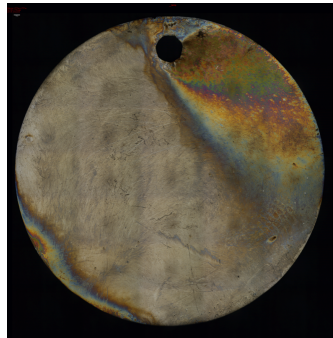


Figure 4.2.10: Surface characterization by OM with a magnification of 2.5X of selected samples after electrochemical measurements according to ASTM G61 with an electrolyte temperature of 40°C.



(a) Sample AD-60-2 after recording with an electrolyte temperature of 60°C.

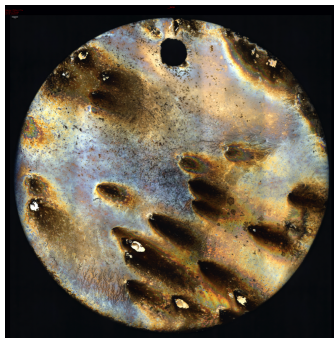


(b) Sample T2t3-60-1 after recording with an electrolyte temperature of 60°C.

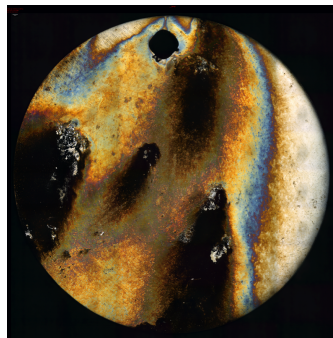


(c) Sample W-T1t1-60-1 after recording with an electrolyte temperature of 60°C.

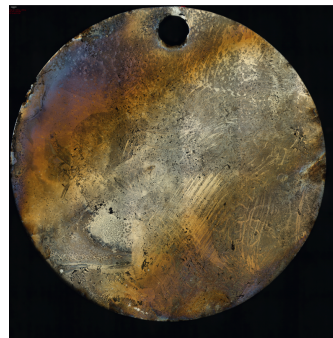
Figure 4.2.11: Surface characterization by OM with a magnification of 2.5X of selected samples after electrochemical measurements according to ASTM G61 with an electrolyte temperature of 60°C.



(a) Sample T3t3-80-2 after recording with an electrolyte temperature of 80°C



(b) Sample W-AD-80-1 after recording with an electrolyte temperature of 80°C.



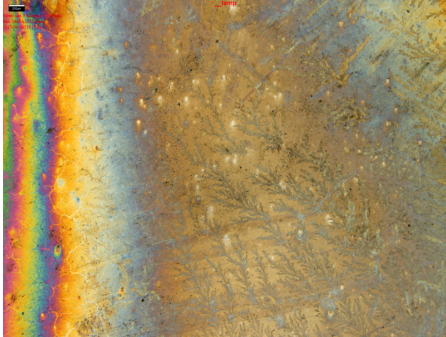
(c) Sample W-SA-80-1 after recording with an electrolyte temperature of 80°C.

Figure 4.2.12: Surface characterization by OM with a magnification of 2.5X of selected samples after electrochemical measurements according to ASTM G61 with an electrolyte temperature of 80°C.

Some of the samples after recording with an electrolyte temperature of 40°C, as given in Figure 4.2.10, show many small pits covering the whole surface, such as the sample in Figure 4.2.10c while others only have some small pits, as in Figure 4.2.10a and 4.2.10b. The surfaces after 60°C show big variations after the electrochemical measurements, as can be seen in Figure 4.2.11. It varies from almost no visible pitting, as in Figure 4.2.11b, to severe corrosion over the whole sample, as in Figure 4.2.11a, while Figure 4.2.11c shows pits evenly partitioned around the samples. By observing Figure 4.2.12, big variations in pit size and amount of pitting can be seen after recording the anodic CPP curves with an electrolyte temperature of 80°C. Many smaller pits can be observed in Figure 4.2.12a, while Figure 4.2.12b shows fewer bigger pits, whereas there are almost no signs of pitting in Figure 4.2.12c.

To get an overview of the different sizes of the pits and how the anodic CPP measurements affected the passive oxide film, closeups of selected samples by OM with a magnification of 2.5X are shown in Figure 4.2.13. There can be observed different sizes of the pits both at the same electrolyte temperature and at different electrolyte temperatures. The passive oxide film shows many different colors after the anodic CPP curves were obtained, and some small cracks forming in the oxide layer can also be observed.

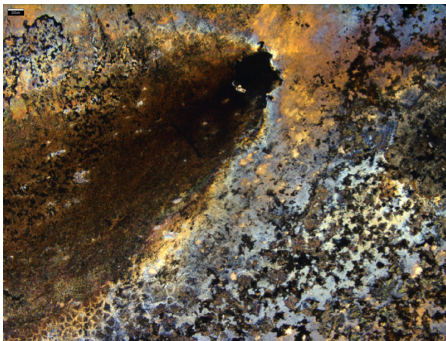
Different colors in the oxide film together with some small cracks can be observed both in Figure 4.2.13a and in Figure 4.2.13f. Figure 4.2.13b shows many small pits on the surface, while Figure 4.2.13e shows slightly bigger pits. One big pit with surrounding smaller pits can be observed in Figure 4.2.13c, whereas Figure 4.2.13d shows small pits and different colors in the oxide film.



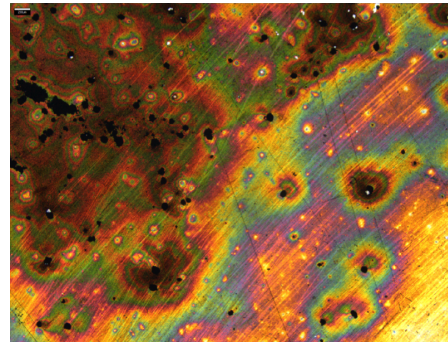
(a) Closeup on sample SA-60-2 - different colors and small cracks in the oxide film.



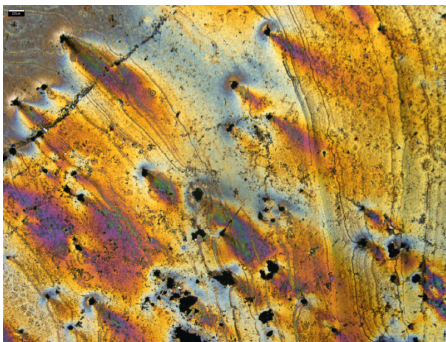
(b) Closeup on sample T2t3-40-2 - showing many small pits on the surface.



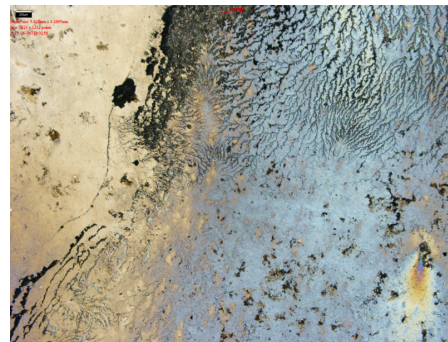
(c) Closeup on sample T2t3-80-2 - showing a big pit with surrounding smaller pits.



(d) Closeup on sample T3t3-60-1 - showing pitting and different colors at the oxide film.



(e) Closeup on sample W-T1t4-40-2 - showing small pits on the surface.



(f) Closeup on sample W-T1t5-80-2 - showing discoloration and cracks in the oxide.

Figure 4.2.13: Closeup on the surface characterization by OM with a magnification of 2.5X of selected samples after anodic CPP measurements.

Chapter 5

Discussion

The results of this work are compared to the parallel work done by two other students. One of the students focused on the corrosion resistance of UNS S32760, a SDSS grade containing 0.62 wt% W, and the other on microstructure characterizations prior to electrochemical measurements on UNS S32750, UNS S32760, and UNS S39274. All of the test samples were machined the same way and had the same surface finish as used in this work. The same electrochemical measurements were performed on all of the above mentioned SDSS grades. Selected results from the other students work are included in Appendix B.3.

5.1 Electrochemical measurements

CPT was obtained by OCP measurements while exposed to 6 wt% ferric chloride, as described in Section 3.3.1. The OCP of passive stainless steel was 700 mV_{SCE} in this electrolyte and most of the samples showed a stable passive behavior at that potential in the beginning of the measurement[71]. When CPT was reached, OCP dropped as seen in Figure 4.1.3a. The samples that had a lower CPT showed a more stable decreasing OCP, like in Figure 4.1.1a. This may be due to active corrosion. CPT has been arbitrarily defined as the temperature where the OCP drops below 500 mV_{SCE}, which can be explained based on polarization curves. Detrimental phases or increased temperature can decrease the pitting corrosion area or increase the active area in the polarization curve. The corrosion rate depends on the intersection between the cathodic tafel slope for dissolution of trivalent iron into divalent iron with the anodic polarization curve. This intersection gives a low corrosion rate if a stable oxide film is present. If detrimental phases are present or the temperature is raised and there is damage in the oxide film, the intersection can be found in the pitting area or in the ac-

tive area of the anodic polarization curve, which gives a high corrosion rate. This will also suppress the OCP from the corrosion potential of iron to lower values, and the critical value for activation and corrosion has been found to be about 500 mV_{SCE} [71]. The results of the CPT measurements performed in this work can be found in Section 3.3.1 and B.2, and a summary of the results from all of the grades mentioned in this thesis can be found in Table B.3.4. Some of the results from microstructure characterizations prior to electrochemical measurements are given in Appendix B.3.

The anodic CPP curves in this thesis were obtained at three different electrolyte temperatures, 40°C , 60°C , and 80°C , as described in Section 3.3.2. Figure 4.2.1, 4.2.2, and 4.2.3, together with Figure C.1.1 to C.1.6 in Appendix, show that all of the samples tested with an electrolyte temperature of 40°C , had anodic CPP curves with no or little hysteresis. This indicates no pitting corrosion or small pits respectively, but anodic dissolution and oxygen evolution[64, 67]. For anodic CPP curves recorded with an electrolyte temperature of 60°C , most of the curves showed no or little hysteresis, but some of them had a hysteresis, indicating pitting corrosion. This can be observed in Figure 4.2.4, 4.2.5, and 4.2.6, together with Figure C.1.7 to C.1.12 in Appendix. All of the anodic CPP curves obtained at 80°C have a hysteresis, as can be seen in Figure 4.2.7, 4.2.8, and 4.2.9, together with Figure C.1.13 to C.1.18 in Appendix. The same was observed at anodic CPP measurements of UNS S32760[75].

5.2 General trends

Prior to recording of the anodic CPP curve, OCP was measured for one hour. The average OCP of UNS S32750 at 40°C , 60°C , and 80°C was measured to be $-156 \text{ mV}_{Ag/AgCl}$, $-180 \text{ mV}_{Ag/AgCl}$ and $-160 \text{ mV}_{Ag/AgCl}$, respectively as given in Table 4.2.1, 4.2.2, and 4.2.3. For UNS S39274, the average OCP of UNS S32750 at 40°C , 60°C , and 80°C was measured to be $-178 \text{ mV}_{Ag/AgCl}$, $-218 \text{ mV}_{Ag/AgCl}$ and $-190 \text{ mV}_{Ag/AgCl}$, respectively. This indicates a similar value of OCP for the different electrolyte temperatures. To secure a minimum concentration of dissolved oxygen, the electrolyte was bubbled with nitrogen gas for one hour before the OCP measurements, but a high value of OCP may indicate that there are some oxygen present. If dissolved oxygen are present it may cause formation of oxides on the metal surface[45]. Due to degradation of the oxide film at increased temperature, the OCP is expected to be lower at higher temperatures. There was found no general trend between samples with same IHt, but different electrolyte temperature. Significant individual differences are observed for almost all of the measurements, as can be seen in Table 4.2.1 for T3t3-40-1 and T3t3-40-2 that have OCP of $-71 \text{ mV}_{Ag/AgCl}$ and $-191 \text{ mV}_{Ag/AgCl}$ respectively. This indicates that there may still be some dissolved oxygen present in the electrolyte. Another factor that can affect the measurements

was bubbles in the luggin probe, disturbing the connection to the reference electrode, especially at high temperatures. This problem was noticed and avoided in almost every case. Comparing the values of OCP obtained at this thesis with the results obtained from UNS S32760 with 0.62 wt% and the same sample preparations[75]. The average OCP of UNS S32760 at 40°C, 60°C, and 80°C was measured to be mV_{SCE} , $-119 mV_{SCE}$, and $-203 mV_{SCE}$, respectively. These results show the temperature effect on OCP, but the OCP obtained at lower electrolyte temperatures are higher than expected, indicating presence of dissolved oxygen. The SCE reference electrode has a potential of 0.042 V, with respect to the standard hydrogen electrode, higher than the Ag/AgCl reference electrode at 25°C[74]. This is almost negligible for this work. The value of the OCP does not seem to affect the results noticeably, as for SA-60-1 and SA-60-2 in Table 4.2.2. Even though there is a difference in the OCP for samples from the same condition, the pitting and repassivation potential are still approximately the same. This can also be seen in the anodic CPP curve in Figure 4.2.3, showing that the curves follow each other even though they started at different potentials.

A clear correlation between E_p and the hysteresis size of the anodic CPP curves was found. E_p is the potential where pitting initiates, which gives an indication of the pitting resistance at the given electrolyte temperature. Whether or not the polarization curve have a hysteresis, reveals if the pits repassivates immediately after initiating or if the pits continue to grow before they repassivates. Thus, how big the pits are. The samples that have anodic CPP curves with no or little hysteresis have a value of E_p close to or above $1.0 V_{Ag/AgCl}$. This is in accordance with literature where E_p has been found to be $1.0 V_{SCE}$ for DSS and SDSS[13]. The SCE reference electrode has a potential of 0.042 V, with respect to the standard hydrogen electrode, higher than the Ag/AgCl reference electrode at 25°C[74]. The anodic CPP curves with hysteresis have an average E_p of approximately $0.3 V_{Ag/AgCl}$. This shows that E_p drops several hundred mV when pitting corrosion is present, which is in accordance with literature[64, 67]. A reason for the E_p drop may be that an increasing temperature makes the protective oxide film less stable, which increases the possibilities for damage in the oxide film and thereby lead to pitting corrosion as described in Section 2.4[57]. E_p is known to reduce with increasing amount of intermetallic phases[57]. This is because the passive film weakens by the formation of intermetallic phases, thus decreasing the pitting corrosion resistance. There was not observed any difference in the behavior of E_p between the W-free UNS S32750 and the W-rich UNS S39274, and by comparing the values of E_p obtained at this thesis with the results previously obtained with low-W UNS S32760. All of the anodic CPP curves obtained at 80°C together with the anodic CPP curves recorded at 60°C for UNS S32750 heat treated for 1 minute and UNS S39274 heat treated for 10 minutes, have a hysteresis. All of the anodic CPP curves show a value of E_p between 0 and $0.4 V_{Ag/AgCl}$. The rest of the anodic CPP curves recorded at 60 V°C and the ones recorded at 40 °C, have no hysteresis and an average value of E_p between 0.9

and $1.1 V_{Ag/AgCl}$.

All of the E_{RP} values for the anodic CPP curves obtained at 40°C were stable around $1.0 V_{Ag/AgCl}$, but slightly lower than the E_p values, as shown in Table 4.2.1. Pits only stop growing if the potential is lower than E_{RP} and since the repassivating potential varies with the depth of the pit, deeper pits have a lower E_{RP} [63]. This indicates that the pitting corrosion terminates at a high rate at this electrolyte temperature, immediately after the initiating of the pitting. The same can be seen at 60°C in Table 4.2.2 for the heat treatments that have a CPT of 80°C . For the other conditions at 60°C and for all of the conditions at 80°C , the E_{RP} value drops several hundred mV from the E_p value, as can be seen in Table 4.2.2 and 4.2.3. Indicating that it takes longer time from pit initiation till the termination of the pit. There was found no general trend for the values of i_p , which is a measure of the protectiveness of the oxide film[66]. For almost all the samples the value of i_p varied between $1 A/\mu\text{m}^2$ and $10A/\mu\text{m}^2$.

Table 4.1.1 and 4.1.2 show the results from the CPT measurements. It can be observed that all of the samples had a CPT below 80°C . This indicates that all of the anodic CPP curves obtained at 80°C should have a hysteresis, which is also the case. All of the samples that were used to record the anodic CPP curves, except from the as-delivered condition of UNS S39275 and after aging at 846°C for 10 minutes, had a CPT above 40°C , indicating no hysteresis for all of the samples except from those two. At 60°C , it can be observed from Table 4.1.1 and 4.1.2 that the samples with CPT below 60°C had anodic CPP curves with a hysteresis, whereas the samples with CPT above 60°C had anodic CPP curves without a hysteresis. The same correlations can be seen between CPT and the value of E_p , since E_p correlates with the size of the hysteresis.

5.3 Effect of tungsten and isothermal heat treatments

By comparing the electrochemical measurements with the microstructure characterizations prior to electrochemical measurements, it is possible to get a greater understanding of how tungsten and isothermal heat treatments affect the corrosion resistance properties of SDSS.

5.3.1 Solution annealed condition

W-free UNS S32750 and W-rich UNS S39274 had CPT of 80°C in the solution annealed condition, while UNS S32760 had a CPT of $75\text{-}80^\circ\text{C}$, indicating no intermetallic precipitation or secondary phases. This was verified by SEM-BSE and OM for UNS S32750

and 32760, and phase map and IQ-maps for UNS S39274, where no inclusions or intermetallic phases were found prior to corrosion testing[72], which is listed in Table B.3.3. The high CPT of the solution annealed conditions are reflected in the anodic CPP curves. There are not observed any hysteresis for the anodic CPP curves obtained with an electrolyte temperature of 40°C and 60°C for any of the solution annealed conditions of the examined SDSS grades. At 80°C, all of the anodic CPP curves for the solution annealed conditions have hysteresis, indicating pitting. The hysteresis are relatively narrow, which may indicate small pits.

5.3.2 As-delivered condition

For the as-delivered condition, UNS S39274 exhibited a CPT of 80°C, the same that was measured for the solution annealed condition. Whereas the CPT was significantly lower for the as-delivered condition for UNS S32750, which was measured to be between 45-50°C. As can be found in Table B.3.1, microstructure characterization prior to the electrochemical measurement found the α/γ -phase distribution to be 58.5/41.4 and 42.0/58.0 for the as-delivered conditions for UNS S32750 and UNS S39274, respectively. For the solution annealed condition they measured 57.2/42.8 and 47.6/52.4. Showing that the phase distribution was almost the same for the as-delivered and solution annealed condition for UNS S32750, indicating that it is not as a result of uneven phase distribution. However, it might be due to deleterious phases or also an improper balance of chemical composition in ferrite and austenite. As listed in Table B.3.2, there are no significant differences between the chemical composition before and after solution annealing of UNS S32750. But the solution annealed condition had a slightly more balanced chemical composition for ferrite and austenite than the as-delivered condition. However, the differences are not to that extent that they can explain the significantly lower CPT for the as-delivered condition for UNS S32750. Microstructural factors as grain orientation and grain size can also affect the corrosion properties of SDSS. The grains in the as-delivered condition for UNS S32750 was found to be elongated compared to the solution annealed grains, which was smaller and more equiaxed[72]. The as-delivered condition was not tested for UNS S32760.

The low CPT value of the as-delivered condition for UNS S32750 is also reflected in the anodic CPP curves, as can be seen in Figure C.1.1, 4.2.4, and C.1.13 obtained at 40°C, 60°C, and 80°C, respectively. The ones recorded with an electrolyte temperature of 40°C and 60°C do not seem to repassivate and they have hysteresis of significant sizes, indicating large pits that do not repassivate. This can be due to bad pre-aging of the material from the manufacturers, which have not repaired errors from the fabrication. For UNS S39274, no hysteresis are observed until recording with an electrolyte temperature of 80°C, which is in accordance with the CPT measurements.

The anodic CPP curves obtained for the as-delivered samples is less noisy than for the other conditions, as can be seen by comparing the anodic CPP curves in Figure 4.2.2 and 4.2.3. Since the recording of the anodic CPP curves are made to initiate pitting to see where it initiate and repassivates, this may be a result of a more stable oxide film developed during isothermal heat treatments, making it more difficult to penetrate the oxide film than for the as-delivered condition. This can result in a more noisy result. The same can be observed after recording of the polarization curve with an electrolyte temperature of 60°C. As can be seen from surface characterization after recording of the polarization curve in Figure 4.2.10b, the as-delivered sample from UNS S39274 is only affected where the pits have occurred after recording with an electrolyte temperature of 40°C. The rest of the sample seems as before the electrochemical measurements, with no damage in the oxide film. This is not the case for the other samples at this electrolyte temperature. Since the as-delivered condition has the only polarization curve without noise, this may indicate that the proposed less stable oxide film of the as-delivered samples, may be the case.

If Figure 4.2.8 is observed closely, small current density peaks can be seen before pit initiating, starting at potentials far below E_p . They are most likely metastable pits, which are pits that initiate and grow for a limited time before repassivating, often with a lifetime in the order of seconds or less. Metastable pits are able to form under conditions where stable pits do not form, and under conditions where stable pits will form they often act as precursors to stable pits. For a period, metastable pits can initiate at potentials far below E_p , where the stable pits initiate, and at potentials above E_p during the induction time before the onset of stable pitting. This provides evidence against the definition of E_p being the potential above which pits initiate. Stable pits will survive the metastable phase and continue to grow, whereas metastable pits repassivates and stop growing[49]. They should not be confused with the noisy peaks that can be seen in Figure 4.2.3.

5.3.3 T1 - isothermal heat treatment

For the W-rich UNS S39274 there was found no intermetallic precipitation or secondary phases before a holding time of 4 minutes at 846°C prior to the CPT measurements, as can be seen in Table B.3.3. This matches the results of the CPT measurements, which gave a CPT of 80°C for samples with holding times of 1 and 1.5 minutes, and 75°C for samples isothermal heat treated for 2 minutes. No intermetallic phases were found to precipitate before after a holding time of 2 minutes for the W-free UNS S32750. This is listed in Table B.3.3 and can be observed in Figure B.3.1a. However, the results showed a relatively low CPT of about 65°C after a holding time of 1 minute, while it increased to 70-75°C after 1.5 minutes holding time, which was lower than expected. The TTT-

diagram given in Figure 2.2.1 shows that χ -phase and Cr_2N starts to precipitate after 1 minute, and it has been reported that isothermal heat treatment in the temperature range 700-900°C can result in intergranular precipitation of Cr_2N after less than 1 minute [17, 18, 21]. This could explain the results. As can be seen from Table 4.2.2, the low value of E_p and E_{RP} , indicates a hysteresis for the anodic CPP curve at an electrolyte temperature of 60°C, which correlates with the CPT. For UNS S32760, a few particles were observed in Figure B.3.2e, most likely χ , after 1.5 minutes holding time. This is in accordance with the TTT diagram in Figure 2.2.1 which indicates that χ can start to precipitate prior to 1 minute in the temperature range 700-900°C. This will have a negative effect on the corrosion resistance since the χ phase consumes chromium and molybdenum as described in Section 2.2.1. Since CPT measurements showed slightly higher value of 70-75°C after 1.5 minutes holding time than the 70°C at 1 minute holding time, they do not affect the corrosion resistance noticeably. Even though there are no secondary or intermetallic phases precipitated after 1 minute of isothermal heat treatment, it seems to affect the CPT of UNS S32750 and UNS S32760, but not UNS S39274. This may be an effect of the α/γ -phase distribution in solution annealed condition. As can be seen in Table B.3.1, UNS S39274 is close to the ideal 50/50 phase distribution, while the two other are closer to and above 60/40. However, what matters the most is the partitioning of alloying elements. Table B.3.2, shows approximately the same balance of the chemical composition for UNS S32750, UNS S32760, and UNS S39274. Ferrite are more rich in chromium and molybdenum for all of the three grades, along with tungsten for UNS S32760 and UNS S39274. Whereas nickel is more enriched in the austenite. Since ferrite is slightly more rich in alloying elements and ferrite is more enriched in W-free UNS S32750 and low-W UNS S32760, the austenite is more prone to corrosion than for W-rich UNS S39274. This may explain the lower CPT for those SDSS grades. Even though the results of the anodic CPP curves showed no difference in corrosion resistance in the polarization test after heat treatments, the W-rich grade showed superior corrosion resistance to that of the low-W grade.

After 2 minutes of aging, the W-rich UNS S39274 still has a high CPT of 75°C, only a decrease of 5°C, as expected since there was not observed any intermetallic phases. This can be seen in Figure ?? and found in Table B.3.3. For UNS S32750 the increased holding time has resulted in precipitation of σ - and χ -phase. There are observed a greater volume of σ and a more numerous χ -phase in Figure B.3.1a, and as can be seen from Table B.3.3, they have approximately the same volume fraction of 0.04 vol% and 0.03%, respectively. This is in accordance with the TTT-diagram in Figure 2.2.1, which shows that the σ -phase starts to precipitate between 2 and 4 minutes at this temperature. σ is the phase that causes most concern, since it has a relatively large volume fraction and depletes chromium and molybdenum from the surrounding ferrite, leading to a decrease in corrosion resistance [2, 15, 18]. This is further described

in Section 2.2.1. The σ -phase precipitation leads to the same effect as for the χ -phase described above, but precipitates in larger scales. The CPT was measured to be 70°C, only a slightly decrease from the 70-75°C at 1.5 minutes aging. Indicating that the depletion of chromium and molybdenum is not large enough to significantly affect the corrosion resistance. However, a more significant decrease due to the precipitated σ -phase was expected. A bigger impact was observed for UNS S32760 where the CPT had decreased from 70-75°C at 1.5 minutes holding time to 65°C at 2 minutes holding time. Microstructure characterizations prior to the corrosion testing showed that the χ -phase continued to grow, even though it still was small. σ -phase was not observed in Figure B.3.2f, but there was measured a volume fraction of the σ -phase of 0.5 vol% and 0.006 vol% for the χ -phase. This can be seen in Table B.3.3. There was not observed any indication of hysteresis from the parameters obtain from the anodic CPP curves as listed in Table 4.2.2 and 4.2.3.

The first signs of intermetallic precipitation in UNS S39274 was observed after 4 minutes of isothermal heat treatment. Narrow, small particles were detected along the α/γ -grain boundaries as seen in Figure B.3.4e, but their chemical composition could not be analyzed by EDS because of their small size. CPT decreased to 65°C, 10°C lower than at 2 minutes of aging. This indicates that they have affected the corrosion resistance properties. The results are reflected by the anodic CPP curve obtained at 60°C in Figure C.1.11, which shows a small hysteresis, indicating small pits. Microstructure characterization of UNS S32750 in Figure B.3.1b showed that the amount of intermetallic phases increased drastically, particularly σ , which had consumed big parts of the α -phases, but there were still many free grain boundaries. As can be seen in Table B.3.3, the volume fraction of σ increased from 0.04 vol% to 0.3 vol%. This can also be seen from the low CPT value of 50°C for the samples isothermal heat treated for 4 minutes. The rapid reduction in CPT between 2 and 4 minutes indicates that the effect of σ , as described above, has started to affect the corrosion resistance significantly. For UNS S32760, Figure B.3.3a shows that σ was also detected after this holding time. As can be seen from Table B.3.3, both σ and χ had a volume fraction of 0.2 vol% . Since the CPT decreased from 65°C to 45°C from 2 to 4 minutes aging, the precipitation of the detritus intermetallic phases seems to have a significantly negative affect on the corrosion resistance.

Because of the relatively high CPT of UNS S39274 after 4 minutes of aging, it was decided to add another isothermal heating time of 10 minutes to the test matrix, as seen in Table 3.3.2. This gave a CPT below 40°C and an anodic CPP curve with a little hysteresis when recording with an electrolyte temperature of 40°C, which can be explained by microstructure characterizations in Figure B.3.4f, showing some σ -phase and an increased amount of χ along the grain boundaries. Table B.3.3 shows that 0.3 vol% σ and 1.4 vol% χ were detected. If UNS S32750 and UNS S32760 had been tested,

they would most likely have equally low or even lower CPT values owing their largest vol% of σ og 3.8 and 2.7, respectively, as listed in Table B.3.3. As can be seen in Figure B.3.1c, UNS S32750 have intermetallic phases decorating most of the grain boundaries at this time and Figure B.3.3b shows that UNS S32760 has α decomposition by σ and γ_2 , with relative large χ particles.

As described in Section 2.1.2, an optimal range of tungsten is known to increase the pitting corrosion resistance in SDSS[7, 4], and since the tungsten content of 0.62 wt% for UNS S32760 is below that threshold, it has been measured to have slightly lower CPT as a function of IHt than W-free UNS S32750. Except from after 1 minute of isothermal heat treatment at 846°C of UNS S32750, the CPT values as a function of IHt for UNS S32760, was the same or up to 5°C lower than for UNS S32750, as can be observed in Figure 5.3.1. A tungsten content of 2.1 wt% is in the optimal range of tungsten, and seems to have a larger impact on the corrosion resistance of SDSS. The electrochemical measurements showed a stable CPT of 75°C to 80°C before it decreased to 65°C after 4 minutes of isothermal heat treatment at 846°C, and to below 40°C after 10 minutes holding time. As can be seen in Figure 5.3.1, this is significantly better than the two other SDSS grades, indicating that an increased tungsten content will increase the pitting corrosion resistance up to a certain wt%, as discussed in Section 2.1.2[4, 7]. These results are in accordance with the results from the microstructure characterization prior to the CPT measurements, which found the rate of precipitation to increase in the order 2.1 wt% W < 0 wt% W < 0.62 wt% W-SDSS[72]. The σ -phase was found to be the dominating intermetallic phase in both the 0 wt% W- and the 0.62 wt% W-material. Whereas for the grade with 2.1 wt% W, the precipitation was delayed towards longer aging times, and the χ -phase was dominating after longer holding times, as listed in Table B.3.3. Indicating that below a critical amount of tungsten addition, precipitation of intermetallic phases is promoted and stabilized towards higher temperatures. Above this critical value, the precipitation is delayed, and χ -phase is stabilized of σ -phase[72].

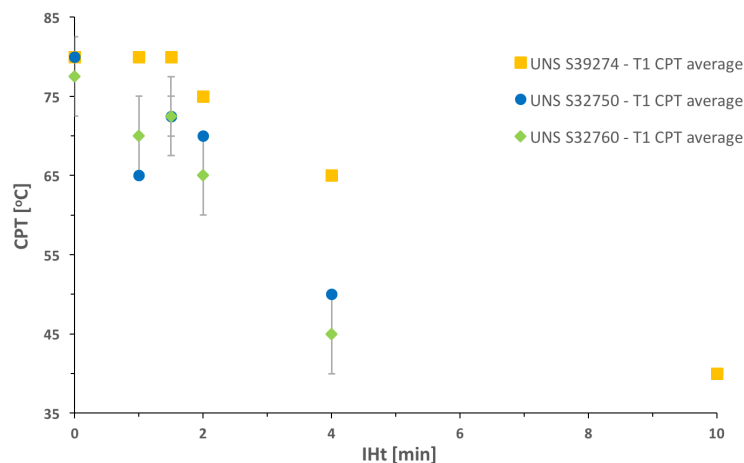


Figure 5.3.1: Comparison of CPT as a function of Iht obtained from CPT measurements of UNS S32750, UNS S32760, and UNS S39274 at 846°C.

5.3.4 T2 - isothermal heat treatment

Only UNS S32750 and UNS S32760 were tested at 790°C and 920°C. 1 minute of holding time at 790°C gave a CPT of 70-75°C for UNS S32750 and 65°C for UNS S32760. No intermetallic phases were observed for both of the SDSS grades. The same was the case after a holding time of 2 minutes, that gave a CPT between 65-75°C for UNS S32750 and at 65°C for UNS S32760. This is about the same results as for the isothermal heat treatment at 846°C for UNS S32750, but why the CPT is consistently lower for UNS S32760 is unknown. Since the temperature is lower and no intermetallic phases were observed, it was expected to be the same as for 846°C.

Small bright phases were observed at triple junctions and α/α -interfaces for UNS S32750 after 4 minutes of aging at 790°C, as can be seen in Figure B.3.1d. However, they were too small to characterize. CPT was measured to be 70-75°C, the same as after 1 minute of aging and slightly higher than after 2 minutes of aging. This indicates that the precipitation of the intermetallic phases do not affect the corrosion resistance noticeably at that time. However, the anodic CPP curve obtained at 60°C showed a hysteresis in Figure 4.2.5, indicating pitting. Since there are almost no intermetallic phases detected, CPT is most likely higher than 60°C. Even though no intermetallic phases were observed for UNS S32760, the CPT still decreased 10°C, making it 55°C. This may indicate that there was some intermetallic phases precipitated that was not detected during microstructure characterization.

After 10 minutes of aging intermetallic phases were observed in Figure B.3.1e and

B.3.3d for both UNS S32750 and UNS S32760, respectively. For UNS S32750, the bright phases could be characterized as χ - and σ -phase. The σ -phase was mainly observed at α/γ interfaces, triple junctions, and in vicinity to χ -particles. The volume of σ was greater at this point, but χ was found to be more numerous than σ . They had a volume fraction of 0.2 vol% and 0.1 vol%, respectively. χ was precipitated as elongated particles along the majority of α/α -grain boundaries or intergranular in α . UNS S32760 had most of α/α - and γ/α -grain boundaries covered in χ and σ , where σ had started to consume α . Table B.3.3 shows that both σ and χ have a volume fraction of 0.2 vol%. It was only UNS S32750 that was tested at this aging time. This is because it was added to the test matrix given in Table 3.3.2, to see if the decrease in CPT was less rapid than the decrease from 4 to 20 minutes of aging. As for 20 minutes of aging, the CPT of UNS S32750 was measured to be below 40°C at a 10 minutes holding time. At 20 minutes of aging, Figure B.3.1f shows that UNS S32750 still had χ -phase and the σ -phase had grown substantially to 3.9 vol%. For UNS S32760, Figure B.3.3e shows that the χ -phase continued growing along the grain boundaries and the σ -phase continued consuming α , giving volume fractions of 0.8 vol% and 4.3 vol%, respectively. CPT for UNS S32760 was also measured to be below 40°C at 20 minutes of aging. Most likely, it would have been below 40°C with a holding time of 10 minutes as well, due to the great volume fraction of intermetallic phases.

It can be observed from Figure 5.3.2 that UNS S32750 have a larger value of CPT as a function of IHt than UNS S32760, which is in accordance with the amount of intermetallic phases precipitated. Table B.3.3, shows that UNS S32760 has a larger volume fraction of σ and χ at all of the holding times. As discussed in Section 5.3.3, the tungsten content of 0.62 wt% is not in the range that gives improved pitting corrosion resistance[4, 7].

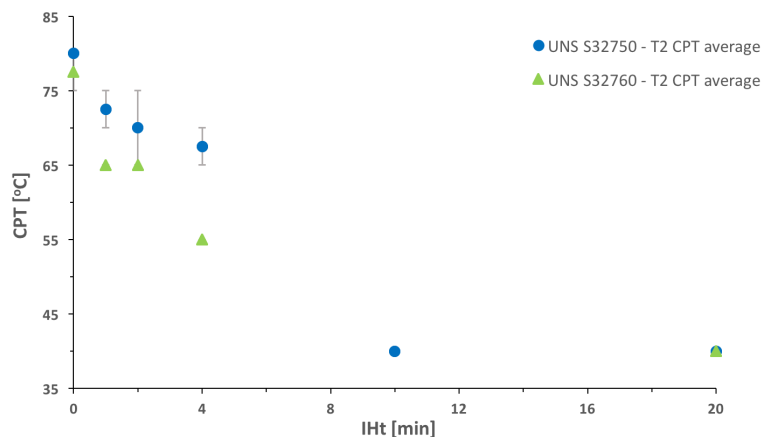


Figure 5.3.2: Comparison of CPT as a function of IHt obtained from CPT measurements of UNS S32750 and UNS S32760 at 790°C.

5.3.5 T3 isothermal heat treatment

With a temperature of 920°C and a holding time of 1 minute, the CPT measurement gave CPT of 70-75°C and 70°C for UNS S32750 and UNS S32760, respectively. Microstructure characterization shows no precipitation of intermetallic phases for UNS S32750, whereas a relatively large volume of precipitates was observed in Figure B.3.3f for UNS S32760. One of the detected phases could be characterized as σ and had a volume fraction of 0.03 vol%, but the other phase, most likely χ , was too small to analyze with EDS. Something suspected to be Cr_2N was also observed. The amount of intermetallic phases was significantly higher than the amount observed after 1.5 minutes of aging at 846°C and after 2 minutes of aging at 790°C for UNS S32750. This was not reflected in the CPT value of 70°C, which is similar to the CPT after 1.5 minutes of aging at 846°C at 70-75°C, and higher than the CPT of 65°C after 2 minutes of aging at 790°C for UNS S32750.

After a holding time of 2 minutes, electrochemical measurements on UNS S32750 and UNS S32760 gave CPT of 70-75°C and 70°C respectively. This is approximately the same as for 846°C and slightly higher than for 790°C. There was observed χ - and σ -phase, and something suspected to be Cr_2N , for UNS S32750 in Figure B.3.2a. The χ -phases were small and few, while the σ -phases were larger with a volume fraction of 0.06 vol%. For UNS S32760, it can be observed in Figure B.3.4a that σ and χ continued growing, but not to that extent that it is noticed in the CPT value. At 4 minutes of aging, the χ - and σ -phase continued growing of UNS S32750 and the volume fraction of σ had increased from 0.05 to 0.2 vol%, but the CPT does still have a stable value of 70-75°C. As for aging at 790°C for 4 minutes, the anodic CPP curve obtained at 60°C, which can be observed in Figure C.1.8, showed a hysteresis. Since there are more intermetallic phases measured at 920°C than at 790°C, it is more likely that the measured CPT is too high at 920°C. The σ - and χ -phase also continued growing for UNS S32760, as can be seen in Figure B.3.4b, which was visible at the decreased value of CPT to 60-65°C.

As for 790°C, UNS S32750 was the only grade tested at 10 minutes of aging, which gave a CPT of 45-50°C. This is higher than at 790°C, which measured a CPT below 40°C. It could be observed from Figure B.3.2c that most of the grain boundaries were decorated with intermetallic precipitations, especially σ -phase that increased from 0.2 vol% to 3.1 vol%, as listed in Table B.3.3. After 10 minutes holding time, Figure B.3.4c of UNS S32760 showed a microstructure with almost all grain boundaries decorated with intermetallic precipitates. The σ -phase continued to grow, and after 20 minutes Figure B.3.4d shows that almost all of the α -phase was consumed by σ and γ_2 , between the layers of σ . 30.2 vol% of the sample was covered with σ . CPT was measured to be below 40°C, as expected with the great amount of precipitates. The same was the case

for UNS S32750, where it could be observed from Figure B.3.2d that the intermetallic phases had continued growing at 20 minutes of aging. σ was present at a volume fraction of 9.3 vol% and γ_2 was also detected at this grade. This poor corrosion resistance may also be due to increased χ -phase precipitation, which consumes chromium and molybdenum as described in Section 2.2.1. This leads to a formation of γ_2 from ferrite[21, 22]. Since chromium and molybdenum increase the corrosion protection in SDSS, as proposed by the PRE_N in Equation 2.4.2, the χ -phase decreases the corrosion resistance. As described in Section 2.2.1, γ_2 rejects chromium and molybdenum and absorbs nitrogen, leading to a lower chromium and molybdenum concentration than in primary ferrite and a decreased corrosion resistance in that phase[17, 21]. The metallic contact between the χ -phase and γ_2 further decrease the corrosion resistance, since χ is more noble than γ_2 . This may enhance the dissolution of γ_2 and give galvanic corrosion as if there were two dissimilar metals, as described in Section 2.3.2. Since all of the other phases are more noble and have a larger area than γ_2 , the corrosion rate will most likely be enhanced[52].

As can be seen from Figure 5.3.3, UNS S32750 have greater value of CPT as a function of IHt than UNS S32760. Which is in accordance with literature, proposing that a tungsten content of 0.62 wt% is not in the range that have an positive effect of the pitting corrosion resistance[4, 7].

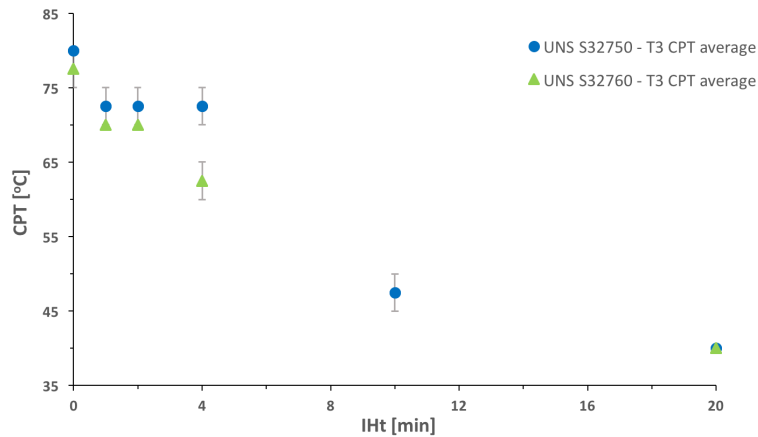


Figure 5.3.3: Comparison of CPT as a function of IHt obtained from CPT measurements of UNS S32750 and UNS S32760 at 920°C.

The objective with the electrochemical measurements was to determine the critical IHt for the three SDSS grades at given isothermal heat treatment temperatures, by observing reduction in localized corrosion resistance. At 846°C, Figure 5.3.1 shows CPT as a function of IHt, where a rapid reduction in CPT, and thereby decreased corrosion resistance, can be observed between 2 and 4 minutes for UNS S32750. Indicating that

the critical IHT may be in that time interval. The low CPT after 1 minute of isothermal heat treatment may be an exception, but characterization with SEM gives no more clarification, as described above. For UNS S32760, there can also be observed a rapid decrease in OCP between 2 and 4 minutes, indicating that the critical IHT may be in that time interval. UNS S39274 shows a better corrosion resistance with a critical IHT in the time interval 4 to 10 minutes. At 790°C, Figure 5.3.2 shows that UNS S32750 has a rapidly decreasing CPT value between 4 and 10 minutes. The same can be observed in Figure 5.3.3 at 920°C, indicating that this is the critical time interval for the corrosion resistance of UNS S32750 at those temperatures. For UNS S32760, the critical IHT was found to be in the time interval from 4 to 20 minutes for both 790°C and 920°C, since they were not tested at 10 minutes of aging.

5.4 Surface characterization after electrochemical measurements

5.4.1 After CPT measurements

Table B.1.1 shows that there are individual differences in weight loss between samples with the same isothermal heat treatments after CPT measurements, as can be seen in Figure 4.1.8a and B.4.3a. Indicating that weight loss only is an indication of pitting corrosion, and not something that can be used to determine the susceptibility to pitting or the amount of intermetallic phases. The results of the CPT measurements, as given in Figure 4.1.1, 4.1.2, and 4.1.3 shows that the OCP decreases rapidly after reaching 500 mV_{SCE} for the isothermal heat treatments with high CPT. However, for the samples with lower CPT the decrease is slower, as discussed in the beginning of this chapter. By comparing these results with the weight losses shown in Table B.1.1, it can be observed that the most severe weight loss are found among the samples with high CPT, indicating a more rapid pitting corrosion at lower potentials. Which again indicates that longer holding time at lower potentials is the main factor for the amount of weight loss, and thereby pitting. Thus, it is not the IHT, but how long the samples are immersed in the electrolyte after the OCP is below 500 mV_{SCE} that is the main factor for the amount of pitting corrosion.

Surface characterization of selected samples by OM after the CPT measurements performed in this thesis can be found in Figure 4.1.7, 4.1.8. The rest of the samples can be found in Appendix in Figure B.4.1 to B.4.3. They show different amounts of pitting, as described above, and pitting corrosion was mainly observed in the middle of the samples, but some corrosion was also observed at the edges and around the hole. Some samples showed such amount of pitting that it was impossible to see where it

had initiated, as in Figure 4.1.8b. Examples of corrosion around edges and holes can be seen in Figure 4.1.9d and 4.1.9e, respectively, where cracks have appeared along the edges and around the hole. This may be a result of crevice corrosion which have initiated due to crevices or holes on the metal surface[51]. It is not unlikely that crevices appeared around the hole during machining or at the edges during grinding since it was performed manually. As mentioned in Section 2.4.1, small pits are often covered by remnant of the undermined passive film in stainless steels, and larger pits can be covered with a metal layer detached from the rest of the metal. It is often of a considerable thickness and do still remain reflecting, making optical detection of the pits extremely difficult[29]. Examples of this can be seen in Figure 4.1.9c, 4.1.9c, and 4.1.9f, where residues from the metal layer that used to cover the pit is shown.

5.4.2 After recording of anodic CPP curves

When recording the anodic CPP curves, the samples are driven to a state where pitting initiate, demonstrating that pitting will be observed on all of the samples after the electrochemical measurements. This is shown in Figure 4.2.10, 4.2.11, and 4.2.12, together with Figure C.2.1, C.2.2, and Figure C.2.3 in Appendix.

All the samples after anodic CPP measurements at 40°C have small pits on the surface, but the amount of pitting varies between the different conditions. As can be seen from Figure 4.2.10b, the as-delivered sample from UNS S39274 is only affected where the pits have occurred, where the rest of the sample is as before the electrochemical measurements. This is not the case for the other samples. Figure C.2.1a and 4.2.10a shows that the as-delivered and solution annealed UNS S32750 samples had a few small pits and. The solution annealed sample had also a slightly change of color after the recording of the polarization curve, whereas UNS S39274 aged at 846°C for 4 minutes, given in Figure 4.2.10c, had more pits and a more significant change in color. Indicating that the amount of pitting increases with the amount of intermetallic phase, which is also the case for the damage of the oxide film. A high amount of secondary and intermetallic phases leads to more depleted zones, which increases the amount of initiation sites for pitting corrosion.

Significant differences can be observed at the samples after recording polarization curves with an electrolyte temperature of 60°C. A hysteresis can be observed for the polarization curve for the as-delivered UNS S32750 condition, as can be seen in Figure 4.2.4. Corrosion can be observed all over the sample shown in Figure 4.2.11a, together with small pits spread homogeneously over the surface. Figure 4.2.11b show almost no pitting for the UNS S32750 sample aged at 790°C for 4 minutes, but shows damage in the oxide film. The anodic CPP curve in Figure 4.2.5 show a small hysteresis, which is not in accordance with a CPT of 70°C. As can be seen from Figure C.2.3, the samples

with an CPT close to 80°C, do not have many big pits, but there are more damage in the oxide film than at lower recording temperatures. Indicating that there are more pitting close to or above CPT, but there are more damage in the overall oxide film. This is also indicates that the measured CPT is too high. No hysteresis can be observed for the UNS S39274 aged at 846°C for 1 minute in Figure 4.2.6, but the pits in Figure 4.2.11c is bigger than at 40°C. Indicating that the pit size increases with increasing electrolyte temperature because the electrolyte temperature is getting closer to the CPT.

By comparing the anodic CPP curves obtained at 80°C in Figure 4.2.7, 4.2.8, and 4.2.9 with the correlating surface characterizations given in Figure 4.2.12, it can be observed that the size of the hysteresis is reflected in the surface characterization. At this temperature all of the conditions showed signs of pitting, which matches the results from the CPT measurements. A big hysteresis with a relatively large difference between the value of E_p and E_{RP} , gave a surface with a few big pits, while a more narrow hysteresis with E_{RP} closer to E_p gave a surface with more, but smaller pits. Almost no pits could be observed at the surface when the anodic CPP curved showed a even more narrow hysteresis. Indicating that the size of the hysteresis gives an indication of the size and amount of the pits.

5.4.3 Pit initiating

Selected samples from W-free UNS S32750 and W-rich UNS S39274 with different heat treatments were also examined using the backscattered electron signal of SEM (SEM-BSE) as it is more sensitive than an optical microscope in detecting intermetallic phases. The SEM-BSE micrographs can be found in Figure 4.1.10 and 4.1.11. The objective with this was to establish if the pitting had occurred in the intermetallic phases, austenite, ferrite, or along the grain boundaries, and in what direction the pits grew. It was not possible to separate the secondary phases at the magnifications selected for these micrographs, but the phases that was present prior the electrochemical measurements was characterized by another student[72]. Some of the results from those measurements can be found in Section B.3 and are included in Table 4.1.1. They are also included when discussing the results from the electrochemical measurement, to help understand the effect of tungsten and the isothermal heat treatments. Intermetallic phases can be seen as bright inclusions due to the high content of molybdenum, which have a significantly larger atomic scattering factor than the other elements. The γ -phase appears slightly brighter than the α -phase.

To establish if the pitting had occurred in the depleted areas around the intermetallic phases, austenite, ferrite, or along the grain boundaries, and in what direction the pits grew, SEM-BSE was used to characterize the surface. These pictures are found in Figure 4.1.10 and 4.1.11. As discussed above, the amount of pitting after CPT measure-

ments is mainly due to the holding time after pit initiating and the value of CPT. Thus, these micrographs are used to determine where the pits initiated and not the amount or size. Pitting corrosion can occur in either phase depending on the alloying elements [49]. Pitting corrosion is further described in Section 2.4. The austenite grains appear brighter than the ferrite grains in SEM and the precipitated intermetallic phases appear bright due to their high content of molybdenum. Whereas the bright area around the pits are residue from the corrosion products, which also is high in heavy metals. It was not possible to separate the intermetallic phases at the magnifications selected for these micrographs, but the phases that were present prior to the electrochemical measurements were characterized by another student [72]. Some of the results from those measurements can be found in Section B.3 and are included in Table 4.1.1.

To achieve a greater understanding of the effect of tungsten on the corrosion resistance of SDSS, the micrographs of the W-free UNS S32750 and W-rich UNS S39274 samples heat treated at 846°C were compared. No precipitation of intermetallic phases were observed in Figure 4.1.10a, UNS S32750 isothermal heat treated for 1 minute, which is in accordance with microstructure characterization prior to electrochemical measurements. Pitting is mainly observed inside austenite grains, but also some pitting along the α/γ boundaries and in the ferrite domains. With a holding time of 2 minutes, small amounts of σ and χ were observed, as listed in Table B.3.3 and as previously discussed. However, the surface characterization after CPT measurements, given in Figure 4.1.10b, show no precipitation of intermetallic phases. This may be due to the pits having initiated in the depleted areas around and grown past the intermetallic phases or that the magnification was too little. As for after 1 minute of aging, pitting was mainly observed inside the austenite grains, but also some corrosion along the α/γ boundaries and inside ferrite grain. For UNS S39274, the solution annealed condition showed no intermetallic phases, as expected and in accordance with Table B.3.3 and earlier discussions. Figure 4.1.11b shows that pitting is mainly observed inside α grains and along the α/γ boundaries. As can be seen in Figure 4.1.11c, this is also the case after 2 minutes of aging. After 4 minutes of aging for UNS S32750, Figure 4.1.10c shows that σ -phase, as characterized in Table B.3.3, has precipitated along the grain boundaries. It can be observed that some of the pits have initiated in the depleted areas around the σ -phase, whereas the other pits have initiated in the γ -domain. For UNS S39274 after 10 minutes of aging, as shown in Figure 4.1.11d and 4.1.11e, precipitation of σ - and χ -phase along the grain boundaries and inside the grains are observed and characterized in Table B.3.3. Pitting is observed to mainly initiate in the depleted areas around those phases, which is in accordance with literature, and inside ferrite grain. The increased precipitation of intermetallic phases are reflected in the low CPT below 40 °C.

To examine where pitting initiates at larger amounts of intermetallic phases, the pit-

ting corrosion of UNS S32750 was also studied closer at 20 minutes of aging at 790°C, as shown in Figure 4.1.10d and 4.1.10e and at 4 minutes of aging at 920°C, as shown in Figure 4.1.10f and 4.1.11a. After 20 minutes of aging at 790°C, precipitation of intermetallic phases, mainly along the grain boundaries were observed, and the pits were found to initiate at the depleted areas around those inclusions. Some pits were also found to initiate inside the γ -grains. After 4 minutes of aging at 920°C, some precipitation of intermetallic phases can be observed at triple junctions and along the grain boundaries. It is in the depleted areas around those phases the pits were found to initiate.

The SEM-BSE micrographs after CPT measurements shows that pits mainly initiate at the depleted areas around intermetallic phases when they are present, but when they are not, pits were found to mainly initiate inside the austenite domains for W-free UNS S32750 and inside the ferrite domains for W-rich UNS S39274.

5.5 Limitations and sources of error

There were temperature differences in the oven during both solution annealing and isothermal heat treatments. The samples were placed on a SDSS tray that approximately had the size of an A4 sheet, indicating different individual heat treatment temperatures. During isothermal heat treatment, the samples were placed close to each-other in the front of the oven, giving almost the same heating temperature. The temperature dropped quickly when the door was opened to insert the samples, often in the matter of 10°C to 20°C in a few seconds. For the shortest aging times below 2 minutes, the time to reach the target temperature was longer than the aging time. This could influence the microstructure, especially at shorter holding times. By working in pair, the temperature loss in the furnace when inserting the samples was reduced. This also made it possible to remove the samples faster from the furnace to the water quenching, reducing the cooling time.

The samples were placed in a desiccator prior to electro chemical measurements to passivate. They were held there for at least 24 hour, but often longer. The holding time varied between the samples, which may affect their corrosion resistance. As discussed in Section 5.4, the amount of pitting and weight loss during CPT measurements was mainly dependent on the holding time after initiating of pitting corrosion.

The temperature was increased by 5°C during CPT measurements. This gives rounded values of CPT, and may give an error of 4°C. Surface characterization of some of the samples indicated that there was some corrosion initiating close to the platinum thread. This may cause crevice corrosion or other corrosion mechanisms. The electrolyte tem-

perature in the CPT measurements was regulated by a temperature regulator in the solution, which had an uncertainty of $\pm 2^\circ\text{C}$. This could contribute to some small experimental errors. Because of noise during anodic CPP, the temperature regulator was turned off prior to OCP measurements. The temperature was relatively stable because of the water bath, but it could have changed during the measurements.

Chapter 6

Conclusion

The effect of tungsten and isothermal heat treatment on the pitting corrosion resistance of SDSS was investigated in this thesis. Two SDSS grades, W-free UNS S32750 and W-rich UNS S39274 was investigated by electrochemical measurements and the results was compared to results from the same electrochemical measurements on low-W UNS S32760 and to microstructure characterizations prior to electrochemical measurements. How intermetallic and secondary phases like σ -phase, χ -phase and γ_2 affected the pitting corrosion resistance was emphasized. The work led to the following conclusions:

- CPT was found to generally decrease with increasing isothermal heating time and thus, increasing precipitation rate and amount of intermetallic phases.
- W-rich UNS S39274 was found to have a significantly better result of CPT as a function of isothermal heating time than W-free UNS S32750 and UNS S32760 at 846°C. Thus, W additions of 2.1 wt% in SDSS promotes better pitting corrosion resistance than 0.62 wt% W and no W.
- W-free UNS S32750 was found to have slightly better result of CPT as a function of isothermal heating time for the three temperatures, 790°C, 846°C, and 920°C. Thus, SDSS without W promotes better pitting corrosion resistance than additions of 0.62 wt% W.
- The critical isothermal heating time was found to be between 2 and 4 minutes for the W-free UNS S32750 and between 4 and 10 minutes for W-rich UNS S39274.
- When secondary and intermetallic phases was present, pitting was found to mainly initiate at the depleted areas around those inclusions.
- The results obtained from the anodic CPP curves was found to generally corre-

late with the results from the CPT measurements.

Chapter 7

Further work

To achieve a larger understanding of the effect of tungsten and isothermal heat treatments on the pitting corrosion resistance of SDSS, the following is recommended for further work:

- Isothermal aging at 790°C and 920°C for UNS S39274, to further compare the effect of tungsten and isothermal heat treatments on the pitting corrosion resistance of SDSS.
- Start the CPT measurements at 20°C for the aging conditions that had CPT below 40°C, to get a more precise result.
- Add more holding times to the test matrix for CPT measurements in the critical isothermal heating time interval, to get a more precise critical heating time.
- Optimize the solution annealing to achieve similar phase distribution of ferrite and austenite.
- Optimize the solution annealing to achieve even heat distributions.
- Optimize the isothermal heat treatments to achieve wanted temperatures.

Bibliography

- [1] J. Charles. Super duplex stainless steels: structure and properties. pages 151–168, 1991.
- [2] Alfred R Akisanya, Udoka Obi, and Neill C Renton. Effect of ageing on phase evolution and mechanical properties of a high tungsten super-duplex stainless steel, 2012.
- [3] R. A. Perren, T. A. Suter, C. Solenthaler, G. Gullo, P. J. Uggowitzer, H. Böhni, and M. O. Speidel. Corrosion resistance of super duplex stainless steels in chloride ion containing environments: investigations by means of a new microelectrochemical method. *Corrosion Science*, 43:707–726, 2001.
- [4] H. Ogawa, K. and Okamoto, M. Ueda, M. Igarashi, T. Mori, and T. Kobayashi. Effects of tungsten on pitting corrosion resistance and impact toughness in the haz of duplex stainless steel - study of weldability of high-tungsten duplex stainless steel (1st report). *Welding International*, 10:466–472, 1996.
- [5] Henrik Sieurin and Rolf Sandström. Sigma phase precipitation in duplex stainless steel 2205. *Materials Science and Engineering A*, 444(1):271–276, 2007.
- [6] K. Ogawa, H. Okamoto, M. Igarashi, M. Ueda, T Mori, and T. Kobayashi. Effects of tungsten on precipitation behaviour of intermetallic compounds in the haz of duplex stainless steel: Study of weldability of high-tungsten duplex stainless steel. *Welding International*, 11:14–22, 1997.
- [7] J. S. Kim and H. S. Kwon. Effects of tungsten on corrosion and kinetics of sigma phase formation of 25% chromium duplex stainless steels. *Corrosion*, 55:512–521, 1999.
- [8] J. Charles. The duplex stainless steels: materials to meet your needs. In *Duplex stainless steels*, pages 3–48. Les Editions de Physique, 1991.
- [9]

- [10] C.-O.A Olsson and D. Landolt. Passive films on stainless steels—chemistry, structure and growth. *Electrochimica Acta*, 48:1093 – 1104, 2003.
- [11] R. F. A. Jargelius-Pettersson. Application of the pitting resistance equivalent concept to some highly alloyed austenitic stainless steels. *Corrosion*, 54:162–168, 1998.
- [12] H.K.D.H. Bhadeshia and Sir Robert Honeycombe. *Steels - Microstructure and Properties*. Butterworth Heinemann, third edition, 2006.
- [13] E. H. Haugan, M. Næss, R. Johnsen, and M. Iannuzzi. Effect of tungsten on pitting and crevice corrosion of type 25cr super duplex stainless steel. *NACE International*, pages 1–10, 2016.
- [14] L. Weber and P.J. Uggowitzer. Partitioning of chromium and molybdenum in super duplex stainless steels with respect to nitrogen and nickel content. *Materials Science and Engineering: A*, 242(1–2):222 – 229, 1998.
- [15] N. Ebrahimi, M. Momeni, M.H. Moayed, and A Davoodi. Correlation between critical pitting temperature and degree of sensitisation on alloy 2205 duplex stainless steel. *Corrosion Science*, 53:637–644, 02 2011.
- [16] H. Vannevik, J.-O. Nilsson, J. Frodigh, and P. Kangas. Effect of elemental partitioning on pitting resistance of high nitrogen duplex stainless steels. *ISIJ International*, 36(7):807–812, 1996.
- [17] Juan Manuel Pardal, Souto Maior Tavares, Maria da Penha Cindra Fonseca, Adailson de Souza, Lorena Menezes Vieira, and Hamilton Ferreira Gomes de Abreu. Deleterious phases precipitation on superduplex stainless steel UNS S32750: characterization by light optical and scanning electron microscopy. *Materials Research*, 13:401 – 407, 09 2010.
- [18] R. A. Perren, T. A. Suter, P. J. Uggowitzer, L. Weber, R. Magdowski, H. Böhni, and M. O. Speidel. Corrosion resistance of super duplex stainless steels in chloride ion containing environments: investigations by means of a new microelectrochemical method - ii influence of precipitates. *Corrosion Science*, 43:727–745, 2001.
- [19] Niklas Pettersson and Rachel F. Pettersson. Precipitation of chromium nitrides in the super duplex stainless steel 2507. *Metallurgical and Materials Transactions A*, 46:1062–1072, 2015.
- [20] X. G. Wang, D. Dumortier, and Y. Riquier. Structural evolution of zeron 100 duplex stainless steel between 550 and 1000 c. In *Duplex stainless steels*, pages 127–134. Les Editions de Physique, 1991.

- [21] J. O. Nilsson. Super duplex stainless-steels. *Materials Science and Technology*, 8:685–700, 1992.
- [22] Michael Pohl, Oliver Storz, and Thomas Glogowski. Effect of intermetallic precipitations on the properties of duplex stainless steel. *Materials Characterization*, 58(1):65 – 71, 2007.
- [23] K. W. Chan and S. C. Tjong. Effect of secondary phase precipitation on the corrosion behavior of duplex stainless steels. *Materials*, 7:5268–5304, 2014.
- [24] Prabhu Paulraj and Rajnish Garg. Effect of intermetallic phases on corrosion behavior and mechanical properties of duplex stainless steel and super-duplex stainless steel. *Advances in Science and Technology Research Journal*, 9:87–105, 2015.
- [25] Fe-cr phase diagram. http://www.calphad.com/pdf/Fe_Cr_Phase_Diagram.pdf. Accessed: 2017-05-23.
- [26] K. Sugimoto and Y. Sawada. The role of molybdenum addition to austenitic stainless steel to the inhibition of pitting in acid chloride solutions. *Corrosion Science*, 17:425–445, 1977.
- [27] I. Olefjord and B.-O. Elfström. The composition of the surface during passivation of stainless steels. *Corrosion*, 38:46–52, 1982.
- [28] R.C Newman. The dissolution and passivation kinetics of stainless alloys containing molybdenum - i. coulometric studies of fe-cr and fe-cr-mo alloys. *Corrosion Science*, 25:331–339, 1985.
- [29] G. S. Frankel. Pitting corrosion of metals - a review of the critical factors. *Journal of Electrochemical Society*, 145, 1998.
- [30] Eirik B. Haugan, Monika Næss, Cristian Torres Rodriguez, Roy Johnsen, and Mariano Iannuzzi. Effect of tungsten on the pitting and crevice corrosion resistance of type 25cr super duplex stainless steels. 73:53–67, 2017.
- [31] Y. S. Ahn and J. P. Kang. Effect of aging treatments on microstructure and impact properties of tungsten substituted 2205 duplex stainless steel. *Materials Science and Technology*, 16:382–388, 2000.
- [32] Hyuck Mo Lee, Samuel M. Allen, and Mica Grujicic. Coarsening resistance of m₂c carbides in secondary hardening steels: Part ii. alloy design aided by a thermochemical database. *Metallurgical Transactions A*, 22(12):2869–2876, 1991.
- [33] Soon-Hyeok Jeon, Soon-Tae Kim, In-Sung Lee, Ji-Soo Kim, Kwang-Tae Kim, and Yong-Soo Park. Effects of w substitution on the precipitation of secondary phases

- and the associated pitting corrosion in hyper duplex stainless steels. *Journal of Alloys and Compounds*, 544:166–172, 2012.
- [34] A. Irhzo, Y. Segui, N. Bui, and F. Dabosi. The role of alloyed tungsten on the conductivity of stainless steel passive layers. *Corrosion Science*, 26:769–780, 1986.
- [35] Chen Jia and Wu Jiann Kuo. The improved passivation of iron induced by additions of tungsten. *Corrosion Science*, 30:53–58, 1990.
- [36] M.B Ives, Y.C Lu, and J.L Luo. Cathodic reactions involved in metallic corrosion in chlorinated saline environments. *Corrosion Science*, 32(1):91 – 102, 1991.
- [37] L. F. Garfias-Mesias and J. M. Sykes. Effect of copper on active dissolution and pitting corrosion of 25cr duplex stainless steels. *Corrosion*, 54:40–47, 1998.
- [38] R.C. Newman and T. Shahrabi. The effect of alloyed nitrogen or dissolved nitrate ions on the anodic behavior of austenitic stainless steel in hydrochloric acid. *Corrosion Science*, 27(8):827 – 838, 1987.
- [39] Fe-ni phase diagram. http://www.calphad.com/pdf/Fe_Ni_Phase_Diagram.pdf. Accessed: 2017-05-23.
- [40] S. K. Ghosh and S. Mondal. High temperature ageing behaviour of a duplex stainless steel. *Materials Characterization*, 59:1776–1783, 2008.
- [41] Yanjun Guo, Jincheng Hu, Jin Li, Laizhu Jiang, Tianwei Liu, and Yanping Wu. Effect of annealing temperature on the mechanical and corrosion behavior of a newly developed novel lean duplex stainless steel. *Materials*, 7, 2014.
- [42] R. F. Steigerwald. The effects of metallic second phases in stainless steels. *Corrosion*, 33:338–344, 1977.
- [43] R. Sriram and D. Tromans. Pitting corrosion of duplex stainless-steels. *Corrosion*, (10):804–810, 10 1989.
- [44] J. O. Nilsson and A. Wilson. Influence of isothermal phase transformations on toughness and pitting corrosion of super duplex stainless steel saf 2507. *Materials Science and Technology*, 9:545–554, 1993.
- [45] G. Lacombe, P. Baroux, and B. Beranger. *Stainless steels*. ASM International, first edition, 1993.
- [46] ISO 17864. Corrosion of metals and alloys - determination of the critical pitting temperature under potentiostatic control. Standard, the International Organization for Standardization, 2005.

- [47] R. Cervo, P. Ferro, A. Tiziani, and F. Zucchi. Annealing temperature effects on superduplex stainless steel uns s32750 welded joints. ii: pitting corrosion resistance evaluation. *Journal of Materials Science*, 45(16):4378–4389, 2010.
- [48] J. R. Galvele. Tafels law in pitting corrosion and crevice corrosion susceptibility. *Corrosion Science*, (47):3053–3067, 2005.
- [49] L. F. Garfias-Mesias and J. M. Sykes. Metastable pitting in 25 cr duplex stainless steel. *Corrosion Science*, 41:959–987, 1999.
- [50] N. J. Laycock, J. Stewart, and R. C. Newman. The initiation of crevice corrosion in stainless steels. *Corrosion Science*, 39:1791–1809, 1997.
- [51] A. U. Malik, N. A. Siddiqi, S. Ahmad, and I. N. Andijani. The effect of dominant alloy additions on the corrosion behavior of some conventional and high-alloy stainless-steels in seawater. *Corrosion Science*, 35:1521–1535, 1995.
- [52] Kemal Nisancioglu. *Corrosion basics and engineering*.
- [53] Dominique Thierry, Charles Laballeur, and Nicolas Larché. Galvanic series in seawater as a function of temperature, oxygen content, and chlorination. *NACE International*, pager no. 7058:1–11, 2016.
- [54] T. P. Hoar, D. C. Mears, and G. P. Rothwell. The relationships between anodic passivity, brightening and pitting. *Corrosion Science*, 5:279–289, 1965.
- [55] G. S. Frankel, L. Stockert, F. Hunkeler, and H. Boehni. Metastable pitting of stainless steel. *Corrosion*, 43:429–536, 1987.
- [56] N. J. Laycock and R. C. Newman. The use of pitting transients to test microscopic models of localized corrosion. *Materials science forum*, 192:649–662, 1995.
- [57] Jose R. Galvele. Transport processes and the mechanism of pitting of metals. *Journal of The Electrochemical Society*, 123, 1976.
- [58] G. S. Frankel, Tianshu Li, and J. R. Scully. Localized corrosion: Passive film breakdown vs pit growth stability. *Journal of The Electrochemical Society*, 164:C180–C181, 2017.
- [59] R.C Newman. The dissolution and passivation kinetics of stainless alloys containing molybdenum - ii. dissolution kinetics in artificial pits. *Corrosion Science*, 25:341–350, 1985.
- [60] NORSOK M-001. Materials selection. Standard, Standards Norway, Lysaker, Norway, 09 2014.

- [61] ISO 21457. Petroleum, petrochemical and natural gas industries – materials selection and corrosion control for oil and gas production systems. Standard, the International Organization for Standardization, Geneva, Switzerland, 2010.
- [62] J. O. Nilsson, P. Kangas, A. Wilson, and T. Karlsson. Mechanical properties, microstructural stability and kinetics of σ -phase formation in 29cr-6ni-2mo-0.38n super duplex stainless steel. *Metallurgical and Materials Transactions A: Physical Metallurgy and Materials Science*, 31:35–45, 2000.
- [63] M. Pourbaix. *Atlas of Electrochemical Equilibria in Aqueous Solutions*. Pergamon Press, 1. edition, 1966.
- [64] B. E. Wilde and E. Williams. The use of current/voltage curves for the study of localized corrosion and passivity breakdown on stainless steels in chloride media. *Electrochimica Acta*, 16:1971–1985, 1971.
- [65] ASTM G61-86. Standard test method for conducting cyclic potentiodynamic polarization measurements for localized corrosion susceptibility of iron-, nickel-, or cobalt-based alloys. Standard, ASTM International, West Conshohocken, PA, 2014.
- [66] Mariano Iannuzzi. Localized corrosion resistance of corrosion resistant alloys. *Robust Materialvalg i Oljeindustrien*, 2013.
- [67] M. Næss, R. Johnsen, and M. Iannuzzi. Use of electrochemical techniques to determine the effect of sigma (σ)-phase precipitation on a 25 wt% cr super duplex stainless steel. paper no. 5595, 2015.
- [68] N. Sridhar and G. A. Cragolino. Applicability of repassivation potential for long-term prediction of localized corrosion of alloy 825 and type 316l stainless steel. *Corrosion*, 49:885–894, 1993.
- [69] D. S. Dunn, G. A. Cragolino, and N. Sridhar. An electrochemical approach to predicting long-term localized corrosion of corrosion-resistant high-level waste container materials. *Corrosion*, 56:90–104, 2000.
- [70] ASTM G48. Standard test methods for pitting and crevice corrosion resistance of stainless steels and related alloys by use of ferric chloride solution. Standard, ASTM International, West Conshohocken, PA, 2011.
- [71] Troels Mathiesen, Torben Steen Nielsen, Trond Haugen, Bard Espelid, Peter Hummelgaard, and Kari Vilpponen. Improved method for astm g48 corrosion testing of welds. Technical report, 03 2004.

- [72] Mia Bernås. Microstructural evolution during isothermal heat treatment of super duplex stainless steels as a function of tungsten content. Master's thesis, Norwegian University of Science and Technology, NTNU, 2017.
- [73] Hege Kokslien Østvold. Pitting corrosion of super duplex stainless steel without tungsten - effect of isothermal heat treatment. Specialisation project, Norwegian University of Science and Technology, NTNU, 12 2016.
- [74] Gordon Aylward and Tristan Findlay. *SI Chemical Data*. John Wiley & Sons Australia, sixth edition, 2008.
- [75] Christian Lauritsen. Pitting corrosion of super duplex stainless steel - effect of isothermal heat treatment. Master's thesis, Norwegian University of Science and Technology, NTNU, 2016.

Appendix A

Material data sheet

SANDVIK SAF 2507

TUBE AND PIPE, SEAMLESS

DATASHEET

Sandvik SAF 2507 is a super-duplex (austenitic-ferritic) stainless steel for service in highly corrosive conditions. The grade is characterized by:

- Excellent resistance to stress corrosion cracking (SCC) in chloride-bearing environments
- Excellent resistance to pitting and crevice corrosion
- High resistance to general corrosion
- Very high mechanical strength
- Physical properties that offer design advantages
- High resistance to erosion corrosion and corrosion fatigue
- Good weldability

STANDARDS

- Uns: S32750
- EnNumber: 1.4410
- EnName: X 2 CrNiMoN 25-7-4
- Ss: 2328

Product standards

- Seamless tube and pipe: EN 10216-5
- Seamless and welded tube and pipe: ASTM A789; A790
- Flanges: ASTM A182
- Fittings: ASTM A182; (ASTM A815 applied for)
- Plate, sheet and strip: ASTM A240, EN 10088-2
- Bar steel: ASTM A479, EN 10088-3
- Forged billets: EN 10088-3

Approvals

- Approved by the American Society of Mechanical Engineers (ASME) for use in accordance with ASME Boiler and Pressure Vessel Code, Section VIII, div. 1. There is no approval for UNS S32750 in the form of plate. However, according to the ASME paragraph UG-15 it is allowed to use the design values for seamless tube according to ASME Section VIII, div. 1 also for plate
- ASME B31.3 Chemical Plant and Petroleum Refinery piping
- VdTÜV-Werkstoffblatt 508
- ISO 15156-3/NACE MR 0175 (Sulphide stress cracking resistant material for oil field equipment), (applies to liquid quenched tubes)

CHEMICAL COMPOSITION (NOMINAL) %

Chemical composition (nominal) %

C	Si	Mn	P	S	Cr	Ni	Mo
≤0.030	≤0.8	≤1.2	≤0.025	≤0.015	25	7	4

Others
N=0.3

FORMS OF SUPPLY

Seamless tube and pipe– finishes and dimensions

Seamless tube and pipe in Sandvik SAF 2507 is supplied in dimensions up to 260 mm outside diameter. The delivery condition is solution annealed and either white pickled, or bright annealed.

Other forms of supply:

- Welded tube and pipe
- Fittings and flanges
- Wire electrodes and filler wire/rods
- Covered electrodes
- Plate, sheet and wide strip
- Bar steel
- Forged products
- Cast products

MECHANICAL PROPERTIES

The following figures apply to material in the solution annealed condition. Tube and pipe with wall thickness above 20 mm (0.787 in.) may have slightly lower values. For seamless tubes with a wall thickness <4 mm we guarantee proof strength ($R_{p0.2}$) values that are 50 MPa higher than those listed below at 20°C (68°F) as well as those listed at higher temperatures. More detailed information can be supplied on request.

At 20°C (68°F)

Tube and pipe with wall thickness max. 20 mm (0.79 in.).

Metric units

Proof strength, MPa		Tensile strength, MPa	Elongation, %		Hardness, HRC
$R_{p0.2}^{a)}$	$R_{p1.0}^{a)}$	R_m	$A^{b)}$	A_2''	
≥550	≥640	800-1000	≥25	≥15	≤32

Imperial units

Proof strength, ksi		Tensile strength, ksi	Elongation, %		Hardness, HRC
$R_{p0.2}^{a)}$	$R_{p1.0}^{a)}$	R_m	$A^{b)}$	A_2''	HRC
≥80	≥93	116-145	≥25	≥15	≤32

1 MPa = 1 N/mm²

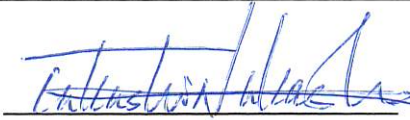
a) $R_{p0.2}$ and $R_{p1.0}$ correspond to 0.2% offset and 1.0% offset yield strength, respectively.

b) Based on $L_0 = 5.65 \sqrt{S_0}$ where L_0 is the original gauge length and S_0 the original cross-section area.

Sample data sheet of A790-S39274 (DP3W)

NIPPON STEEL & SUMITOMO METAL CORPORATION

NIPPON STEEL & SUMITOMO METAL CORPORATION

Date	January 20. 2017
Approved by	
Checked by	J. Yamamoto
Prepared by	Y. Uchida



1. **Standard:** ASTM A790-S39274
 2. **Pipe Size:** O.D. 355.6mm W.T. 30.0mm
 3. **Sample Size:** 200X200X30mm
 4. **Quantity:** 3pcs
 5. **Heat No.:** F321095
 6. **Heat Treatment:** Solution treatment (1085°C × 10min)

7. Chemical Composition (%)

	C	Si	Mn	P	S	Cu	Ni	Cr	Mo	N	W
Heat No. F321095	0.018	0.24	0.71	0.021	0.002	0.52	6.3	24.9	3.1	0.29	2.10
Spec. min.	-	-	-	-	-	0.20	6.0	24.0	2.5	0.24	1.50
max.	0.030	0.80	1.00	0.030	0.020	0.80	8.0	26.0	3.5	0.32	2.50

8. Tensile Test

	YS (N/mm ²)	TS (N/mm ²)	El (%)
Heat No. F321095	598	820	50
	583	819	47
Spec. min.	550	800	15
max.	-	-	-

Test specimen shape; Round bar type
 Gauge length; 50.8 mm

Sampling direction; Longitudinal

9. Hardness Test

	Hardness(HRC)		
Heat No. F321095	24.2	24.6	24.6
Spec. Max	32		

Sampling location: Cross section, Mid-wall

10. Charpy Impact Test

	Absorbed energy (J)			Ductile fracture area(%)		
Heat No. F321095	301	286	297	100	100	100

Test specimen shape: 10X10mm, 2mm V notch,
 Test temperature : -46°C

Sampling location: Longitudinal section



Appendix B

CPT

B.1 Weight and area measurements

The area, calculated by Equation 3.1.1, and the weight differens before and after the CPT measurements of the samples from test matrix for ASTM G48 are given in Table B.1.1. To get a greater understanding of the numbers, the CPT results from the modified version of ASTM G48 is included.

Table B.1.1: The measured CPT, the area calculated by Equation 3.1.1, and the weight loss after CPT measurements of samples according to the test matrix in Table 3.3.2.

Sample number	CPT[°C]	Area[cm ²]	Weight loss[%]
AD-1	50	9.7	0.97
AD-2	45	9.6	0.18
T2t1-1	70	11.2	1.9
T2t1-2	75	11.8	1.9
T2t2-1	65	11.8	2.0
T2t2-2	75	11.4	5.5
T2t3-1	75	11.1	2.8
T2t3-2	70	10.6	0.96
T2t4-1	<40	11.4	3.2
T2t4-2	<40	11.4	2.9
T2t5-1	<40	10.8	11.0
T2t5-2	<40	11.2	11.4
T3t1-1	75	10.6	21.1
T3t1-2	70	10.9	0.87
T3t2-1	75	11.4	10.4
T3t2-2	70	11.7	1.1
T3t3-1	75	10.9	2.9
T3t3-2	70	10.9	21.1
T3t4-1	50	11.8	3.8
T3t4-2	45	11.3	6.5
T3t5-1	<40	11.2	5.2
T3t5-2	<40	10.8	8.8
W-AD-1	80	16.8	1.6
W-AD-2	80	16.8	6.5
W-SA-1	80	14.7	2.2
W-SA-2	80	14.4	11.0
W-T1t1-1	80	16.5	15.5
W-T1t1-2	80	16.7	11.2
W-T1t2-1	80	16.6	13.1
W-T1t2-2	80	16.8	13.0
W-T1t3-1	75	16.7	0.84
W-T1t3-2	75	16.9	1.3
W-T1t4-1	65	14.6	3.9
W-T1t4-2	65	14.7	6.1
W-T1t5-1	<40	16.2	3.1
W-T1t5-2	<40	16.8	1.3

B.2 Electrochemical measurements

Some of the results of the CPT measurements for the samples from the test matrix in Table 3.3.2 for the modified version of ASTM G48 are shown in Figure B.2.1a to B.2.2a. The rest are presented in Chapter 3.3.1, and a summary of the results are given in Table 4.1.1.

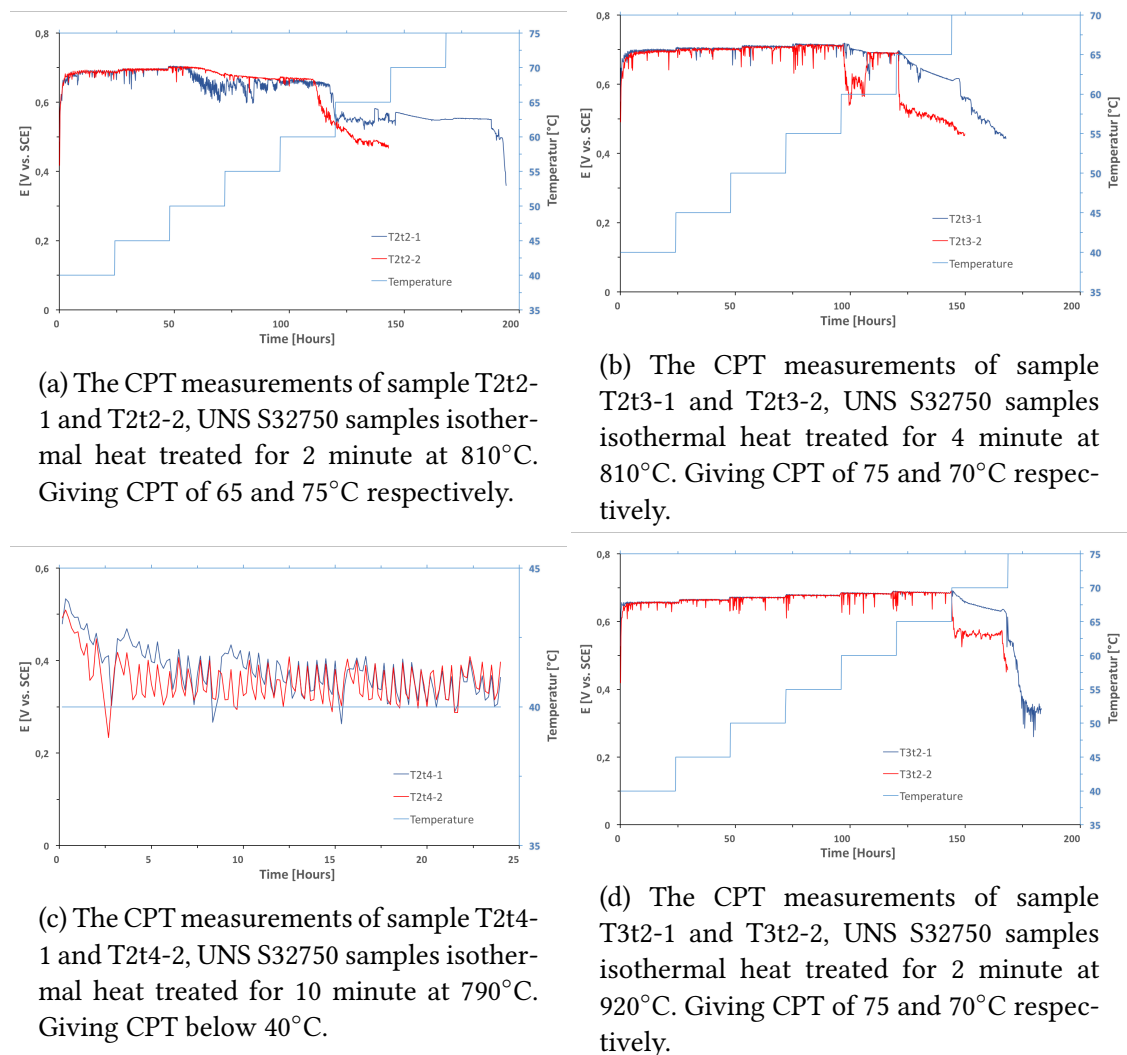
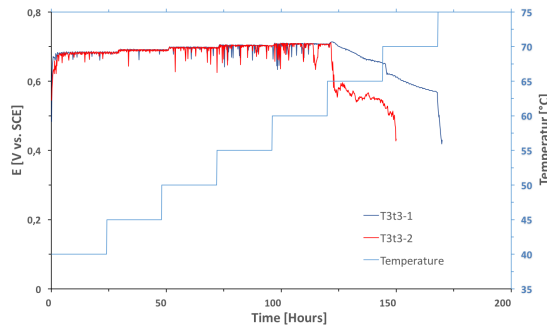
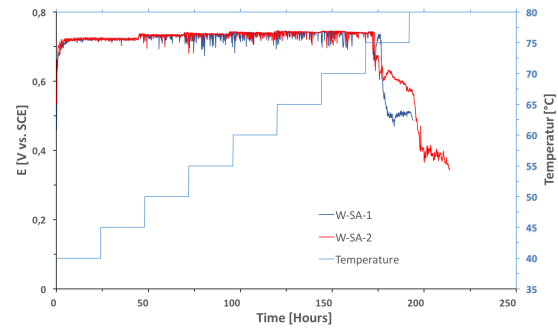


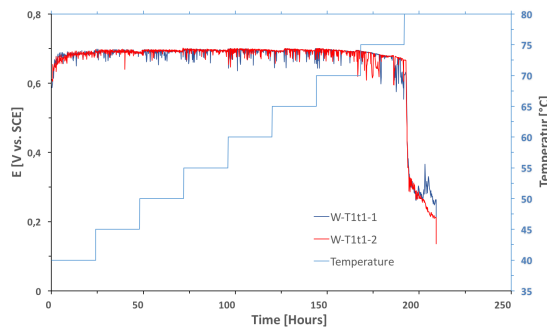
Figure B.2.1: The CPT measurements of samples from the test matrix in Table 3.3.2.



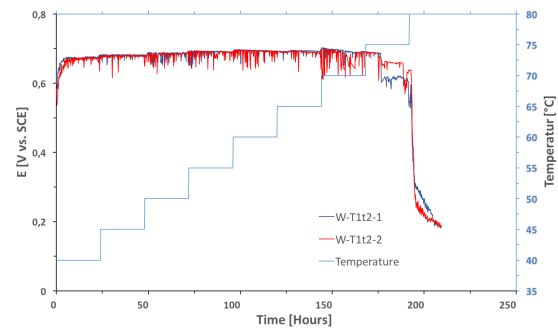
(a) The CPT measurements of sample T3t3-1 and T3t3-2, UNS S32750 samples isothermal heat treated for 4 minute at 920°C. Giving CPT of 75 and 70°C respectively.



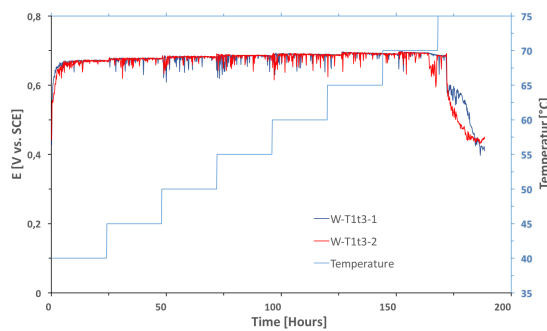
(b) The CPT measurements of sample W-SA-1 and W-SA-2, UNS S39274 samples that only are solution annealed. Giving CPT of 80°C.



(c) The CPT measurements of sample W-T1t1-1 and W-T1t1-2, UNS S39274 samples isothermal heat treated for 1 minute at 846°C. Giving CPT of 80°C.



(d) The CPT measurements of sample W-T1t2-1 and W-T1t2-2, UNS S39274 samples isothermal heat treated for 1.5 minutes at 846°C. Giving CPT of 80°C.



(e) The CPT measurements of sample W-T1t3-1 and W-T1t3-2, UNS S39274 samples isothermal heat treated for 2 minutes at 846°C. Giving CPT of 75°C.

Figure B.2.2: The CPT measurements of samples from the test matrix in Table 3.3.2.

B.3 Previous work

This thesis is a part of a bigger project that focus on the affect on tungsten and isothermal heat treatments on the corrosion resistance of three SDSS grade, W-free UNS S32750, UNS S32760 with a W content of 0.62 wt%, and UNS S39274 with a W content of 2.1 wt%. To get a greater understanding of the corrosion properties of the three SDSS grades, another master student have focused on the surface characterization prior to electrochemical measurements[72]. Another master student have tested the corrosion properties of UNS S32760 by the modified version of ASTM G48 and ASTM G61[75].

B.3.1 Microstructure characterization

All microstructure characterization prior to electrochemical measurements was performed by Mia Bernås[72].

Quantitative analysis of α - and γ -phase in UNS S32750, UNS S32760, and UNS S39274 in its as-delivered condition and after solution annealing by Solution DT image analysis software on light optical micrographs, and EBSD. The measured volume fraction is given in Figure B.3.3[72].

Table B.3.1: The volume fraction of α - and γ -phase in UNS S32750, UNS S32760, and UNS S39274 in its as-delivered condition and after solution annealing[72].

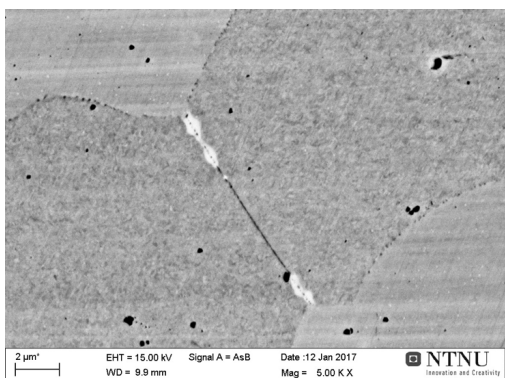
	Phase	UNS S32750	UNS S32760	UNS S39274
As-delivered	α	58.5	56.5	42.0
	γ	41.5	43.5	58.0
Solution annealed	α	57.2	62.9	47.6
	γ	42.8	37.1	52.4

The chemical composition of α - and γ -phase in the as-delivered and solution annealed condition, determined by another student using EDS detector coupled to the SEM[72]. Thus, the effect of solution annealing on the chemical composition can be seen. For UNS S39274, there was only performed qualitative analysis after 1 minute of isothermal heat treatment at 846°C, not the as-delivered and solution-annealed condition.

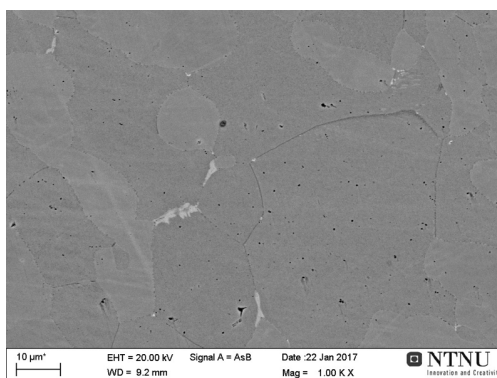
Table B.3.2: The chemical composition of α - and γ -phase in the as-delivered and solution annealed condition for UNS S32750 and UNS S32760, and after aging at 846°C for 1 minute for UNS S39274. Only major alloying elements included[72].

		Phase	Fe	Cr	Ni	Mo	W
UNS S32750	As-delivered	Ferrite (α)	63.5	28.8	4.5	3.7	
		Austenite (γ)	64.7	25.6	7.5	2.2	
	Solution annealed	Ferrite (α)	63.5	27.3	4.9	3.7	
		Austenite (γ)	64.8	25.3	7.4	2.5	
UNS S32760	As-delivered	Ferrite (α)	62.5	27.9	5.4	3.3	0.82
		Austenite (γ)	63.9	24.8	8.3	2.2	0.66
	Solution annealed	Ferrite (α)	62.2	27.9	5.4	3.3	0.89
		Austenite (γ)	63.7	24.6	8.3	2.1	0.84
UNS S39274	W-T1t1	Ferrite (α)	63.5	26.4	4.7	2.9	2.5
		Austenite (γ)	64.7	24.1	7.3	1.9	1.9

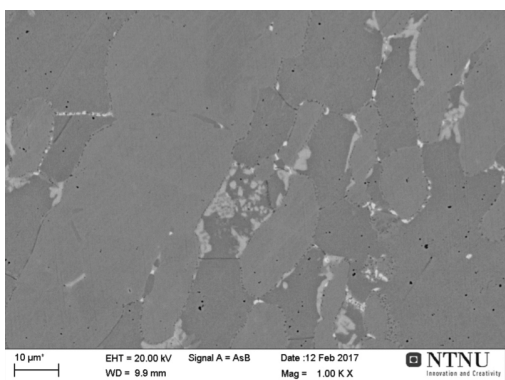
SEM-BSE micrographs of the samples prior to electrochemical measurements, were performed by Bernås[72] to evaluate the microstructural evolution. This can be seen in Figure B.3.1 to B.3.4.



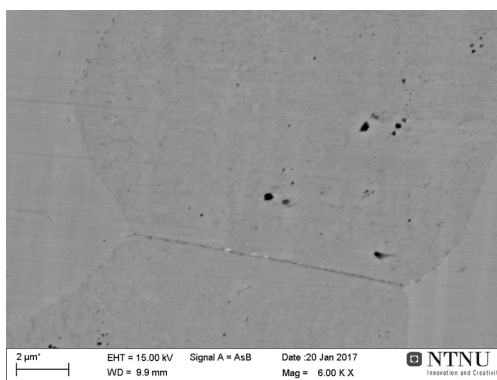
(a) UNS S32750 aged for 2 minutes at 846°C.



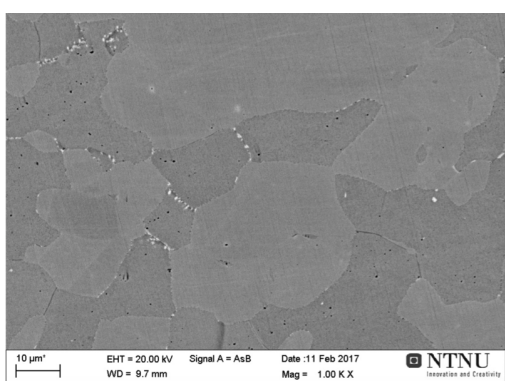
(b) UNS S32750 aged for 4 minutes at 846°C.



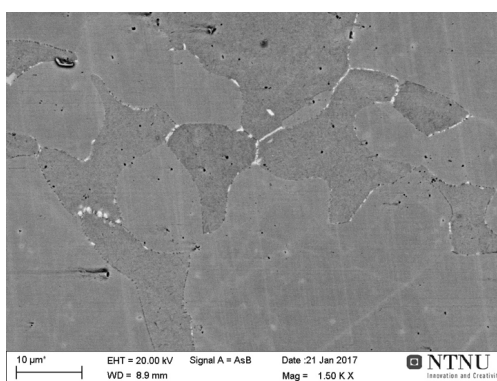
(c) UNS S32750 aged for 10 minutes at 846°C.



(d) UNS S32750 aged for 2 minutes at 790°C.

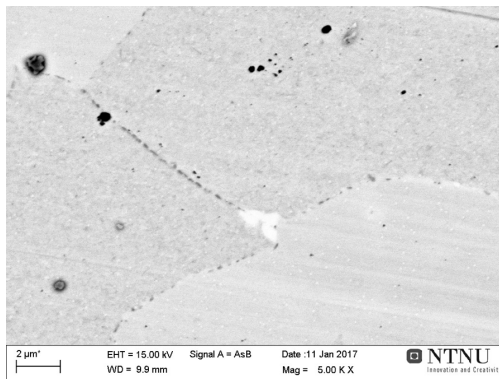


(e) UNS S32750 aged for 10 minutes at 790°C.

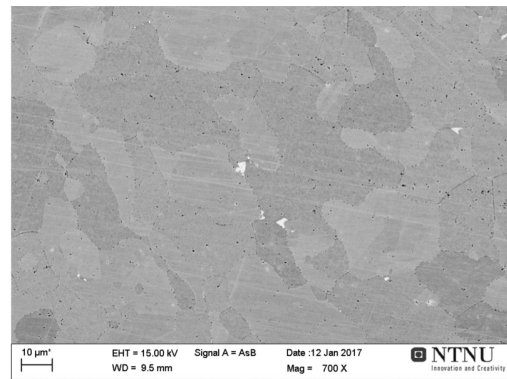


(f) UNS S32750 aged for 20 minutes at 790°C.

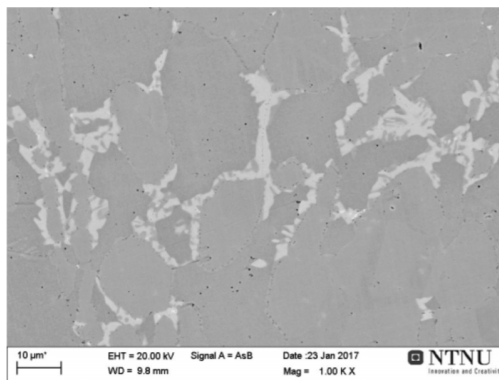
Figure B.3.1: Microstructural evolution of selected samples from UNS S32750[72].



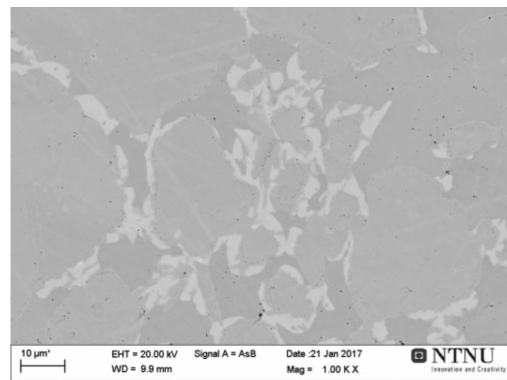
(a) UNS S32750 aged for 2 minutes at 920°C.



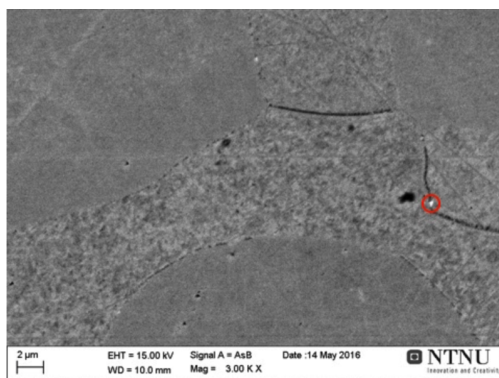
(b) UNS S32750 aged for 4 minutes at 920°C.



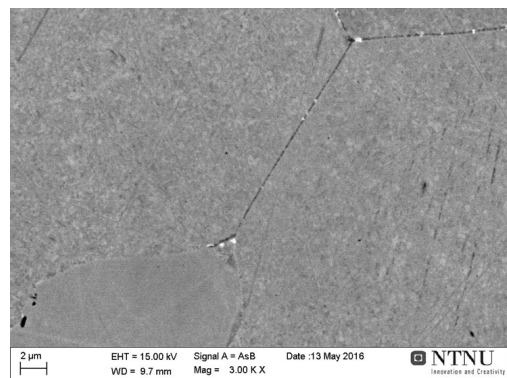
(c) UNS S32750 aged for 10 minutes at 920°C.



(d) UNS S32750 aged for 20 minutes at 920°C.

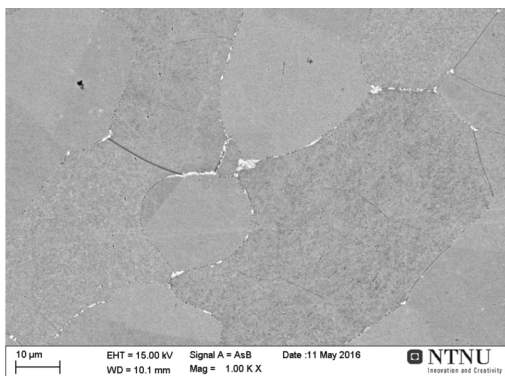


(e) UNS S32760 aged for 1.5 minutes at 846°C.

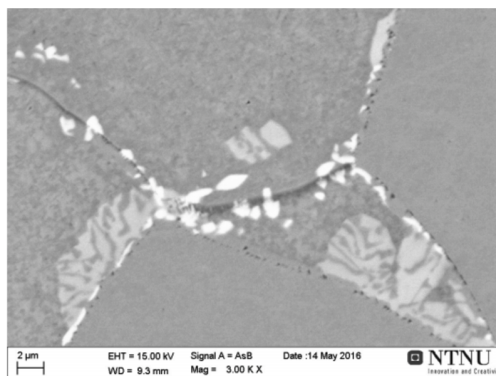


(f) UNS S32760 aged for 2 minutes at 846°C.

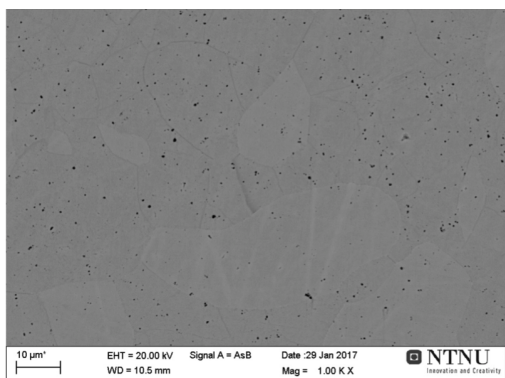
Figure B.3.2: Microstructural evolution of selected samples from UNS S32750 and UNS S32760[72].



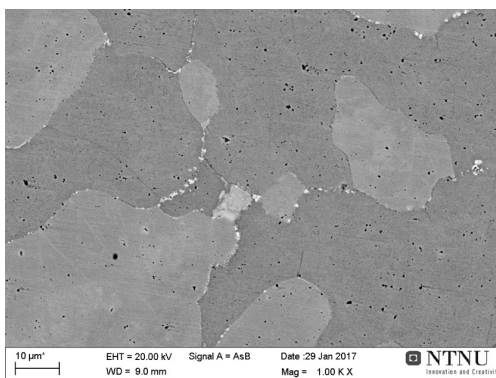
(a) UNS S32760 aged for 4 minutes at 846°C.



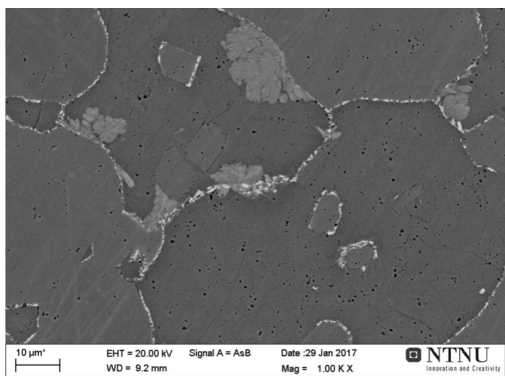
(b) UNS S32760 aged for 10 minutes at 846°C.



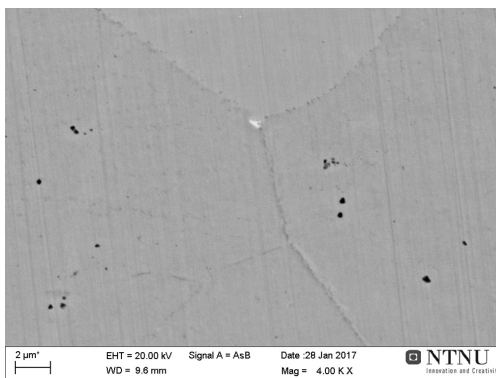
(c) UNS S32760 aged for 4 minutes at 790°C.



(d) UNS S32760 aged for 10 minutes at 790°C.

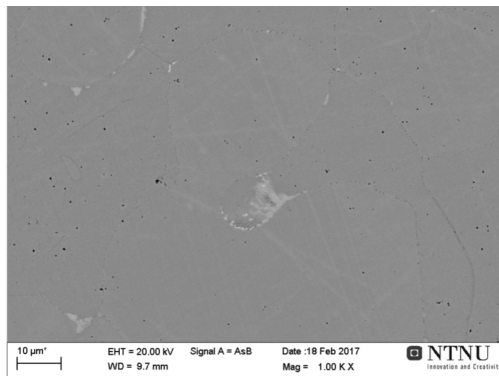


(e) UNS S32760 aged for 20 minutes at 790°C.

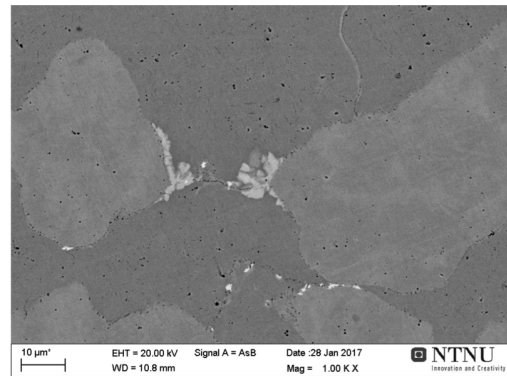


(f) UNS S32760 aged for 1 minute at 920°C.

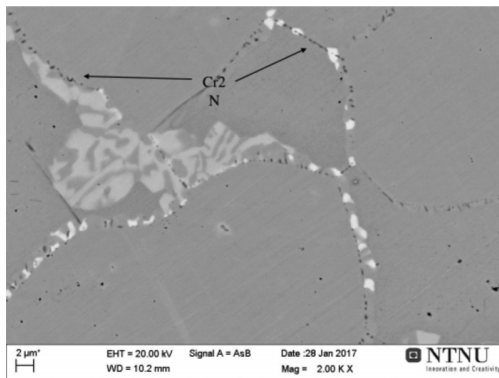
Figure B.3.3: Microstructural evolution of selected samples from UNS S32760[72].



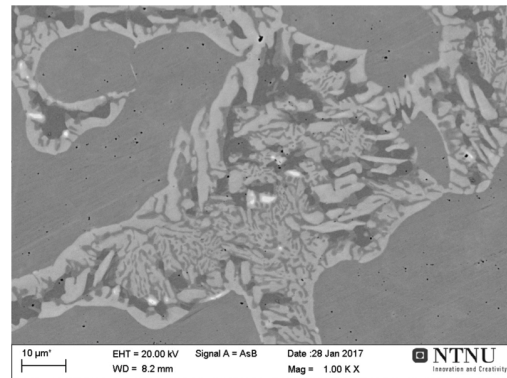
(a) UNS S32760 aged for 2 minutes at 920°C.



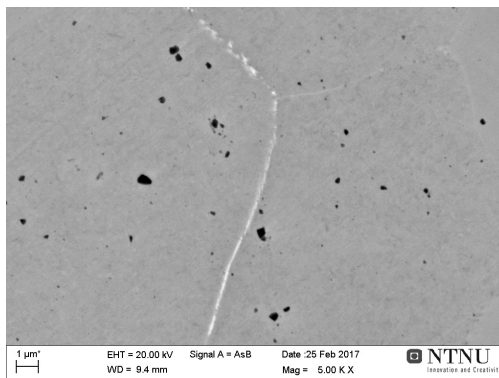
(b) UNS S32760 aged for 4 minutes at 920°C.



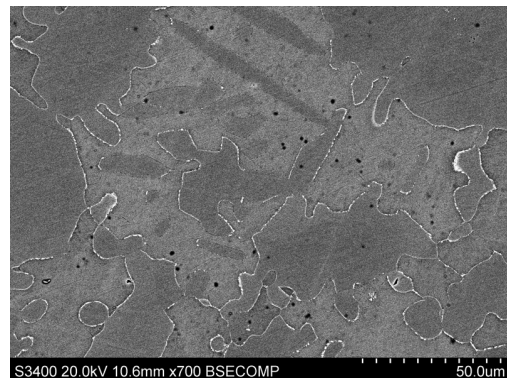
(c) UNS S32760 aged for 10 minutes at 920°C.



(d) UNS S32760 aged for 20 minutes at 920°C.



(e) UNS S39274 aged for 4 minutes at 846°C.



(f) UNS S39274 aged for 10 minute at 846°C.

Figure B.3.4: Microstructural evolution of selected samples from UNS S32760 and UNS S39274[72].

The volume fraction of intermetallic phases measured for UNS S32750, UNS S32760, and UNS 39274[72], can be found in Table B.3.3

Table B.3.3: The volume fraction of intermetallic phases measured for UNS S32750, UNS S32760, and UNS S39274[72].

			Time [min]					
			IHT	Phase	1	1.5	2	4
UNS S32750	846°C	σ	0	0	0.04	0.3	3.8	
		χ	0	0	0.03	0	0.3	
		Sum ^a	0	0	0.04	0	0	
	790°C	σ	0		0	0	0.2	3.9
		χ	0		0	0	0.1	0.4
	920°C	σ	0		0.05	0.2	3.1	9.3
		χ	0		0	0.1	0.03	0.1
		Sum ^a	0		0.06	0	0	0
	UNS S32760	846°C	σ	0	0	0.05	0.2	2.7
χ			0	0	0.006	0.2	0.2	
Sum ^a			0	0.006	0.007	0	0	
790°C		σ	0		0	0	0.9	4.3
		χ	0		0	0	0.4	0.8
920°C		σ	0.03		0.3	0.3	5.1	30.2
	χ	0.03		0.05	0.05	0.3	0.2	
UNS S39274	846°C	σ	0	0	0	0	0.3	
		χ	0	0	0	0	1.4	
		Sum ^a	0	0	0	0.04	0	

^a When unable to distinguish between the mention phases, the amount found was assumed to be a sum of σ - and χ -phase.

B.3.2 CPT

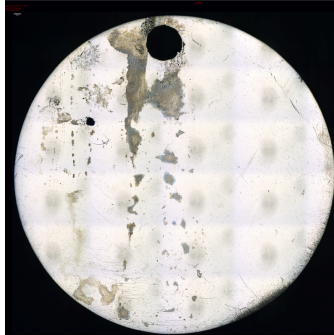
CPT values obtained with OCP measurements in 6 wt% ferric chloride solution from previous work on low-W UNS S32760 are listed in Table B.3.4[75]. They are presented together with the results from the T1 isothermal heat treatment on UNS S32750 performed in the project work[73]. To better understand these results and the effect of tungsten and isothermal heat treatments, they are presented together with the results obtained at this work. All of the samples had about the same area, machining, heat treatment and surface finish. To get a greater understanding of the affect the microstructure has on the corrosion resistance, the intermetallic precipitations and secondary phases detected during surface characterizations prior to corrosion testing on the different isothermal heat treatments are included in the table.

Table B.3.4: CPT of UNS S32750, UNS S32760 and UNS S39274 as a function of heat treatment with detected secondary phases in parenthesis. The results of UNS S32760 and of the T1 isothermal heat treatment of UNS S32750 are from previous work[75, 73].

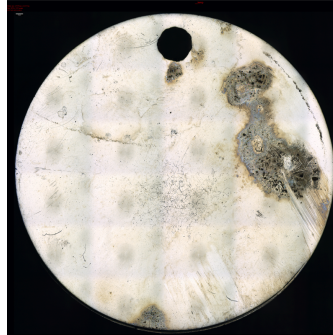
Heat treatment	CPT [°C]					
	UNS S32750		UNS S32760		UNS S39274	
AD	50	(-)			80	(-)
AD	45	(-)			80	(-)
SA	80	(-)	80	(-)	80	(-)
SA	80	(-)	75	(-)	80	(-)
T1t1	65	(-)	70	(-)	80	(-)
T1t1	65	(-)	70	(-)	80	(-)
T1t2	70	(-)	70	(χ)	80	(-)
T1t2	75	(-)	75	(χ)	80	(-)
T1t3	70	(σ, χ)	65	(σ, χ)	75	(-)
T1t3	70	(σ, χ)	65	(σ, χ)	75	(-)
T1t4	50	(σ, χ)	45	(σ, χ)	65	(σ, χ)
T1t4	50	(σ, χ)	45	(σ, χ)	65	(σ, χ)
T1t5					<40	(σ, χ)
T1t5					<40	(σ, χ)
T2t1	70	(-)	65	(-)		
T2t1	75	(-)	65	(-)		
T2t2	65	(-)	65	(-)		
T2t2	75	(-)	65	(-)		
T2t3	75	(σ, χ)	55	(-)		
T2t3	70	(σ, χ)	55	(-)		
T2t4	<40	(σ, χ)				
T2t4	<40	(σ, χ)				
T2t5	<40	(σ, χ)	<40	(σ, χ)		
T2t5	<40	(σ, χ)	<40	(σ, χ)		
T3t1	75	(-)	70	($\sigma, \text{Cr}_2\text{N}, \chi$)		
T3t1	70	(-)	70	($\sigma, \text{Cr}_2\text{N}, \chi$)		
T3t2	75	($\sigma, \text{Cr}_2\text{N}, \chi$)	70	($\sigma, \text{Cr}_2\text{N}, \chi$)		
T3t2	70	($\sigma, \text{Cr}_2\text{N}, \chi$)	70	($\sigma, \text{Cr}_2\text{N}, \chi$)		
T3t3	75	($\sigma, \text{Cr}_2\text{N}, \chi$)	65	($\sigma, \text{Cr}_2\text{N}, \chi$)		
T3t3	70	($\sigma, \text{Cr}_2\text{N}, \chi$)	60	($\sigma, \text{Cr}_2\text{N}, \chi$)		
T3t4	50	($\sigma, \text{Cr}_2\text{N}, \chi$)				
T3t4	45	($\sigma, \text{Cr}_2\text{N}, \chi$)				
T3t5	<40	($\sigma, \text{Cr}_2\text{N}, \chi, \gamma_2$)	<40	($\sigma, \text{Cr}_2\text{N}, \chi, \gamma_2$)		
T3t5	<40	($\sigma, \text{Cr}_2\text{N}, \chi, \gamma_2$)	<40	($\sigma, \text{Cr}_2\text{N}, \chi, \gamma_2$)		

B.4 Surface characterization

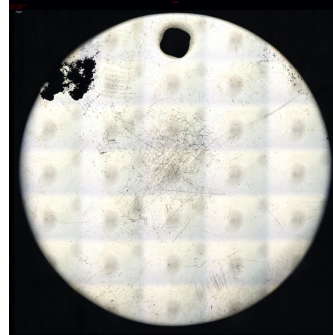
Figure B.4.1, B.4.2, and B.4.3 show surface characterizations after CPT measurements by OM with a magnification of 2.5X. The rest of the surface characterizations are found in Figure 4.1.7 and 4.1.8.



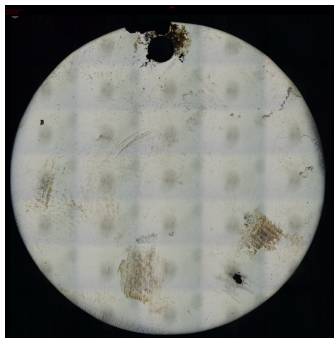
(a) Sample AD-1 with a CPT of 50°C.



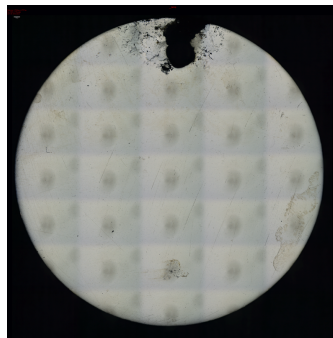
(b) Sample AD-2 with a CPT of 45°C.



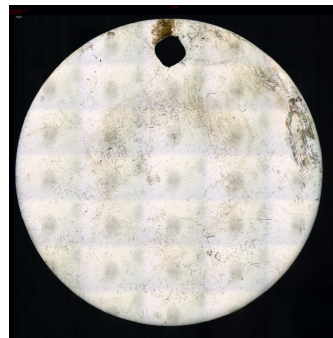
(c) Sample T2t1-2 with a CPT of 75°C.



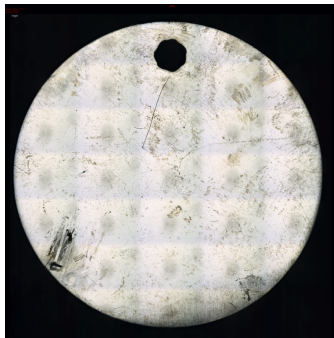
(d) Sample T2t2-1 with a CPT of 65°C.



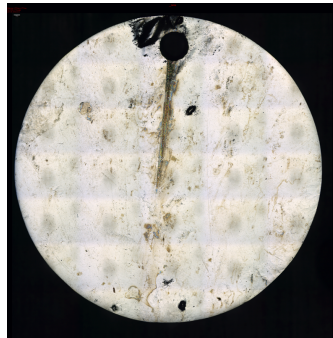
(e) Sample T2t2-2 with a CPT of 75°C.



(f) Sample T2t3-2 with a CPT of 70°C.



(g) Sample T2t4-2 with a CPT below 40°C.



(h) Sample T2t5-1 with a CPT below 40°C.



(i) Sample T2t5-2 with a CPT below 40°C.

Figure B.4.1: Surface characterization by OM with a magnification of 2.5X of selected samples after CPT measurements.

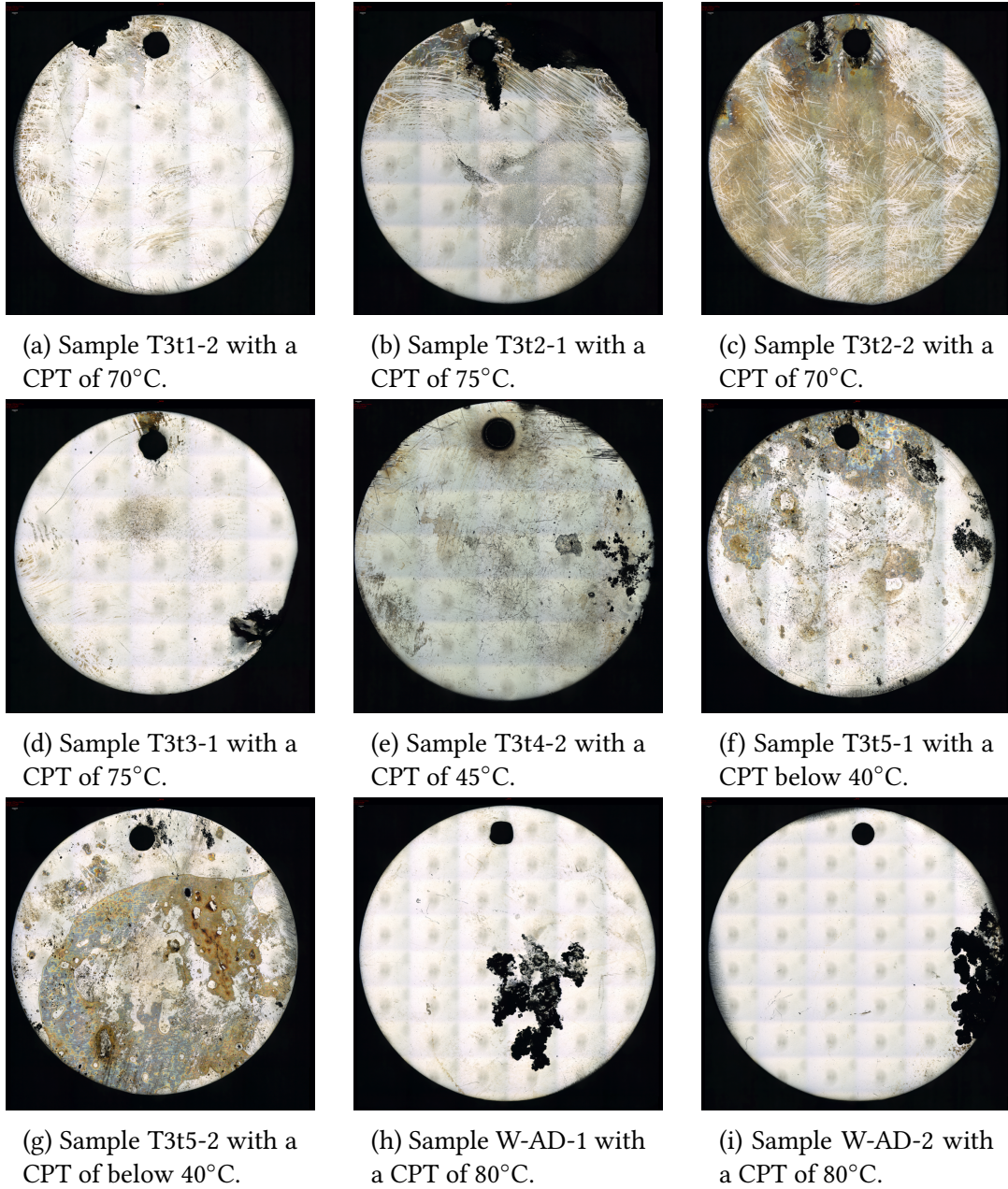
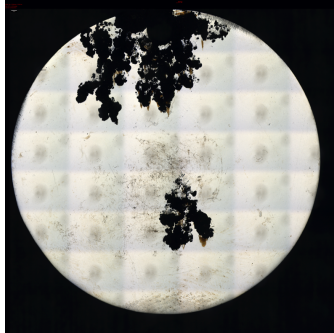
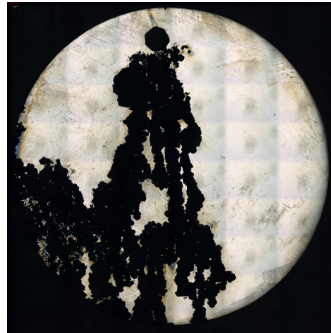


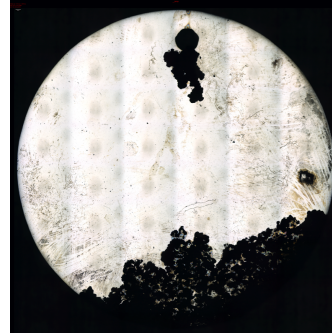
Figure B.4.2: Surface characterization by OM with a magnification of 2.5X of selected samples after CPT measurements.



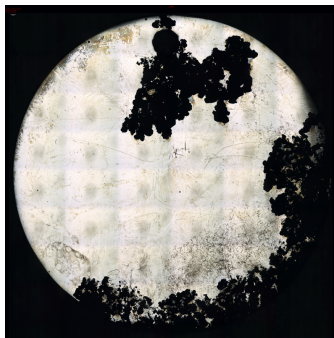
(a) Sample W-SA-2 with a CPT of 80°C.



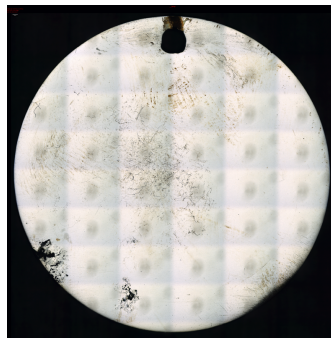
(b) Sample W-T1t1-2 with a CPT of 80°C.



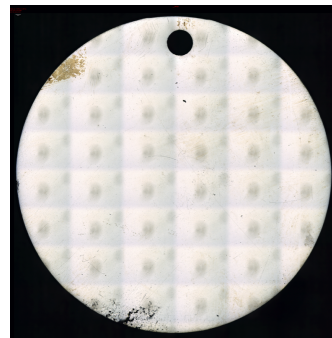
(c) Sample W-T1t2-1 with a CPT of 80°C.



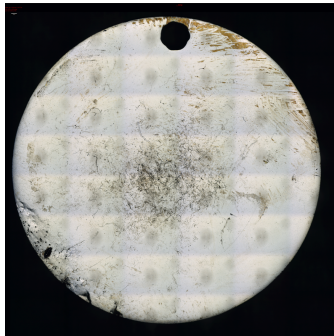
(d) Sample W-T1t2-2 with a CPT of 80°C.



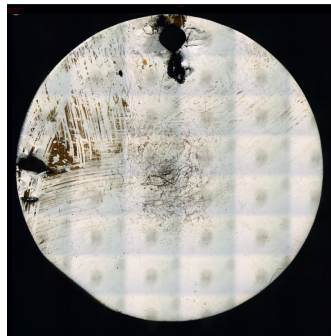
(e) Sample W-T1t3-1 with a CPT of 75°C.



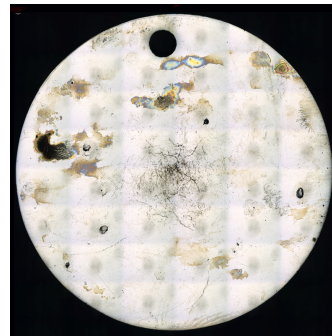
(f) Sample W-T1t3-2 with a CPT of 75°C.



(g) Sample W-T1t4-1 with a CPT of 65°C.



(h) Sample W-T1t4-2 with a CPT of 65°C.



(i) Sample W-T1t5-2 with a CPT below 40°C.

Figure B.4.3: Surface characterization by OM with a magnification of 2.5X of selected samples after CPT measurements.

Appendix C

Anodic CPP

C.1 Electrochemical measurements

Figure C.1.1 to C.1.6 show some of the anodic CPP curves obtained with an electrolyte temperature of 40°C, while Figure C.1.7 to C.1.12 show some of the anodic CPP curves obtained with an electrolyte temperature of 60°C, and Figure C.1.13 to C.1.18 show some of the anodic CPP curves obtained with an electrolyte temperature of 80°C. The rest of the results are found in Appendix 4.2.

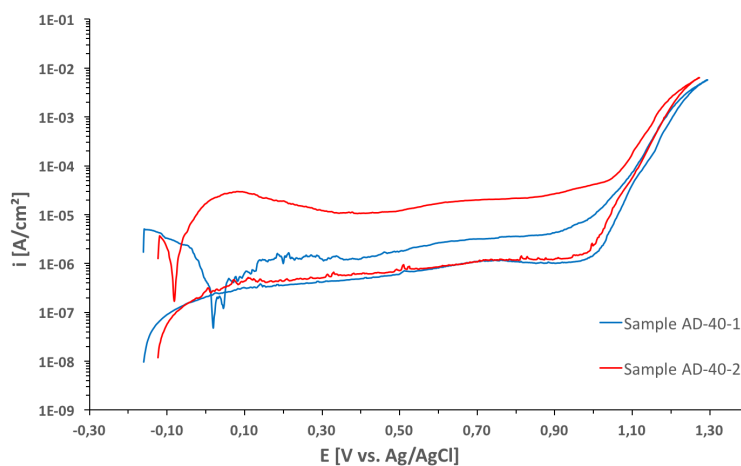


Figure C.1.1: The anodic CPP curves for sample AD-40-1 and AD-40-2, UNS S32750 as delivered samples that have not been heat treated. The curves were recorded with an electrolyte temperature of 40°C.

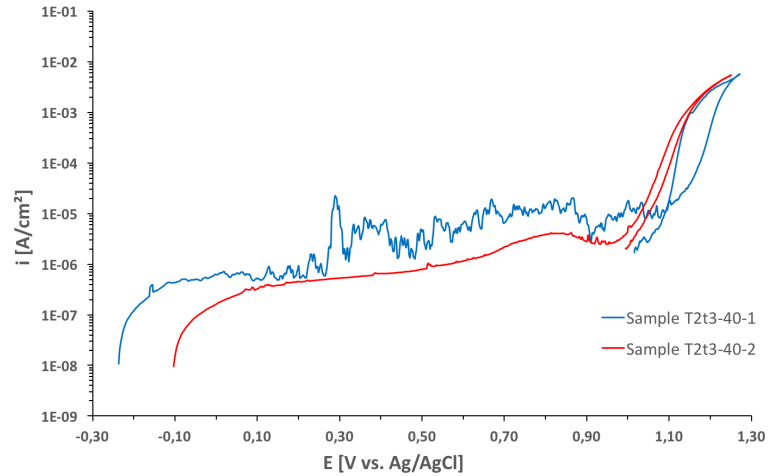


Figure C.1.2: The anodic CPP curves for sample T2t3-40-1 and T2t3-40-2, UNS S32750 samples isothermal heat treated for 4 minutes at 810°C. The curves were recorded with an electrolyte temperature of 40°C.

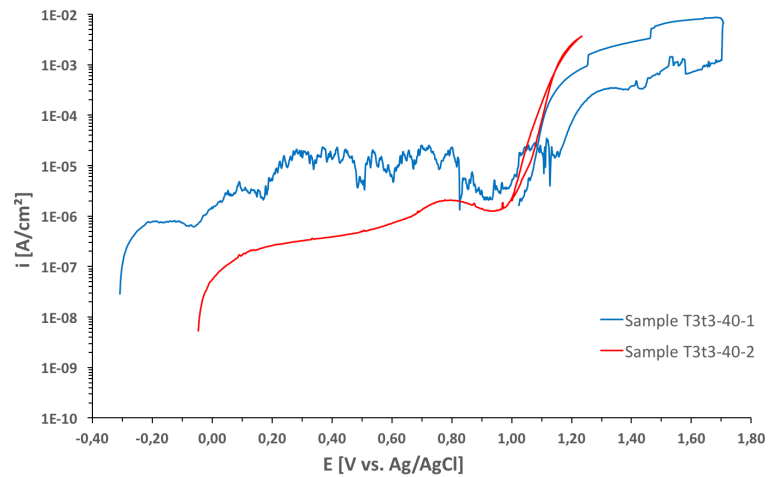


Figure C.1.3: The anodic CPP curves for sample T3t3-40-1 and T3t3-40-2, UNS S32750 samples isothermal heat treated for 4 minutes at 920°C. The curves were recorded with an electrolyte temperature of 40°C.

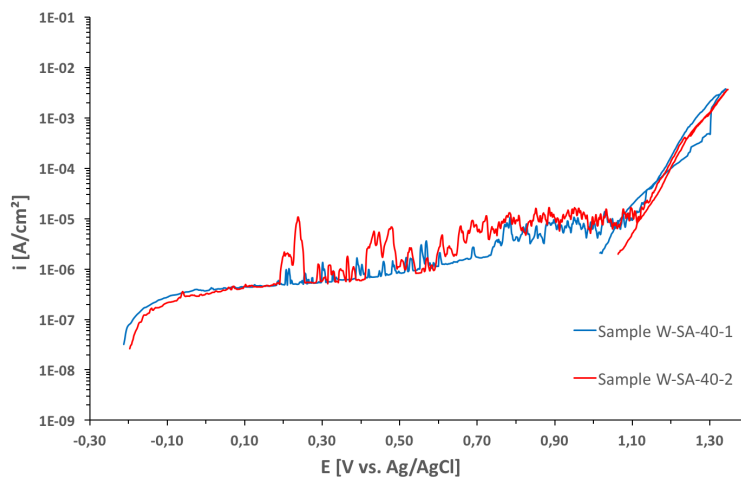


Figure C.1.4: The anodic CPP curves for sample W-SA-40-1 and W-SA-40-2, UNS S39274 samples that have only been solution annealed and not isothermal heat treated. The curves were recorded with an electrolyte temperature of 40°C.

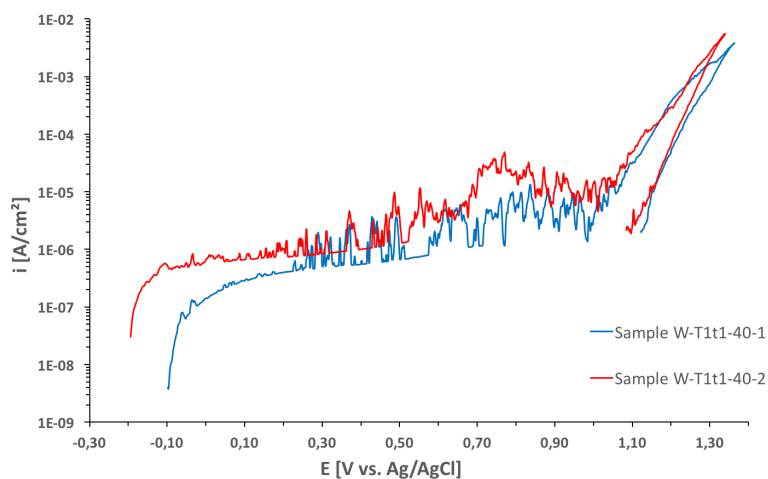


Figure C.1.5: The anodic CPP curves for sample W-T1t1-40-1 and W-T1t1-40-2, UNS S39274 samples isothermal heat treated for 1 minute at 870°C. The curves were recorded with an electrolyte temperature of 40°C.

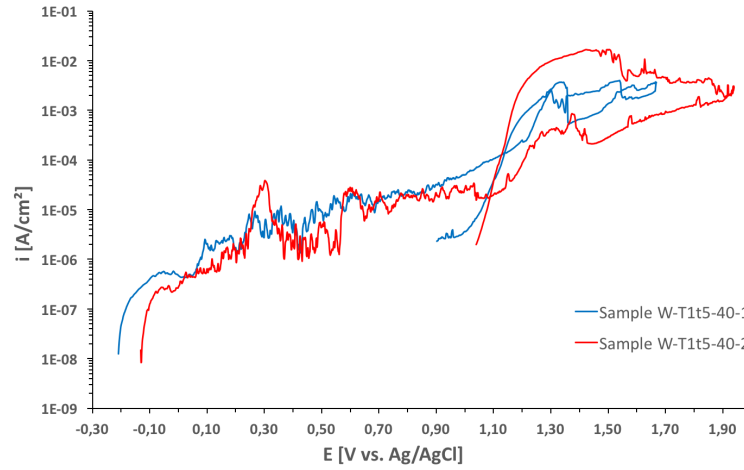


Figure C.1.6: The anodic CPP curves for sample W-T1t5-40-1 and W-T1t5-40-2, UNS S39274 samples isothermal heat treated for 10 minute at 870°C. The curves were recorded with an electrolyte temperature of 40°C.

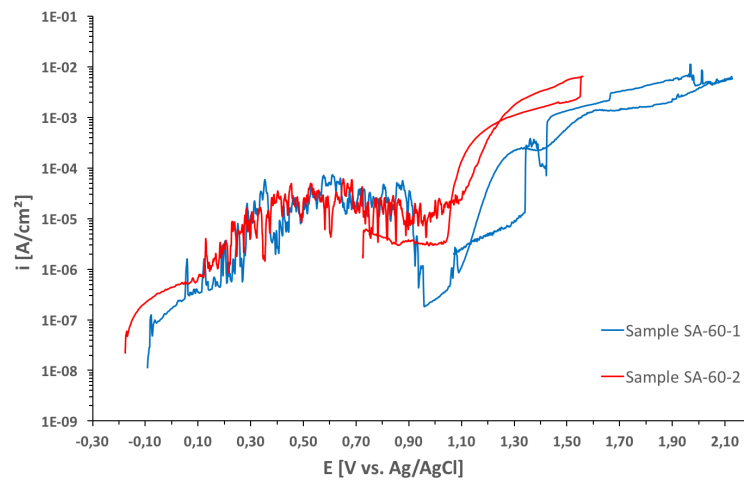


Figure C.1.7: The anodic CPP curves for sample SA-60-1 and SA-60-2, UNS S32750 samples that only have been solution annealed and not isothermal heat treated. The curves were recorded with an electrolyte temperature of 60°C.

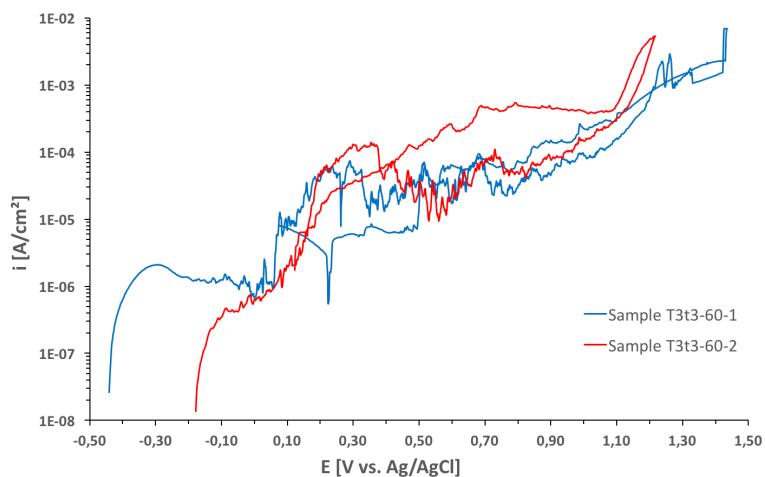


Figure C.1.8: The anodic CPP curves for sample T3t3-60-1 and T3t3-60-2, UNS S32750 samples isothermal heat treated for 4 minutes at 920°C. The curves were recorded with an electrolyte temperature of 60°C.

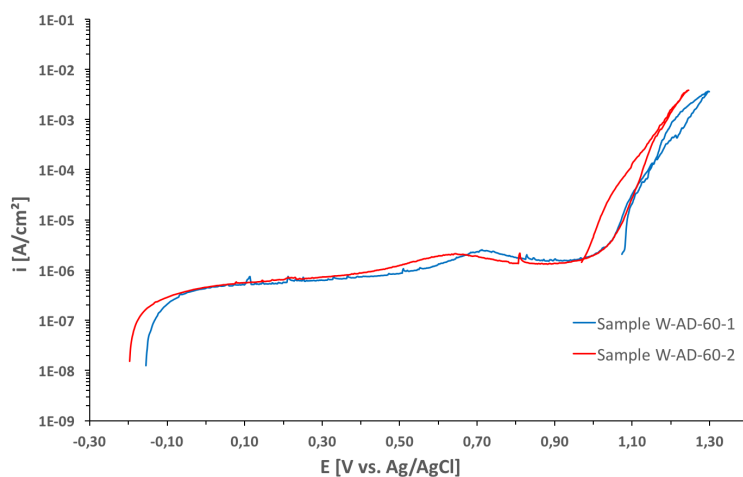


Figure C.1.9: The anodic CPP curves for sample W-AD-60-1 and W-AD-60-2, UNS S39274 as delivered samples that have not been heat treated. The curves were recorded with an electrolyte temperature of 60°C.

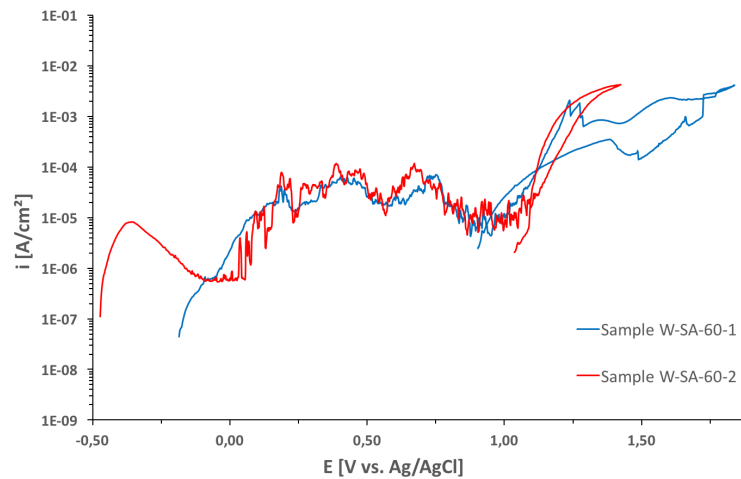


Figure C.1.10: The anodic CPP curves for sample W-SA-60-1 and W-SA-60-2, UNS S39274 samples that only have been solution annealed and not isothermal heat treated. The curves were recorded with an electrolyte temperature of 60°C.

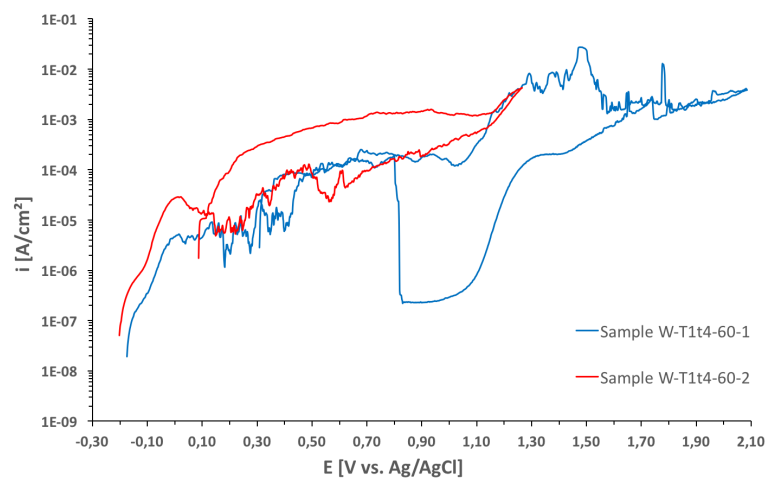


Figure C.1.11: The anodic CPP curves for sample W-T1t4-60-1 and W-T1t4-60-2, UNS S39274 samples isothermal heat treated for 4 minutes at 870°C. The curves were recorded with an electrolyte temperature of 60°C.

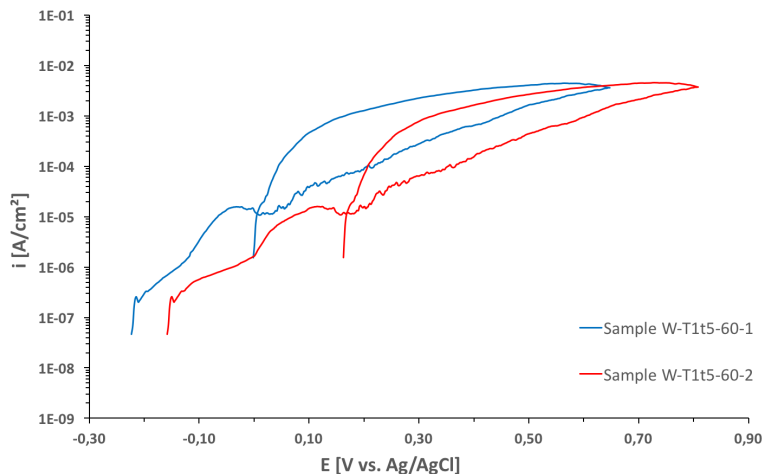


Figure C.1.12: The anodic CPP curves for sample W-T1t5-60-1 and W-T1t5-60-2, UNS S39274 samples isothermal heat treated for 10 minutes at 870°C. The curves were recorded with an electrolyte temperature of 60°C.

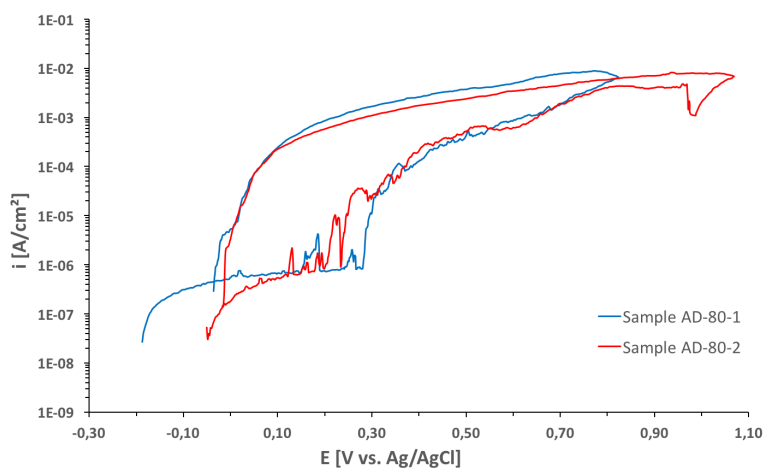


Figure C.1.13: The anodic CPP curves for sample AD-80-1 and AD-80-2, UNS S32750 as delivered samples that have not been heat treated. The curves were recorded with an electrolyte temperature of 80°C.

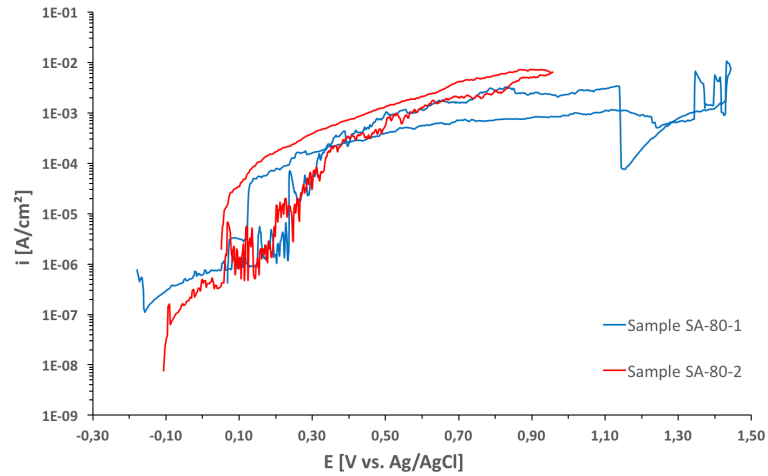


Figure C.1.14: The anodic CPP curves for sample SA-80-1 and SA-80-2, UNS S32750 samples that only have been solution annealed and not isothermal heat treated. The curves were recorded with an electrolyte temperature of 80°C.

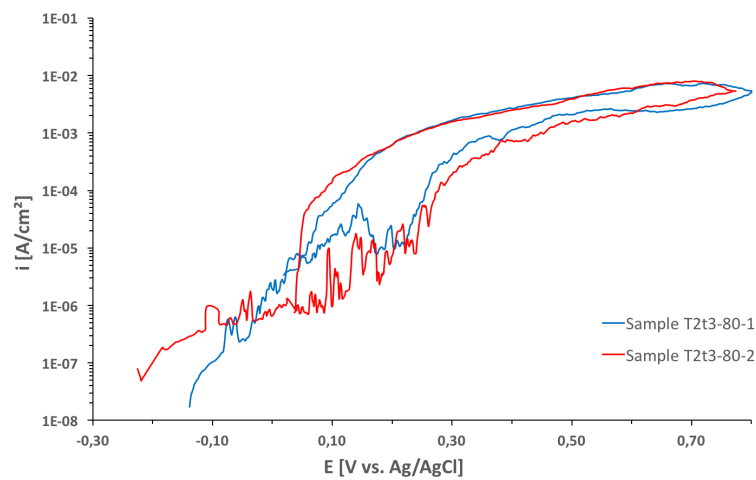


Figure C.1.15: The anodic CPP curves for sample T2t3-80-1 and T2t3-80-2, UNS S32750 samples isothermal heat treated for 4 minutes at 810°C. The curves were recorded with an electrolyte temperature of 80°C.

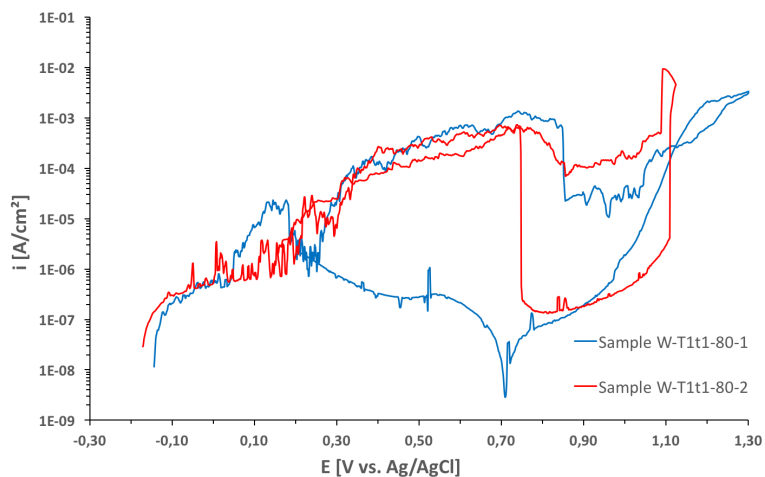


Figure C.1.16: The anodic CPP curves for sample W-T1t1-80-1 and W-T1t1-80-2, UNS S39274 samples isothermal heat treated for 1 minute at 870°C . The curves were recorded with an electrolyte temperature of 80°C .

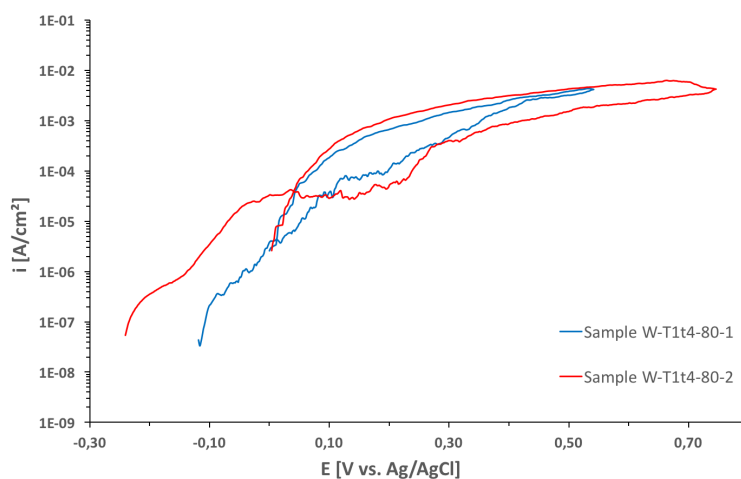


Figure C.1.17: The anodic CPP curves for sample W-T1t4-80-1 and W-T1t4-80-2, UNS S39274 samples isothermal heat treated for 4 minutes at 870°C . The curves were recorded with an electrolyte temperature of 80°C .

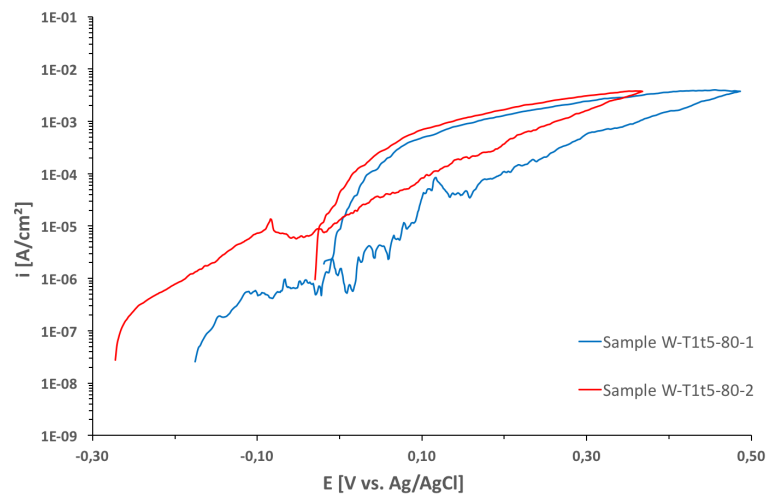
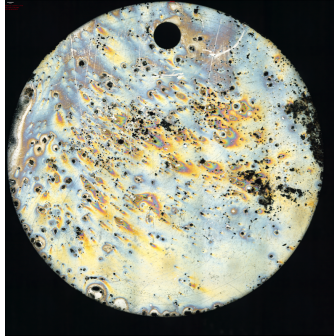


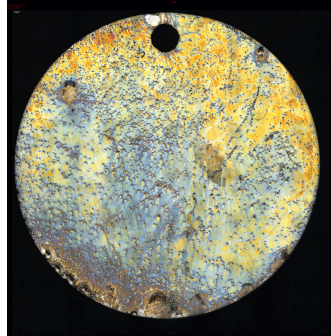
Figure C.1.18: The anodic CPP curves for sample W-T1t5-80-1 and W-T1t5-80-2, UNS S39274 samples isothermal heat treated for 10 minute at 870°C. The curves were recorded with an electrolyte temperature of 80°C.

C.2 Surface characterization

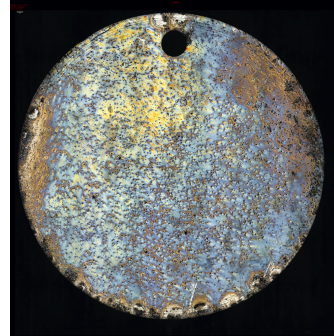
Figure C.2.1, C.2.2, and C.2.3 show surface characterizations after anodic CPP measurements by OM with a magnification of 2.5X. The rest of the surface characterizations are found in Figure 4.2.10, 4.2.11, and 4.2.12.



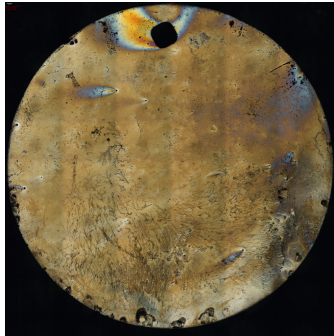
(a) Sample AD-40-1 after recording with an electrolyte temperature of 40°C.



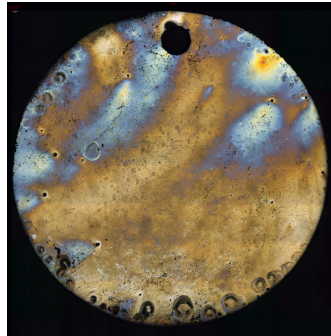
(b) Sample T2t3-40-2 after recording with an electrolyte temperature of 40°C.



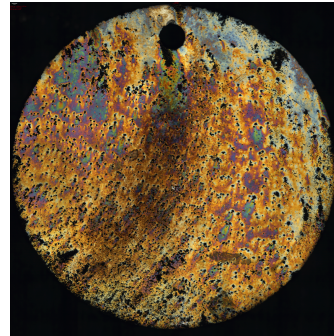
(c) Sample T3t3-40-2 after recording with an electrolyte temperature of 40°C.



(d) Sample W-SA-40-1 after recording with an electrolyte temperature of 40°C.



(e) Sample W-T1t1-40-1 after recording with an electrolyte temperature of 40°C.



(f) Sample W-T1t5-40-2 after recording with an electrolyte temperature of 40°C.

Figure C.2.1: Surface characterization by OM with a magnification of 2.5X of selected samples after electrochemical measurements according to ASTM G61 with an electrolyte temperature of 40°C.

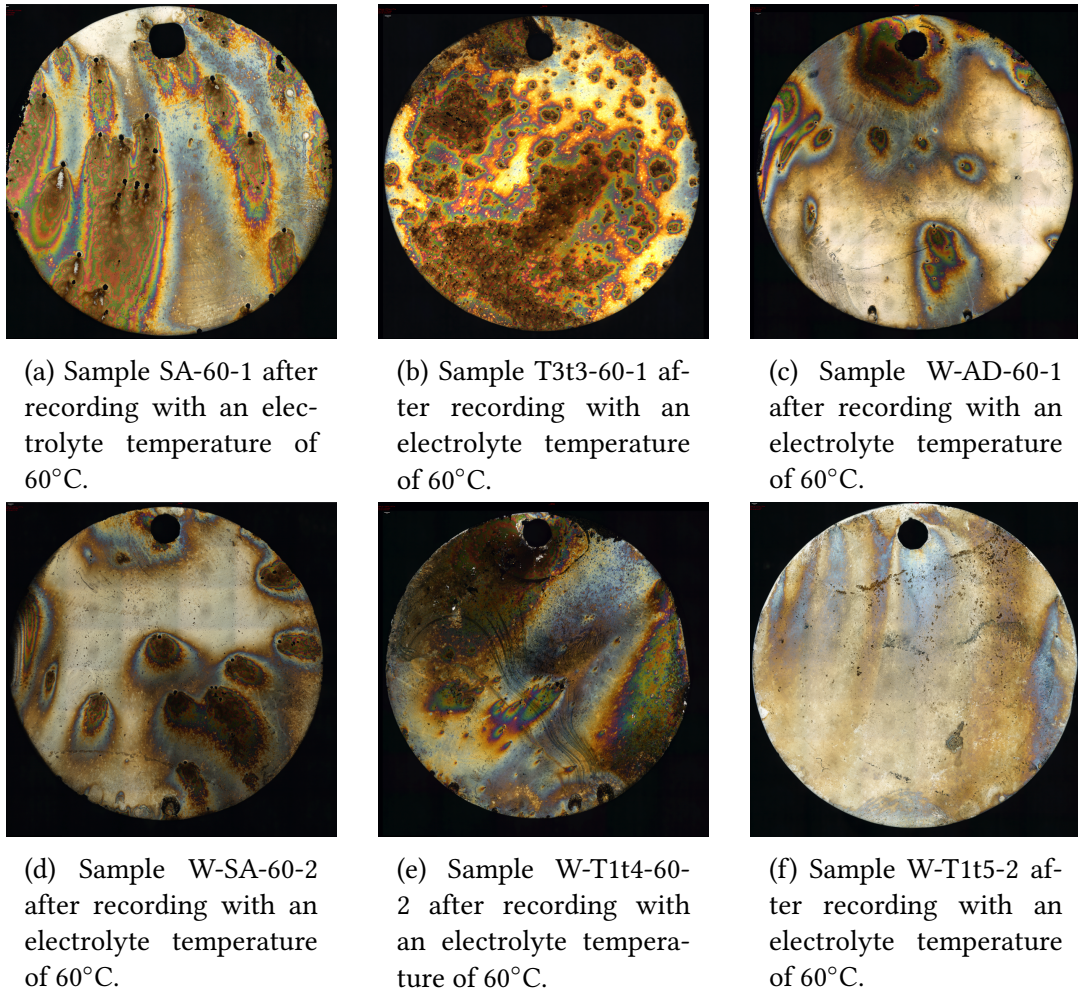
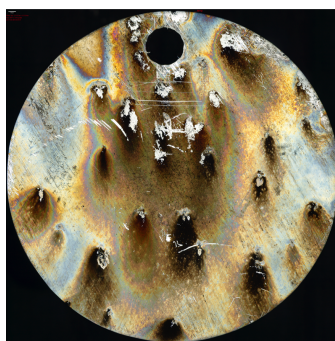
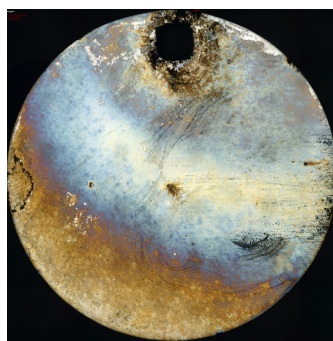


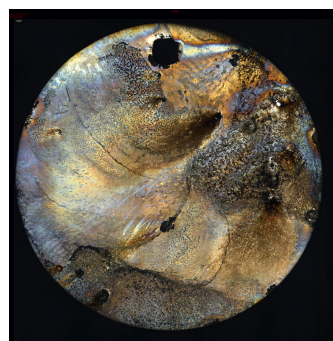
Figure C.2.2: Surface characterization by OM with a magnification of 2.5X of selected samples after electrochemical measurements according to ASTM G61 with an electrolyte temperature of 60°C.



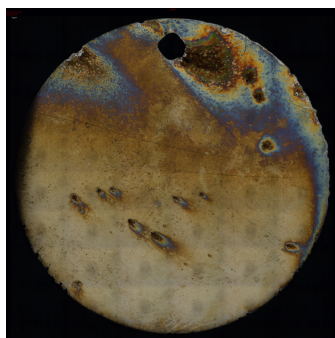
(a) Sample AD-80-1 after recording with an electrolyte temperature of 60°C.



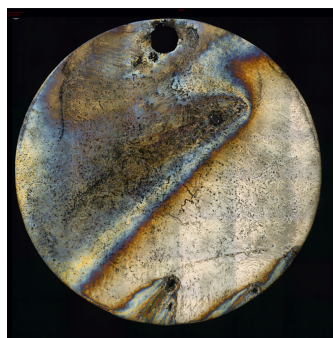
(b) Sample SA-80-1 after recording with an electrolyte temperature of 80°C.



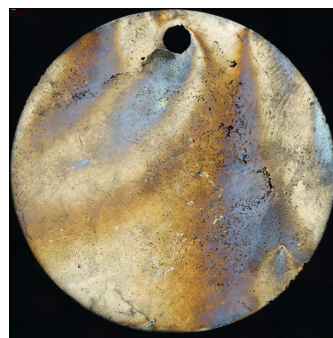
(c) Sample T2t3-80-2 after recording with an electrolyte temperature of 80°C.



(d) Sample W-T1t1-80-2 after recording with an electrolyte temperature of 80°C.



(e) Sample W-T1t4-80-2 after recording with an electrolyte temperature of 80°C.



(f) Sample W-T1t5-80-2 after recording with an electrolyte temperature of 80°C.

Figure C.2.3: Surface characterization by OM with a magnification of 2.5X of selected samples after electrochemical measurements according to ASTM G61 with an electrolyte temperature of 80°C.

C.3 OCP

OCP was measured for one hour prior to anodic CPP. The results of the OCP measurements are given in Figure C.3.1, C.3.2, C.3.3, C.3.4, C.3.5 and C.3.6.

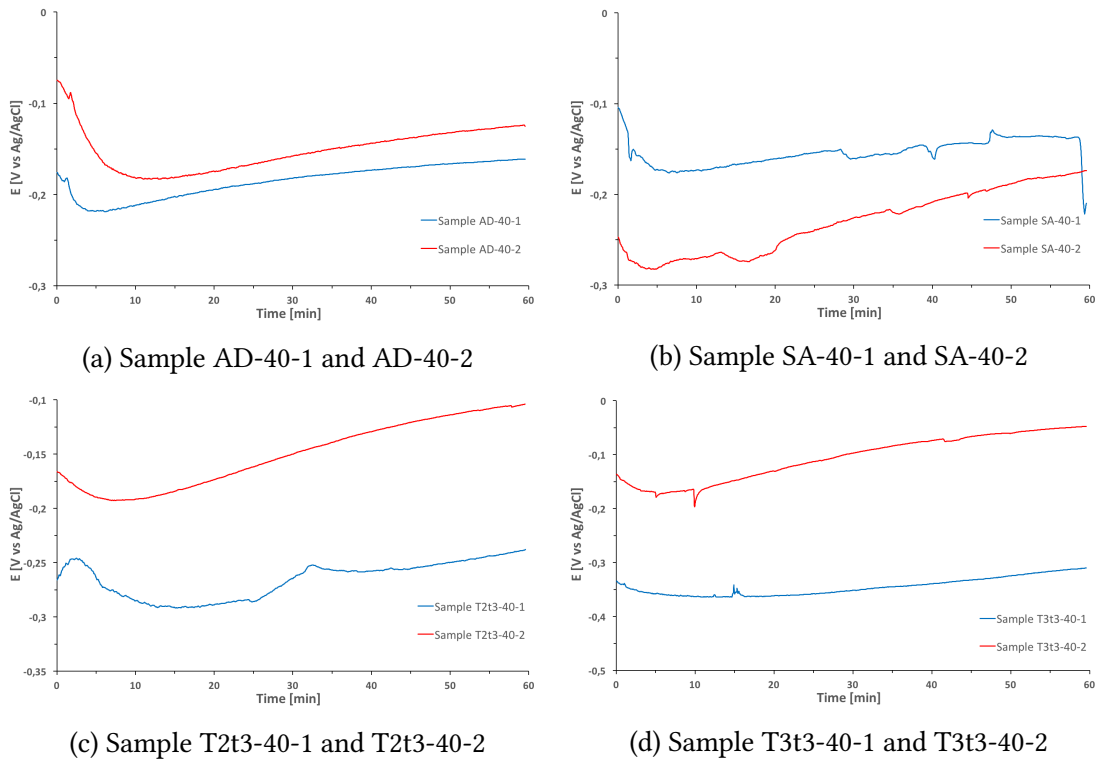
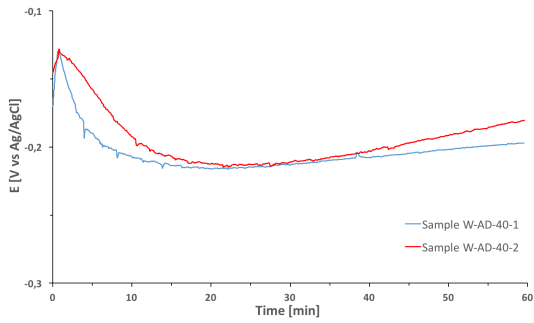
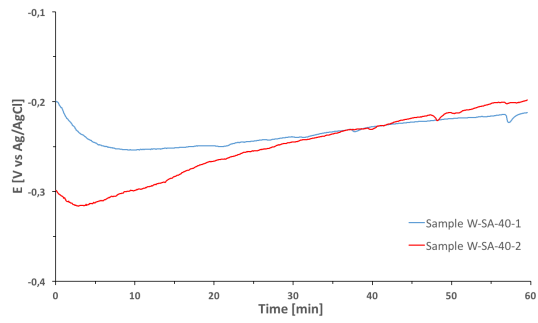


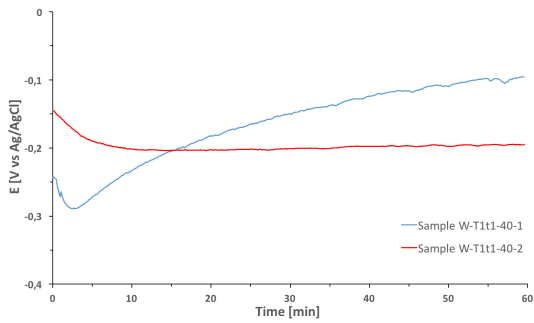
Figure C.3.1: The OCP measurements of UNS S32750 samples obtained at 40°C, according to Table 3.3.4.



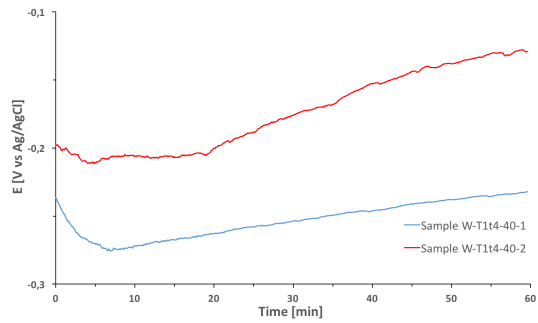
(a) Sample W-AD-40-1 and W-AD-40-2



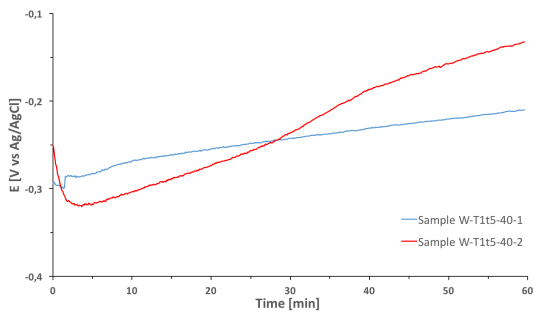
(b) Sample W-SA-40-1 and W-SA-40-2



(c) Sample W-T1t1-40-1 and T1t1-40-2



(d) Sample W-T1t4-40-1 and T1t4-40-2



(e) Sample W-T1t5-40-1 and T1t5-40-2

Figure C.3.2: The OCP measurements of UNS S39274 samples obtained at 40°C, according to Table 3.3.4.

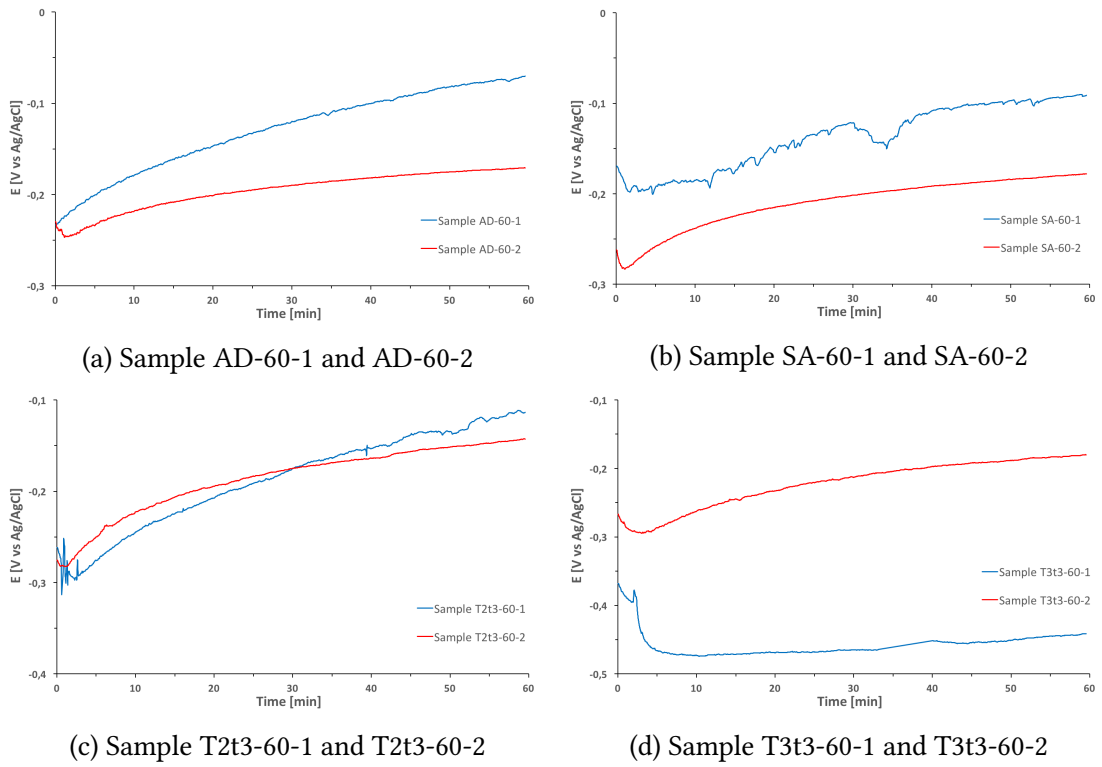
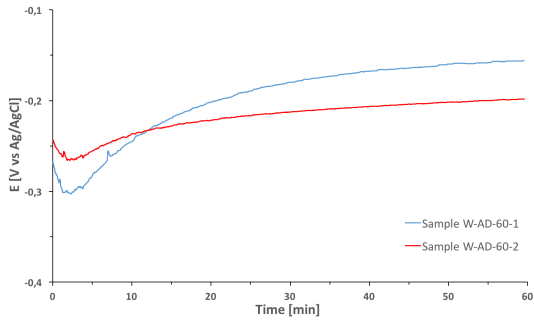
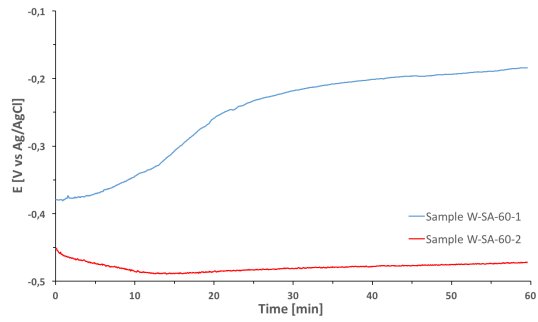


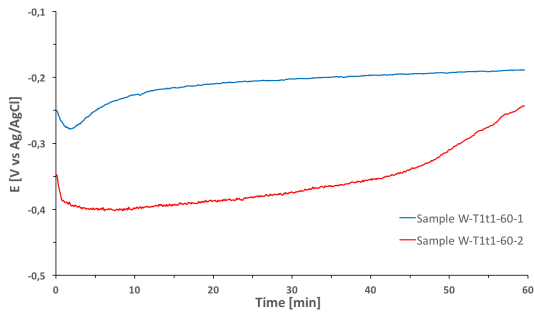
Figure C.3.3: The OCP measurements of UNS S32750 samples obtained at 60°C, according to Table 3.3.4.



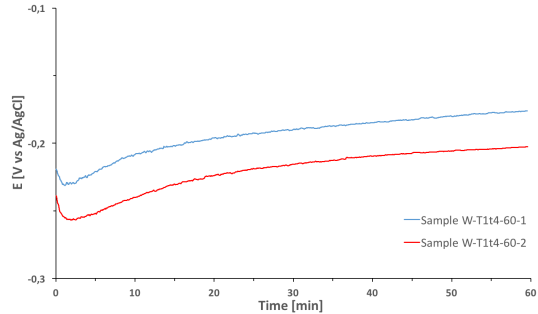
(a) Sample W-AD-60-1 and W-AD-60-2



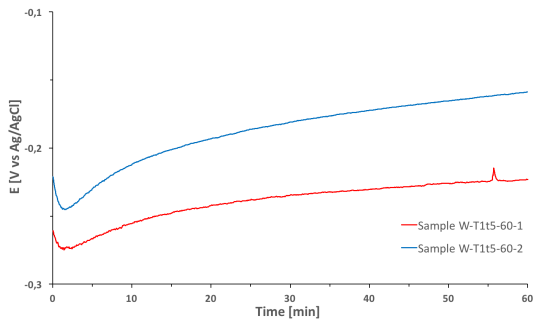
(b) Sample W-SA-60-1 and W-SA-60-2



(c) Sample W-T1t1-60-1 and W-T1t1-60-2

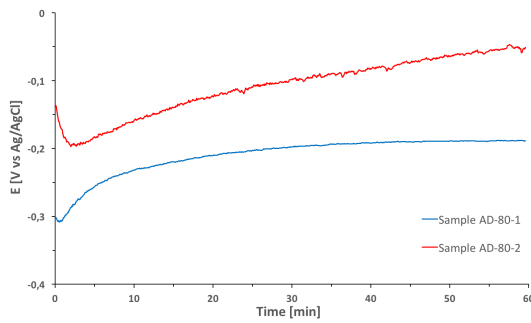


(d) Sample W-T1t4-60-1 and W-T1t4-60-2

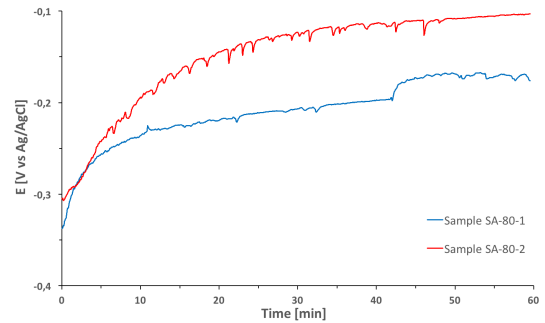


(e) Sample W-T1t5-60-1 and W-T1t5-60-2

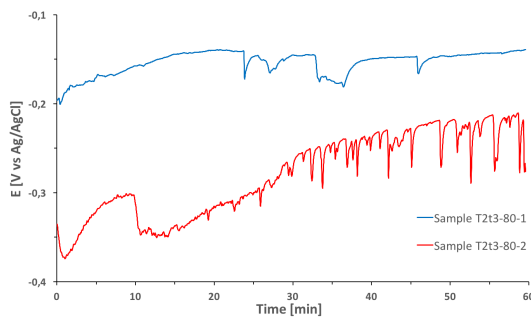
Figure C.3.4: The OCP measurements of UNS S39274 samples obtained at 60°C, according to Table 3.3.4.



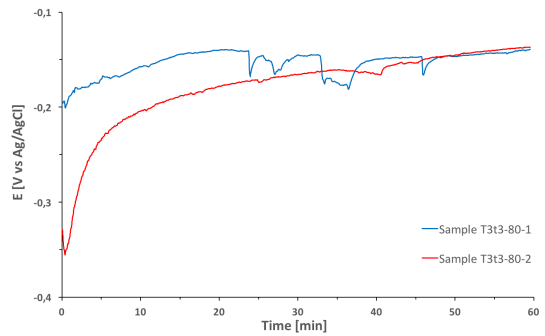
(a) Sample AD-80-1 and AD-80-2



(b) Sample SA-80-1 and SA-80-2

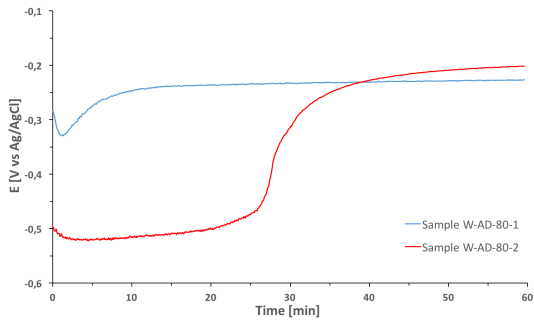


(c) Sample T2t3-80-1 and T2t3-80-2

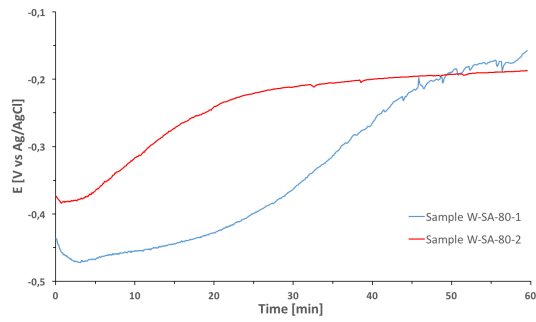


(d) Sample T3t3-80-1 and T3t3-80-2

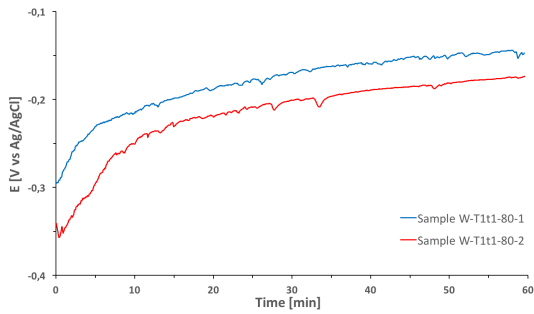
Figure C.3.5: The OCP measurements of UNS S32750 samples obtained at 80°C, according to Table 3.3.4.



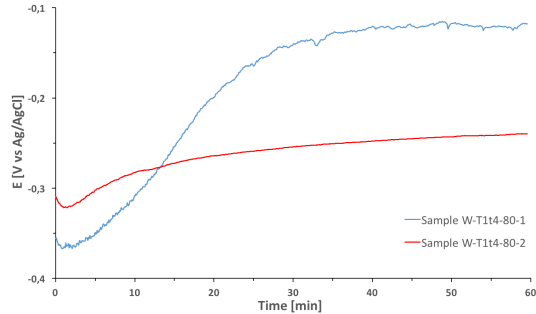
(a) Sample W-AD-80-1 and W-AD-80-2



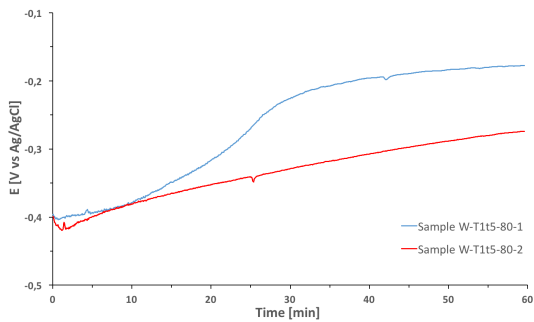
(b) Sample SA-80-1 and SA-80-2



(c) Sample W-T1t1-80-1 and W-T1t1-80-2



(d) Sample W-T1t4-80-1 and W-T1t4-80-2



(e) Sample W-T1t5-80-1 and W-T1t5-80-2

Figure C.3.6: The OCP measurements of UNS S39274 samples obtained at 80°C, according to Table 3.3.4.